Measuring the solar atmosphere

Jaime de la Cruz Rodríguez

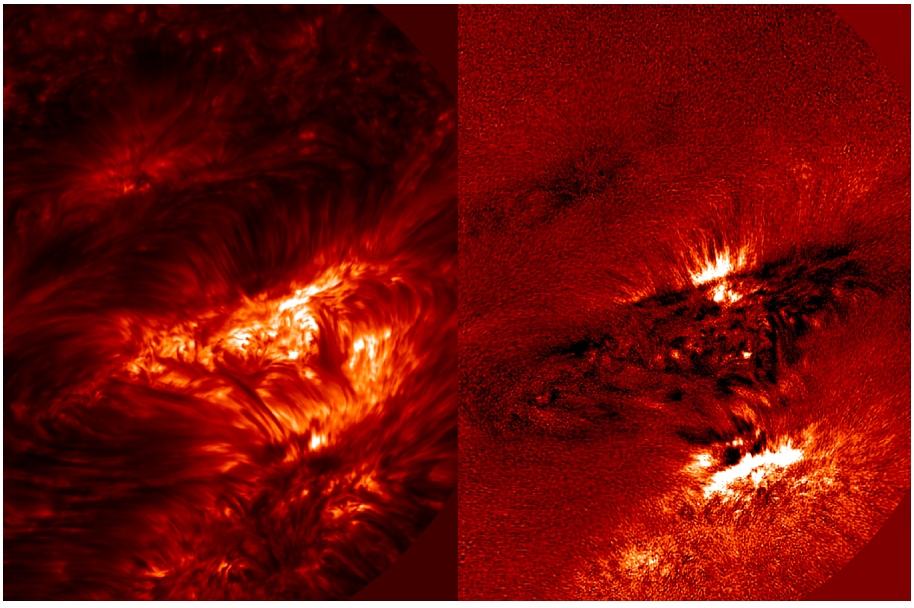

Department of Astronomy
Stockholm University

Cover image:
The chromosphere seen at Ca II 854.2 nm close to the solar limb. The image on the left shows the complex fibrilar topology of the chromosphere around two sunspots. The image on the right shows circular polarization which is produced by the line of sight component of the magnetic field.
Image credit: Observations by Luc Rouppe van der Voort (ITA-UiO) at Swedish 1-m Solar Telescope. Dataset restored by Jaime de la Cruz Rodríguez.

ISBN 978-91-7447-154-0
Universitetsservice, US-AB, Stockholm 2010
Department of Astronomy, Stockholm University

Doctoral Dissertation 2010
Department of Astronomy
Stockholm University
SE-106 91 Stockholm

Abstract

The new CRISP filter at the Swedish 1-m Solar Telescope provides opportunities for observing the solar atmosphere with unprecedented spatial resolution and cadence. In order to benefit from the high quality of observational data from this instrument, we have developed methods for calibrating and restoring polarized Stokes images, obtained at optical and near infrared wavelengths, taking into account field-of-view variations of the filter properties.

In order to facilitate velocity measurements, a time series from a 3D hydrodynamical granulation simulation is used to compute quiet Sun spectral line profiles at different heliocentric angles. The synthetic line profiles, with their convective blueshifts, can be used as absolute references for line-of-sight velocities.

Observations of the Ca II 8542 Å line are used to study magnetic fields in chromospheric fibrils. The line wings show the granulation pattern at mid-photospheric heights whereas the overlying chromosphere is seen in the core of the line. Using full Stokes data, we have attempted to observationally verify the alignment of chromospheric fibrils with the magnetic field. Our results suggest that in most cases fibrils are aligned along the magnetic field direction, but we also find examples where this is not the case.

Detailed interpretation of Stokes data from spectral lines formed in the chromospheric data can be made using non-LTE inversion codes. For the first time, we use a realistic 3D MHD chromospheric simulation of the quiet Sun to assess how well NLTE inversions recover physical quantities from spectropolarimetric observations of Ca II 8542 Å. We demonstrate that inversions provide realistic estimates of depth-averaged quantities in the chromosphere, although high spectral resolution and high sensitivity are needed to measure quiet Sun chromospheric magnetic fields.

A Klara

List of Papers

This thesis is based on the following publications:

I **Solar velocity references from 3D HD photospheric models**
de la Cruz Rodríguez J., Kiselman D., Carlsson M., 2010, submitted to A&A

II **Non-LTE inversions from a 3D MHD chromospheric model**
de la Cruz Rodríguez J., Socas-Navarro H., Carlsson M., Leenaarts J., 2010, to be submitted to A&A

III **Are solar chromospheric fibrils tracing the magnetic field?**
de la Cruz Rodríguez J., Socas-Navarro H., 2010, submitted to A&A

IV **Stokes imaging polarimetry using image restoration at the Swedish 1-m Solar Telescope II: A calibration strategy for Fabry-Pérot based instruments**
Schnerr R., de la Cruz Rodríguez J., van Noort M. 2010, submitted to A&A

The articles are referred to in the text by their Roman numerals.

Contents

1 Introduction

The solar atmosphere constitutes a remarkably complex astrophysical laboratory that continuously performs experiments for us to observe. One reason for trying to understand this complicated environment is to establish with high precision simple but fundamental properties of the Sun. An important example is its chemical composition which can be put in context with our understanding of the astrophysical processes in the interior of the Sun and other stars, in the Galaxy, and in the early universe. To accomplish this, we need to take into account the dynamics of the solar photosphere as well as the physical processes involved in the formation of the spectral lines from which chemical abundance ratios are determined. This represents a major challenge and our confidence in the results rely heavily on the accuracy of measurements made with modern solar telescopes.

A second reason for studying the solar atmosphere, and one that is even more relevant in the present thesis, is to understand the mechanisms that generate the observed fine structure, dynamics, and magnetic field and to carry over that understanding to other astrophysical plasmas, including other stellar atmospheres. Dramatic progress in this field has in recent years been made in part by improved theoretical simulations and in part by new solar telescopes, equipped with powerful instrumentation, on the ground and in space. Both simulations and observations clearly demonstrate that much dynamics occur at very small spatial scales. Obtaining accurate quantitative information that will allow us to confirm or refute new models requires pushing existing telescopes to their diffraction limit and designing future telescopes with improved spatial resolution, better signal-to-noise and equipped with multiple instruments to simultaneously diagnose different layers of the solar atmosphere. In addition, sophisticated post-processing methods are needed to enhance the fidelity of the observed data, by developing accurate methods for calibrations and for removing contamination from straylight due to limitations set by the Earth's atmosphere and optical imperfections in the telescope or its instrumentation. This thesis deals with the challenges of accurate measurements of quantities relevant to small-scale dynamics, based on observations with a major solar telescope: the Swedish 1-m Solar Telescope (SST) on La Palma.

Our observational data are from two distinct, but physically connected, layers of the solar atmosphere: the photosphere and the chromosphere. The dynamics and morphology of these two atmospheric layers are completely different. To a large extent, these differences can be attributed to magnetic fields:

whereas the gas pressure falls of exponentially with height and is roughly 10^5 times smaller in the chromosphere than in the photosphere, the magnetic field strength falls off much slower. The relative importance of forces associated with gas pressure and magnetic field can be estimated from the ratio of gas pressure (P_g) to magnetic pressure (P_B), the plasma-beta parameter defined by:

$$\beta = \frac{P_g}{P_B}$$

In the photosphere, β is much larger than unity everywhere, except in sunspots and other (mostly small-scale) concentrations of magnetic field. The photosphere is dominated by a convective energy flux, peaking just below the visible surface. Key questions today are to understand how this energy flux is maintained within magnetic structures and a major challenge is to identify and measure the velocity signatures of any convective flows present. These signatures are both weak and and small-scale and their identification relies on whether we can establish an absolute reference for measured Doppler velocities on the Sun. The first part of the present thesis deals with this problem.

The second part deals with observations of the chromosphere. Here, magnetic fields are much weaker than in the strongest magnetic structures seen in the photosphere but the gas pressure is even lower. In the upper chromosphere, $\beta < 1$ thus the magnetic forces are dominant. This work aims at investigating the potential for diagnosing the weak chromospheric magnetic fields using Stokes polarimetry and sophisticated inversion techniques.

To set the context, we proceed with an overview of some photospheric and chromospheric topics.

1.1 The Photosphere

The visible surface of the Sun corresponds to the photosphere, a thin layer of about 500 km located on top of the convection zone, where the plasma changes from completely opaque to transparent (Stix 2002).

1.1.1 Granulation

Outside active regions with strong magnetic fields, the photosphere is dominated by a dynamic pattern of bright *granules* surrounded by dark *intergranular lanes* (see Fig. 1.1). The flow in a granule resembles that of a fountain, where the hot plasma moves upwards inside the granules and then flows out towards the edge, where the cooler plasma merges with material from neighbouring granules. Gravity and pressure increase at the edge of the granules, accelerating the fluid downwards (Stein & Nordlund 1998). Regular granules

have a typical size of the order of 1 Mm, and a characteristic life time of 6 minutes (Bahng & Schwarzschild 1961).

Convective motions leave strong fingerprints on any line formed in the photosphere. An important diagnostic is the C-shaped bisector obtained from spatially-averaged line profiles. This effect is produced by the statistical average of bright blueshifted profiles from granules with dark redshifted profiles originating in the intergranular lanes (Dravins et al. 1981). This intensity weighted average is blueshifted as upflows are more heavily weighted by being brighter and covering a larger area than the narrower intergranular lanes. This shift is commonly known as the *convective blueshift*.

The thermodynamic history of fluid elements rising through the photosphere is described in detail by Cheung et al. (2007). The temperature decrease of a fluid element that moves up in the convection zone, is mostly produced by adiabatic expansion. As the fluid reaches the photosphere, the opacity drops and the fluid rapidly loses entropy by radiative cooling. At this point, the fluid cell is overshooting into the stably stratified photosphere, and it still interacts with the surroundings because it is not completely transparent to radiation. Fig. 1.2 shows the trajectory described by tracer fluid elements that enter the photosphere. The color coding indicates the sign of $Q_{\rm rad}$, the heat exchange with the surroundings, in dark for radiative loses ($Q_{\rm rad} < 0$) and in light grey where the fluid elements are being heated ($Q_{\rm rad} > 0$). Interestingly, there is no direct correlation between heat exchange and the temperature variation of the fluid elements, which is determined by a balance between adiabatic expansion and (non-adiabatic) heat exchange with the surroundings.

In recent years, efforts to obtain refined estimates of solar abundances have given rise to some controversies (see e.g. Asplund et al. 2000). This debate stimulated improvements of treatment of energy transfer by radiation in 3D hydrodynamic simulations, in particular for the mid and high photosphere, where spectral lines are formed. These controversies have also stimulated the development of improved non-LTE calculations of spectral lines used for abundance calculations (Shchukina & Trujillo Bueno 2001). As a result, 3D MHD simulations of more complex solar atmosphere dynamics involving magnetic fields can now also be made with improved energy transfer than just a few years ago.

1.1.2 Sunspots

The structure and dynamics of sunspots remain some of the most controversial topics in the solar photosphere. Sunspots constitute strong magnetic field concentrations that appear in the atmosphere and present typical sizes of 12000 km. As a first approximation, we can assume that the magnetic field acts on the gas in the form of a magnetic pressure,

$$P_B = \frac{B^2}{2\mu_0}.$$

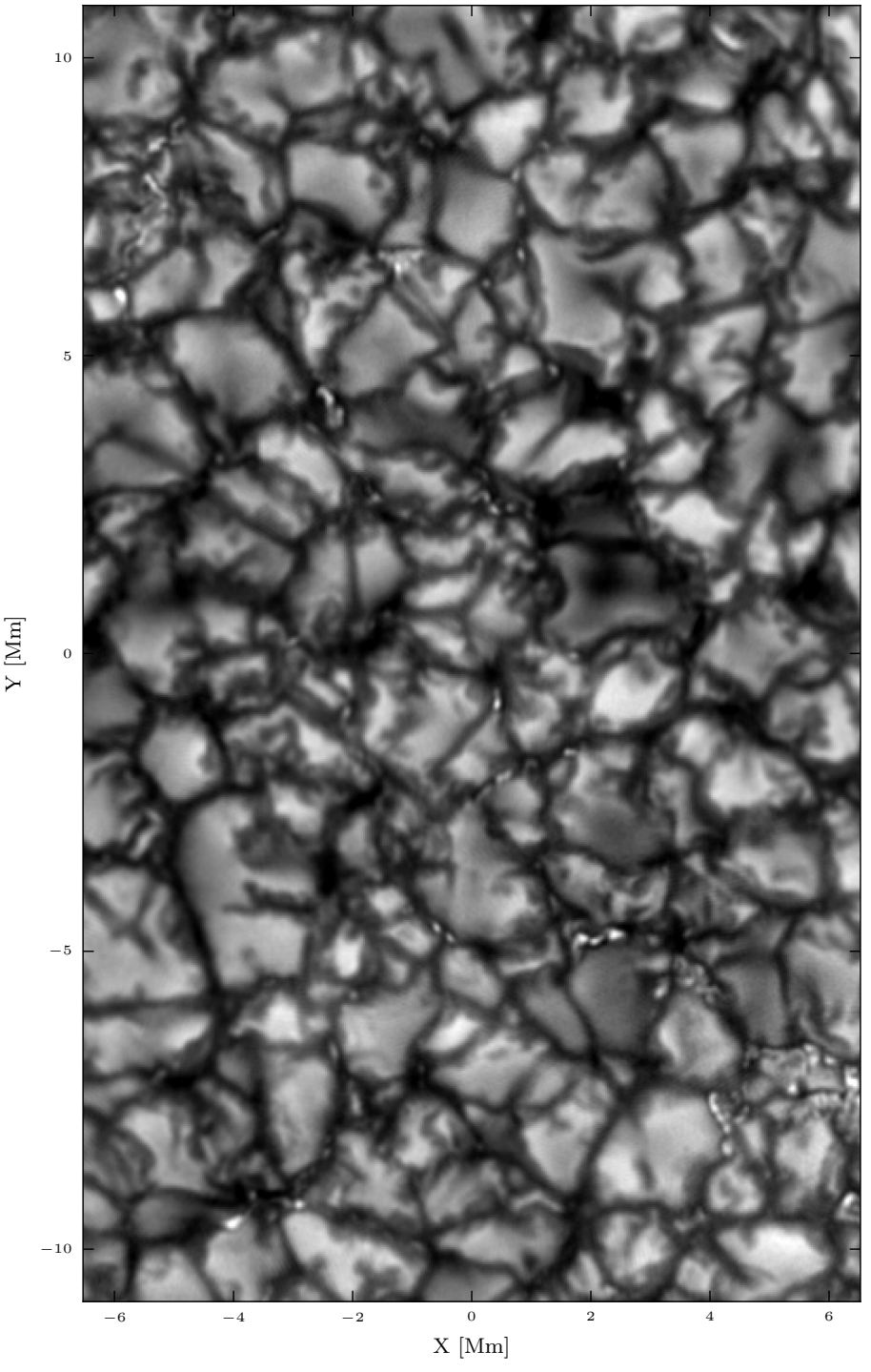

Figure 1.1: The photosphere imaged in the G-band at 430 nm with the Swedish 1-m Solar telescope. Image courtesy of M. van Noort & L. Rouppe van der Voort (ITA-UiO).

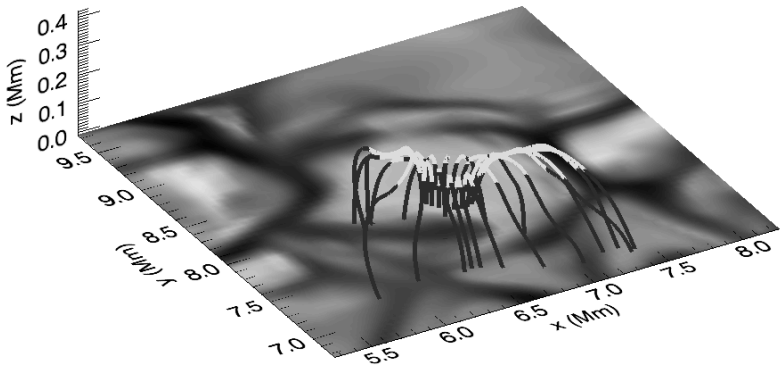

Figure 1.2: Trajectories of tracer fluid elements above a granule. The grayscale image show the vertical velocities at at $Z = 0$ when the tracers were released. The colors in the trajectories correspond to $Q_{\rm rad} < 0$ (dark-grey) and $Q_{\rm rad} > 0$ (light-grey). From Cheung et al. (2007) (reproduced with permission of the authors).

Horizontal force balance then dictates that the sum of the gas pressure and magnetic pressure must be the same inside the sunspot as outside. This implies that

$$P_s + \frac{B^2}{2\mu_0} = P_{qs}$$

where P_s is the gas pressure inside the spot and P_{qs} is the gas pressure in the surrounding (non-magnetic) quiet sun. An immediate consequence of this is that the gas pressure inside the spot must be lower than outside and that therefore the atmosphere is more transparent inside sunspots, allowing observers to see deeper layers of the atmosphere than in quiet Sun observations. This is generally known as the Wilson depression ($\sim$ 500 km), discovered by Wilson & Maskelyne (1774). At the same time the H^- opacity decreases with temperature, and sunspots are cooler than their environment so the opacity decreases even more. Sunspots are darker than their surrounding granulation because convection is suppressed by the strong magnetic field, thus sunspots are cooler as an effect of inefficient heat transfer.

During the past decade, the scientific debate has focused on the dynamics and structure of the penumbra and explaining why the penumbra is as bright as it is, about 75% of the surrounding quiet sun. Recent advances in instrumentation have unveiled very fine structure in sunspots, especially in the penumbra. Fig. 1.3 illustrates in great detail the fine structure of the penumbra of a sunspot. The blown-up section shows dark cored penumbral filaments (Scharmer et al. 2002) and the inner umbra. The following theoretical frameworks (Scharmer 2008) have become popular because they can partially reproduce the features observed in sunspots, in spite of representing different physical concepts.

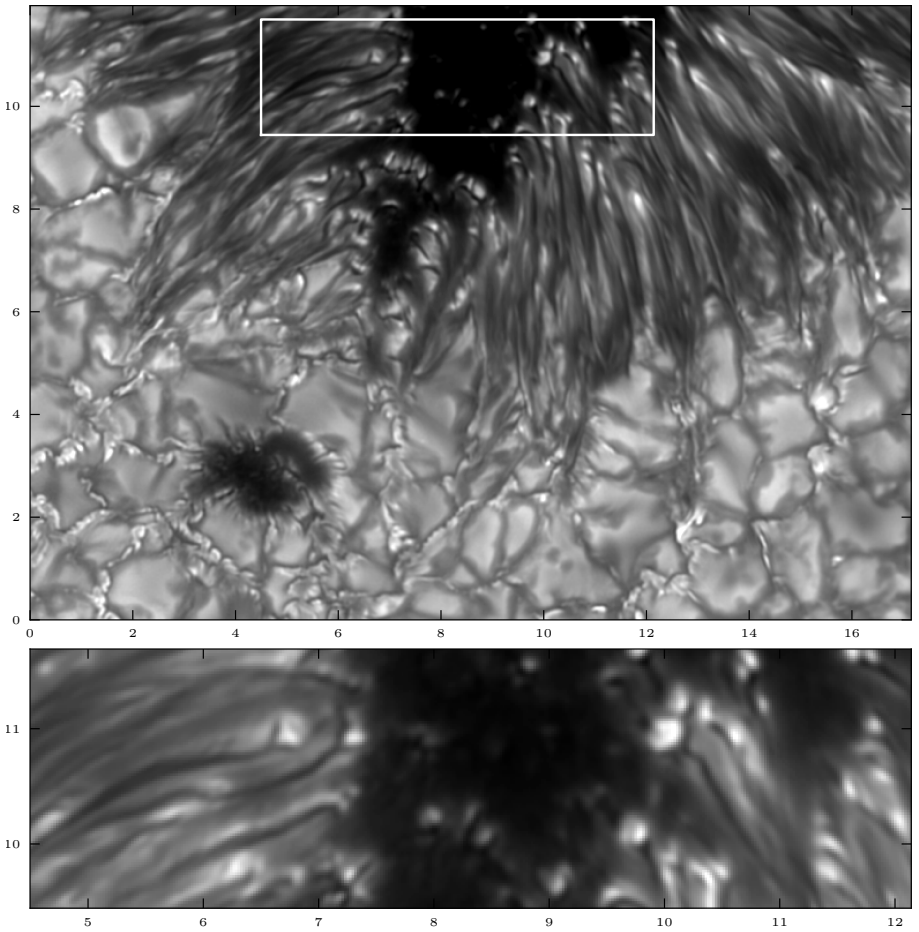

Figure 1.3: Surroundings of a sunspot (top) and close-up view of penumbral filaments (bottom). The units of the axis are given in Mm. Continuum observations at 396 nm, by Vasco Henriques (ISP-KVA).

1. **The uncombed penumbra model** (Solanki & Montavon 1993) postulates the existence of discrete flux tubes with homogeneous magnetic field inside that discontinuously changes at the boundary. Those nearly horizontal flux tubes are embedded in a more vertical magnetic field. This model was able to reproduce strongly asymmetric Stokes V profiles observed on the limb side of the penumbra in observations off disk center (Sanchez Almeida & Lites 1992).
2. **Siphon flow models** (Meyer & Schmidt 1968; Montesinos & Thomas 1997) are based on the idea that a difference in field strength between the two footpoints of a flux tube leads to a difference in gas pressure, driving a plasma flow in the direction of the footpoint with the highest field strength (thus lower gas pressure). Evershed flows are assumed to be steady flows between two footpoints with different magnetic field strengths (e.g.,

Westendorp Plaza et al. 1997). However, these models do not explain the mechanism involved in such field strength difference at the footpoints.

3. **Convection and downward pumping of magnetic flux** are ingredients added to the siphon models. As siphon models present a stationary solution, time variations are explained by external mechanisms to the penumbra. In this context, moving penumbral grains are assumed to be produced by a moving convective pattern in the bright side of the penumbra. Thomas et al. (2002) and Weiss et al. (2004) attribute the submergence of the flux tubes at the boundary of the penumbra to downward pumping produced by convective motions. Furthermore, they attribute the whole filamentary structure of the penumbra to the same downward pumping mechanism, explaining the structure inside the sunspot based on mechanisms that take place outside.
4. **The convective gap model** proposed by Scharmer & Spruit (2006). In this framework, the proposed mechanism that generates penumbral filaments is convection, in radially aligned, nearly field free gaps. The strong field gradients that are necessary to reproduce the asymmetric Stokes V profiles reported by Sanchez Almeida & Lites (1992) are assumed to be produced by the topology of nearly field-free gaps combined with line-of-sight gradients in the flow velocity. The Evershed flow is explained as representing the horizontal component of this convection.

1.1.3 Oscillations in the solar atmosphere

Solar oscillations were discovered by Leighton et al. (1962) with a simple observational technique: two simultaneous images were recorded in the blue and the red wings of a spectral line, respectively, and then subtracted. The resulting image contained intensity variations produced by the Doppler shift of the line. Kahn (1961) proposed that oscillations are sound waves trapped in the solar atmosphere. Towards the solar interior, the temperature and speed of sound increase with the variation of the refractive index, caused by the increased density. The wave is refracted until it starts to propagate upwards. The same process occurs above the photosphere where the waves are refracted back into the inner atmosphere. Observations contain an overlap of hundreds of modes of oscillation that effectively reach different depths. The oscillations in the photosphere typically have a 5-minute period and an amplitude around 1 km s^{-1} (Stix 2002).

1.2 The chromosphere

The chromosphere represents many challenges for solar physicists. Despite important discoveries during the past decade, it still remains unexplored to a large extent. From an observational point of view, only a few spectral lines

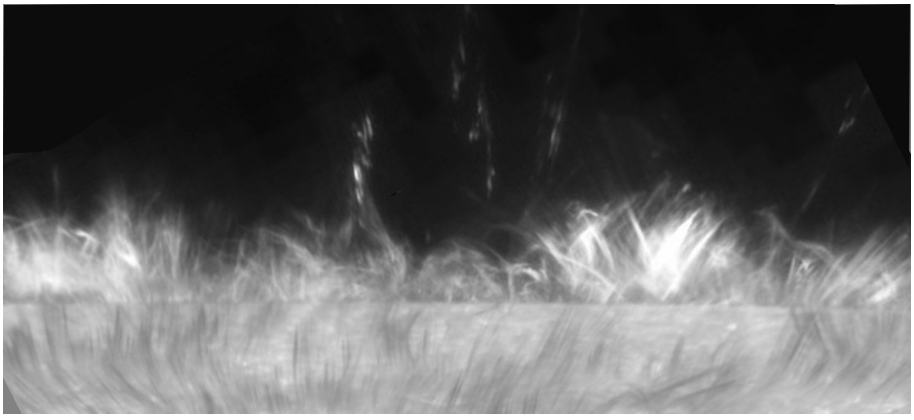

Figure 1.4: Spicules at the limb seen at H I 6563 Å. Intensity gradients towards the limb have been filtered to enhance the off-limb part. Image taken at the Swedish 1-m Solar Telescope, courtesy of Luc Rouppe van der Voort (ITA-UiO).

are sensitive to the chromospheric height range and those are usually hard to model and understand, like H I 6563 Å, Ca II K & H (3934 and 3968 Å respectively), the Ca II infrared triplet (8498, 8542 & 8662 Å), Na I D_1 (5896 Å) , He I 10830 Å.

During the past 15 years combined efforts from observational and computational approaches have lead to a better understanding of chromospheric dynamics. 3D simulations of solar-like stars including a chromosphere and corona are now computationally affordable (Leenaarts et al. 2007; Hansteen et al. 2007; Carlsson et al. 2010).

On the observational side, a new generation of Fabry-Perot interferometers (FPI), for example IBIS at the Dunn Solar Telescope (DST) and CRISP at the Swedish 1-m Solar Telescope (SST), have provided evidences of very fine structure in the chromosphere.

1.2.1 The chromospheric landscape

The definition of chromospheric fine structure has evolved as new discoveries were made. It is widely accepted that the chromosphere includes the characteristic grass-like topology usually seen in H_α images (Rutten 2006), but it is not clear where the boundaries of the chromosphere are. Fig. 1.5 shows three Ca II 8542 Å images acquired with SST/CRISP. This strong spectral line shows photospheric granulation at the wings and chromospheric fibrilar features in the core. Some chromospheric features are:

- **Straws** are bright features seen in the core of chromospheric lines (Rutten 2007). They start in facular regions in the photosphere and are much brighter than their surroundings in the chromosphere, showing hedge shapes in filtergrams. Fig. 1.5 shows a close view of straws, . In the upper panel, photospheric faculae become brighter than the surroundings at

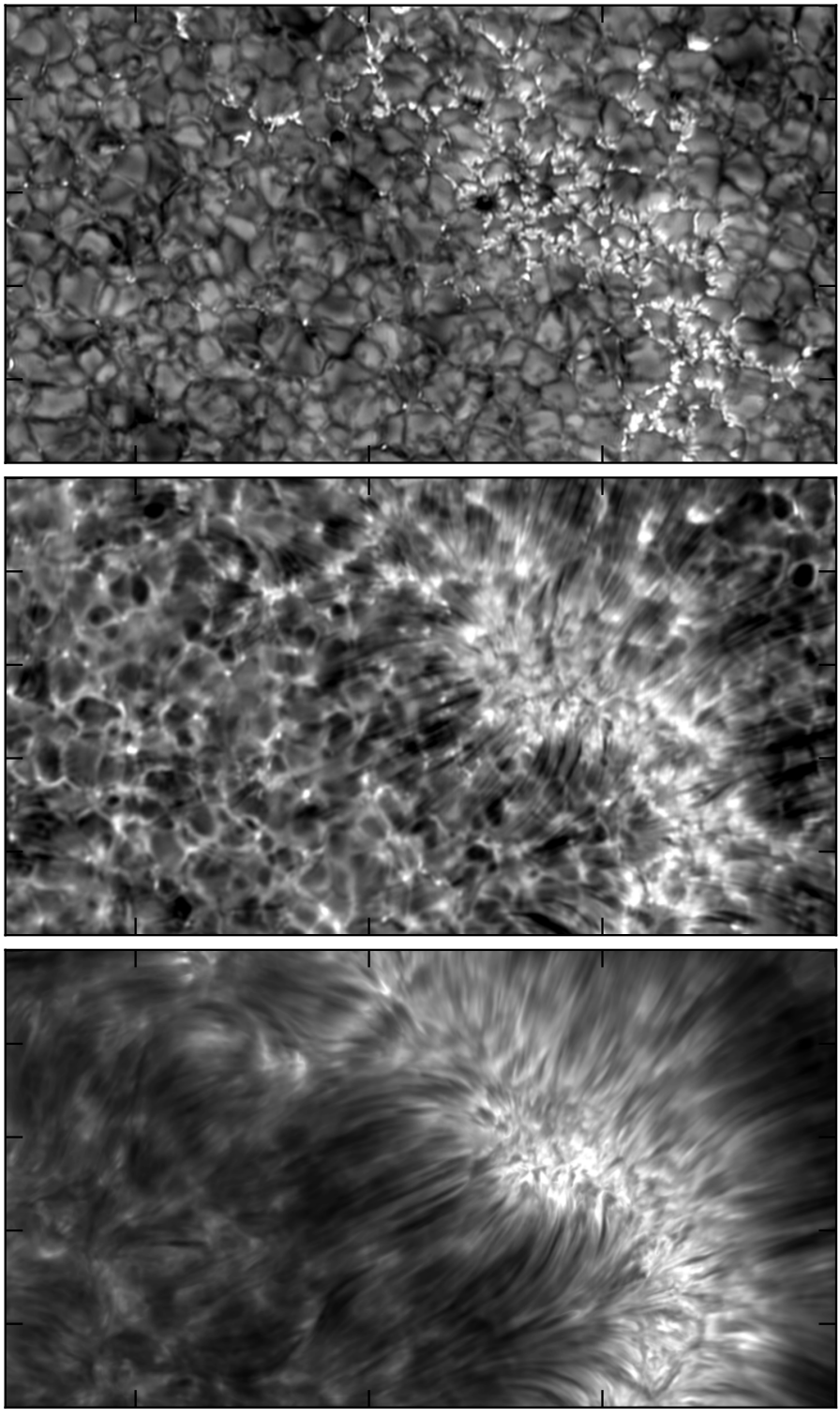

Figure 1.5: Images in Ca II 8542 Å taken at the SST. *Top:* the mid-photosphere. *Middle:* High-photosphere/low-chromosphere. *Bottom:* the chromosphere.

mid-photospheric heights. Fibrils seem to originate in these straws, as shown in the lower panel in Fig. 1.5.

- **Fibrils,** also known as mottles, are elongated dark features that in H I 6563 Å (hereafter H_α) form a grass-like canopy covering internetwork cells at any heliocentric angle. They are also present Ca II images, but they only appear around network patches, as shown in Fig. 1.5. They are very dynamic and show transversal motions over a time period of 2 seconds. Hansteen et al. (2006) and Rouppe van der Voort et al. (2007) proposed that dynamic fibrils are driven by magneto-acoustic shocks that leak into the chromosphere along magnetic field lines.
- **Spicules:** limb images of the chromosphere are dominated by spicules. De Pontieu et al. (2007) provided a detailed description of spicules and proposed physical mechanisms that could drive them. Spicules appear as thin, long highly dynamic features, usually reaching heights around 5000 km (see Fig. 1.4). Their width varies from 700 km down to current telescopes diffraction limit ($\sim$ 100 km). Spicules are classified in type I and type II. Type I spicules move up and down in time scales of 3-7 minutes and some of them present transversal motions. However, those fibrils that do not move transversely show acceleration and trajectories that are similar to those of dynamic fibrils, suggesting that they are also driven by magneto-acoustic shocks. Type II spicules are very dynamic and show apparent speeds between 50-150 km s^{-1}, disappearing in time scales of 5-20 s. The mechanism driving type II spicules is not well understood, although their rapid disappearance suggests that strong heating could be ionizing Ca II atoms. Recently, Rouppe van der Voort et al. (2009) found on-disk counterparts of spicules, which produce a clear signature in the blue wing of the H I 6563 and Ca II 8542 lines.
- **Filaments** are (dark) cold clouds of material that according to their temperature, belong to the chromosphere. They present typical lengths of 200000 km, with thickness's of 5000 km (Stix 2002). Towards the limb, filaments are known as **prominences** that appear *hanging* above the chromosphere up to 50 000 km. The only known mechanism that can sustain such cold and dense material is an electromagnetic force. Photospheric observations show that filaments predominantly exist along neutral magnetic field lines. Present observational efforts aim at measuring magnetic field in the filaments.

1.2.2 Chromospheric heating

One outstanding question about the chromosphere relates to its energy budget. Why is the outer atmosphere of the sun hotter than the photospheric surface? Semi-empirical, one-dimensional models of quiet Sun require the average temperature to rise above the photosphere to reproduce the chromospheric intrinsic enhanced emission (VAL3, Vernazza et al. 1981). However, observa-

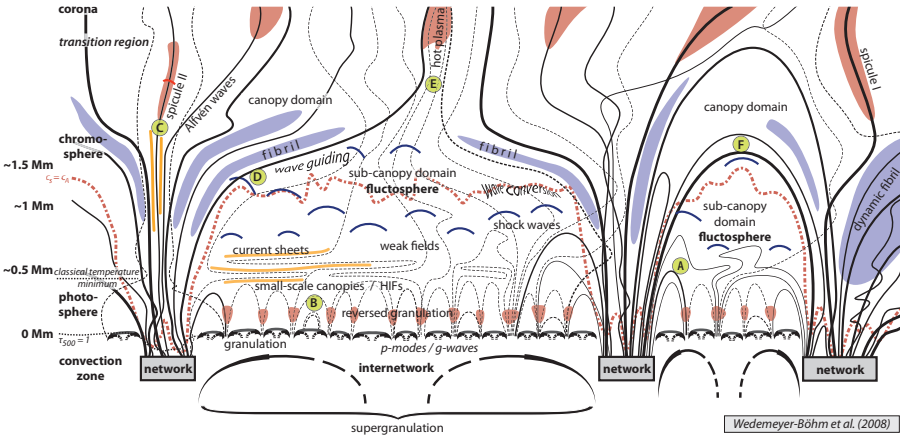

Figure 1.6: Schematic structure of the quiet sun atmosphere (Wedemeyer-Böhm et al. 2009), including some network patches. The black solid lines represent magnetic field lines that are anchored in the photosphere through network regions.

tions show that the chromosphere is vigorously active and strongly inhomogeneous. Carlsson & Stein (1995) demonstrated that enhanced emission can be produced by shocks without increasing the mean gas temperature. At present, the connection of waves with chromospheric heating appears widely accepted (Fossum & Carlsson 2005; Cauzzi et al. 2007; Wedemeyer-Böhm et al. 2007; Vecchio et al. 2009), however the exact role of these waves is still under debate.

1.2.3 Magnetic field configuration

The relatively organized and elongated fibrils seen in chromospheric lines (see Fig. 1.5) suggests the presence of magnetic fields. However, if magnetic fields dominate the chromosphere with $\beta \ll 1$, those should be almost force free, leading to relatively smooth magnetic configuration. Thus, the complex fine structure must relate to the thermodynamics of the plasma (Judge 2006).

The features described in §1.2.1 and their connection with the photosphere have been contextualized by Wedemeyer-Böhm et al. (2009) in the cartoon shown in Fig. 1.6. Magnetic field lines form a canopy where $\beta \sim 1$. Below the magnetic canopy, acoustic waves originating in the photosphere are dissipated, producing short-lived bright features seen in the wings of Ca II images. In this cartoon, fibrils and spicules form the magnetic canopy, which originates from network patches in the photosphere and extends over internetwork regions in the chromosphere.

We investigate the relation between fibrils and magnetic fields in **Paper III**, looking for an observational evidence of their alignment.

2 Velocity references on solar observations

This chapter describes the inherent difficulties in measuring absolute line-of-sight (LOS) velocities from spectroscopic observations. To illustrate the importance of this problem, we recall the discussion in Chapter 1 where we summarized the main theoretical frameworks that have been proposed to explain the structure and dynamics of sunspots. A key difference between flux-tube models and the field-free gap model is that the latter explains penumbral filaments as convective intrusions where magnetic field is weak enough not to suppress convection. Thus, observational evidence of convective motions inside penumbral filaments would be a key to explaining the origin of its filamentary structure and choosing among existing models. These types of measurements are very hard to make because in the upper part of the filament overshooting convection is expected to be weak. At the same time, the presence of the Evershed flow and the small scales involved, makes it very hard to establish the existence of overturning convection inside penumbral filaments. For these reasons, a very accurate velocity calibration is needed to make it possible to distinguish between the upflowing and downflowing components of any convection.

2.1 The calibration problem

The fundamental question that is addressed here is: *What defines the local frame of rest on the Sun?* An observer placed on the Sun would apply Eq. 2.1 to measure LOS velocities, would apply the relationship

$$v = \frac{\lambda - \lambda_0}{\lambda_0} \cdot c, \tag{2.1}$$

where λ is the observed wavelength, λ_0 is the reference wavelength (usually the laboratory wavelength of the line of interest) and c is the speed of light. However, ground-based observations are affected by the rotation of the Earth ($v_{\oplus,\mathrm{rot}}$), the radial component of the Earth's orbital motion ($v_{\oplus,\mathrm{orbit}}$), the rotation of the Sun ($v_{\odot,\mathrm{rot}}$) and the graviational redshift (v_{grav}), the relarion is in reality more complex,

$$v = \frac{\lambda - \lambda_0}{\lambda_0} \cdot c + v_{\oplus,\mathrm{rot}} + v_{\oplus,\mathrm{orbit}} + v_{\odot,\mathrm{rot}} + v_{\mathrm{grav}}, \tag{2.2}$$

Furthermore the precision of the atomic data limits the accuracy of the conversion from wavelength to velocities, regardless of how accurate the instrument is. This calibration issue becomes more severe when observational practicalities make it difficult to compensate for the last three terms of Eq. 2.2. The gravitational redshift has a theoretical constant value of 633 m s^{-1} at the surface of the Earth (Cacciani et al. 2006).

In addition, current instruments for solar observations seldom use laboratory light sources as reference wavelengths. The obvious solution of finding a λ_0 on the Sun itself is confounded by the convective lineshifts discussed in Sect. 1.1.1. The magnitude of these shifts is different for different lines.

Below, we summarize some of the methods that have been used to define a velocity reference for spectroscopic observations.

1. Convective motions in **sunspot umbrae** are suppressed by the presence of strong magnetic fields. Thus, it is common to assume that the umbra is at rest, defining a reference for line-of-sight velocities (e.g., Beckers 1977; Scharmer et al. 2008; Ortiz et al. 2010). However, this assumption usually does not hold higher up in the chromosphere, where umbral flashes associated with shocks (Socas-Navarro et al. 2000a) produce strong blue-shifts. This approach carries the risk of being affected by spurious line shifts produced by molecular blends that only form in the umbra because it is colder than the surrounding granulation. Eq. 2.1 can be used to compute the conversion from the wavelength scale to a velocity scale, but in this case λ_0 is the central wavelength of the spectral line measured in the umbra of a sunspot.
2. **Telluric lines** are sometimes present in the spectral range that is being observed. These lines are formed in the Earth's atmosphere. Thus, they allow the definition of a very accurate laboratory frame of rest that can be converted to the solar frame using ephemeris constants, the time of the observations and solar rotation (Eq. 2.2). The conversion from wavelength to velocities is calculated using the laboratory wavelength of the line of interest. Martinez Pillet et al. (1997) and Bellot Rubio et al. (2008) used this approach to calibrate their observations.
3. **A spectral atlas** can be used to calibrate observations, as the effects of the rotation and translation of the Earth usually have been compensated for. Langangen et al. (2007) used the atlas acquired with the Fourier Transform Spectrometer at the McMath-Pierce Telescope (hereafter FTS atlas) of Brault & Neckel (1987) to calibrate some of his observations. This atlas was acquired at solar center, thus its usability is limited to disk center observations.
4. **Numerical models** can be used to compute the convective shift of a line and use it as a reference for velocities. The advantage of this approach is that the convective shift is measured relative to the assumed laboratory wavelength of the line, so it is insensitive to uncertainties in the atomic

Table 2.1: *Spectral lines used to create calibration data in Paper I.*

C I	5380.34	forms in deep layers of the photosphere
Fe I	5250.21	magnetometry
Fe I	5250.63	magnetometry
Fe I	5576.09	Doppler measurements
Fe I	6082.71	abundance indicator
Fe I	6301.50	magnetometry
Fe I	6302.49	magnetometry
Fe I	7090.38	Doppler measurements
Ca II	8498.01	chromospheric diagnostics
Ca II	8542.05	chromospheric diagnostics
Ca II	8662.16	chromospheric diagnostics

data. Borrero & Bellot Rubio (2002) computed a two-components model from the inversion of photospheric Fe I lines. This model only contains the vertical component of the velocity field, thus it is limited to solar center. Tritschler et al. (2004) and Franz & Schlichenmaier (2009) used this model to calibrate disk center observations. However, Bellot Rubio et al. (2004), used it together with the empirical results of Balthasar (1988) to estimate lineshifts also off solar centre. Langangen et al. (2007) used a 3D hydrodynamical simulation of solar convection to calibrate observations on C I 5380 Å. The central wavelength of this line is not known with enough precision to allow the use of the FTS atlas method that was used with their observations.

2.2 Calibration data from hydrodynamic granulation models

In **Paper I**, we extend the calibration method employed by Langangen et al. (2007) for the C I 5380 line. Snapshots from a 3D hydrodynamical simulation are used to compute synthetic profiles assuming Local Thermodynamic Equilibrium (LTE) (see Fig. 2.1). The convective shift of the spatially-averaged profile is measured from spectra computed with the numerical simulation. Our calculations are performed for eleven selected lines of interest for solar observers (listed in Table 2.1), over a range of heliocentric angles (distance from solar disc centre). The synthetic line profiles are provided in digital form to the community. This method assumes that 3D models can reproduce the correlation between brightness and Doppler shift of granulation in a statistical sense (see Fig. 2.2). The elemental abundances is used as a free parameters

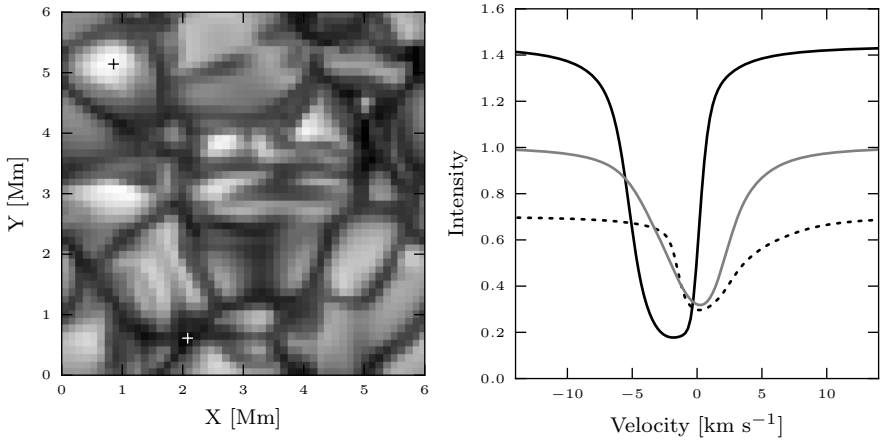

Figure 2.1: *Left:* Continuum intensity at 6301 Å image from one of the 3D snapshots from the numerical simulation. The latter has been resampled at lower spatial resolution. *Right:* Spectra from a blueshifted granule (solid black line) and redshifted intergranular lane (dashed line). The grey line corresponds to the spatial average of this snapshot. Two crosses on the left panel indicate the location of the spectra represented on the right panel.

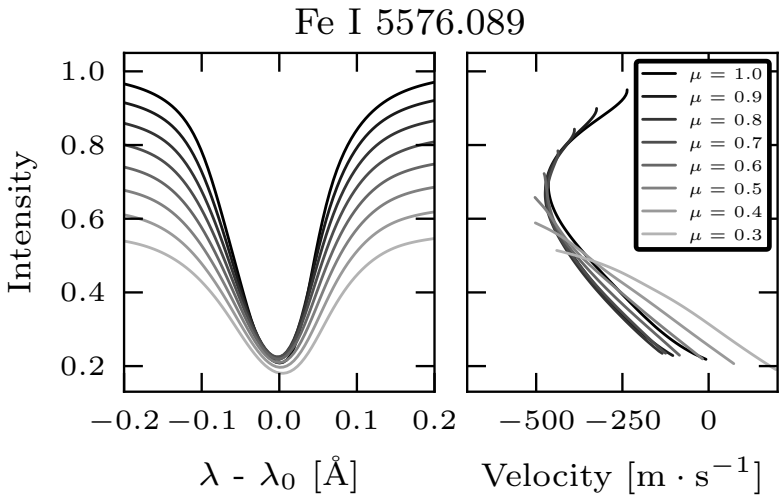

Figure 2.2: Synthetic profiles and the corresponding bisectors resulting from the calculations of Fe I 5576.09 Å. The grey scale indicates the variation of the heliocentric angle from $\mu = 1.0$ to $\mu = 0.3$.

to achieve the best possible agreement between the synthetic profiles and the FTS atlas. The estimated parameters should not be regarded as abundances, as they also compensate for uncertainties in the atomic data, the LTE approximation used in the radiative transfer calculations, and other errors. The accuracy of our results is inferred from experiments carried out using the 3D models. From this and from observational tests, we estimate the results to have an accuracy of $50\ \mathrm{m\ s^{-1}}$ at solar disk centre.

Our results have been analyzed using bisectors. The bisector of a spectral line indicates the center of the profile as a function of intensity. Fig. 2.2 illustrate our results for the Fe I 5576.09 Å line. The line bisectors are shown along with the profiles at different heliocentric angles.

In addition to providing calibration data, **Paper I** discusses the variations of the bisectors with disk position (μ). This *limb effect* is found to mainly be caused by the 3D structure of the granulation, while the changing intensity-velocity correlation with height plays a minor role.

3 Chromospheric diagnostics

It was mentioned in Chapter 1 that chromospheric observations are more difficult than those of the photosphere, especially when polarimetric measurements are involved. Spectral lines that are sensitive to the chromospheric range are usually very broad and only the core, where less photons are emitted, shows chromospheric features (Cauzzi et al. 2008), as illustrated in Fig. 3.1 where the granulation present in the wings smoothly changes into a chromospheric landscape close to the core of the line. The lack of light, in combination with a broad profile and weaker magnetic fields than in the photosphere conspire to reduce the amplitude of Stokes Q, U and V profiles.

The obvious solution to this problem would be to increase the exposure time of observations. However, the chromosphere is vigorously dynamic and long integration times usually translate into image smearing. The evolution time scale in the chromosphere can be estimated using an estimate of the Alfvén speed $v_A(B = 100\ \mathrm{G}, z = 1000\ \mathrm{km}) \sim 10^5\ \mathrm{m\ s^{-1}}$ in the chromosphere (see page 83, Priest 1982). In the case of the SST, the diffraction limit at 854.2 nm is 0."18 which corresponds to 130 km on the surface of the Sun. Thus, the chromosphere cannot be assumed to be static for times longer than 1.3 seconds (see van Noort & Rouppe van der Voort 2006).

Furthermore, this time scale also limits the spectral coverage of FPI observations, as only one wavelength can be observed at the time. It is normally assumed that the Sun does not change during a full scan of the line. If the the spectrum is sampled using a large number of frequency points, this assumption may not hold. Therefore, observing the chromosphere involves a trade-off between sensitivity, cadence and wavelength coverage.

3.1 Detectability of magnetic fields in the chromosphere

During the past decade, the lines of the Ca II infrared triplet have been extensively used to diagnose the chromosphere (see Langangen et al. 2008; Leenaarts et al. 2009; Cauzzi et al. 2009, and references therein), sometimes including polarization. Observational papers have usually studied cases with relatively strong magnetic field (Socas-Navarro et al. 2000a; Pietarila et al. 2007a; Judge et al. 2010; de la Cruz Rodríguez et al. 2010), whereas theoretical approaches have been restricted to 1D models (Pietarila et al. 2007b; Manso Sainz & Trujillo Bueno 2010).

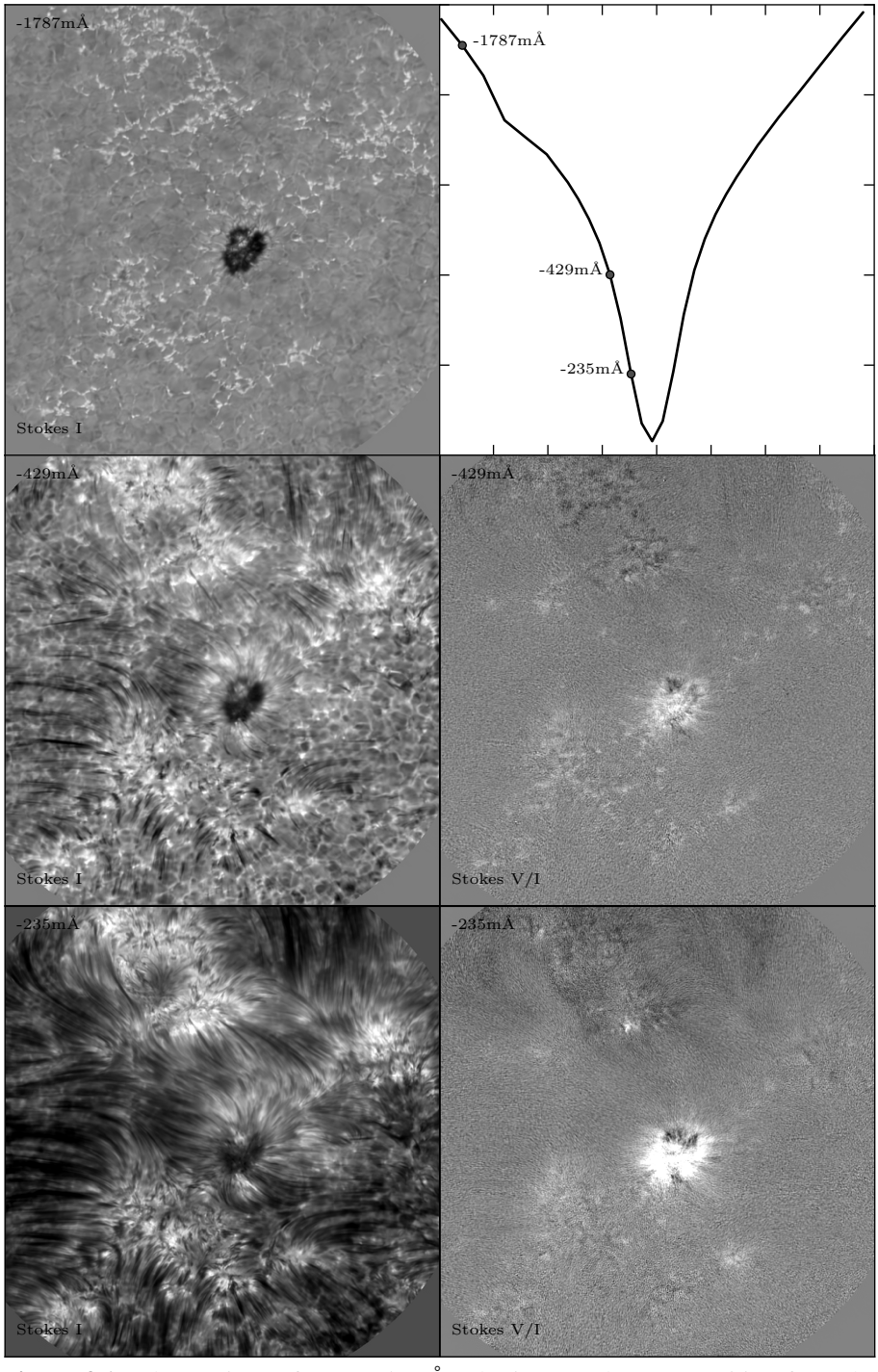

Figure 3.1: Observations of Ca II 8542 Å. The images show a transition from the photospheric wings of the line to the chromospheric core. The dataset was acquired by Luc Rouppe van der Voort (ITA-UiO) with SST/CRISP.

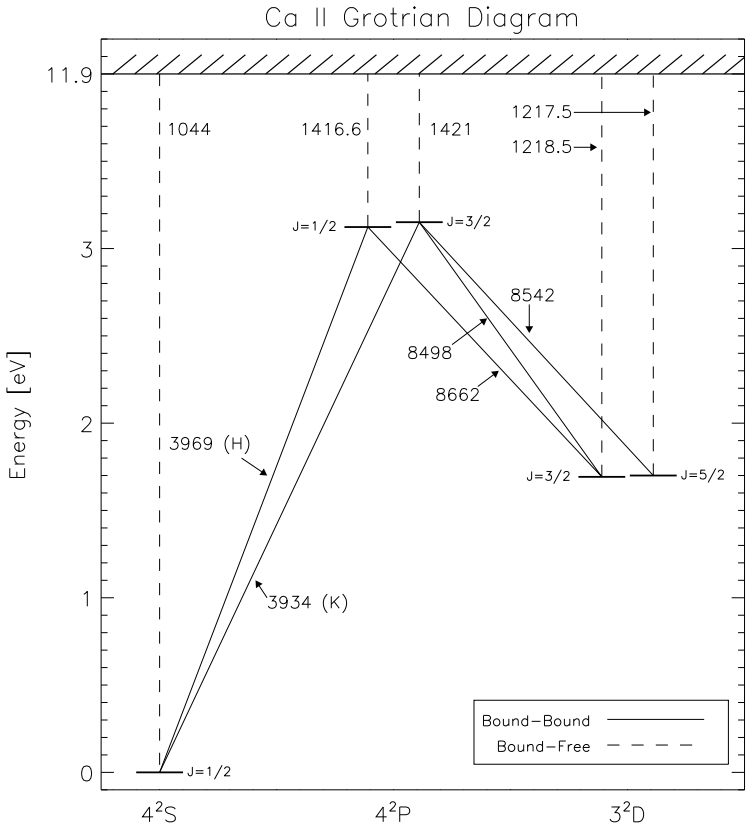

Figure 3.2: Ca II atom model used to compute the calcium lines in **Paper I & II**. Transitions between bound states are marked with solid lines, whereas transitions from a bound state to a free state are represented by dashed lines. The wavelengths of the transitions are given in Å.

In **Paper II** a snapshot from a realistic simulation of the chromosphere is used for the first time to compute synthetic full Stokes spectra. We use a simplified Ca II model atom that consists of 5 bound levels plus ionization continuum, which is illustrated in Fig. 3.2. The populations of the atom are computed in non-LTE evaluating the 3D radiation field as in Leenaarts et al. (2009).

This study is partially motivated by the ongoing debate on requirements of the instrumentation needed to observe chromospheric polarization in the quiet Sun using the Ca II infrared triplet lines. We study the combined effect of spectral resolution and noise on our simulated observations of the chromosphere, considering the following:

- All the polarization is due to the Zeeman effect. We neglect the Hanle effect, which depolarizes or polarizes the light depending on the scattering geometry and changes the ratio between Q and U (Manso Sainz & Trujillo Bueno 2010).

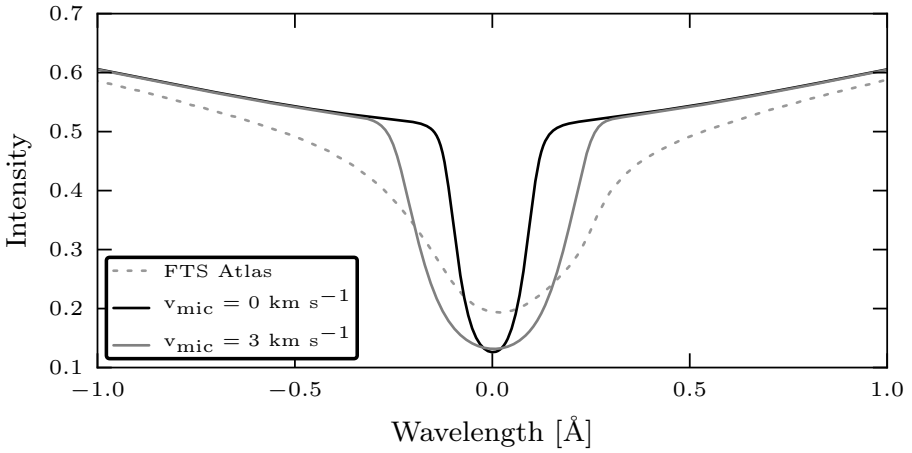

Figure 3.3: Spatially-averaged spectrum from the 3D simulation computed without microturbulence (solid-black line) and with microturbulence (solid-grey line). The solar FTS atlas is plotted for comparison (dashed-line).

- The cores of our synthetic profiles are unrealistically narrow, probably because the model is missing small scale random motions. Conclusions based on these results would underestimate the effect of noise and overestimate the effects of instrumental degradation. Thus, we use microturbulence to broaden our profiles to the same width that is observed in spatially-resolved profiles. In Fig. 3.3 the spatially-averaged spectrum from the 3D simulation with and without microturbulence are compared with the FTS atlas (see Brault & Neckel 1987).
- Instrumental degradation is described by a Gaussian point spread function that operates on the spectra. Additive random noise following a Gaussian distribution is introduced after the convolution with the instrumental profile.

Full Stokes monochromatic images computed from the 3D simulations in the Ca II 8542 Å line are shown in Fig. 3.4. The images have a lot of sharp features that are partially produced by Doppler shifts of the line. As the chromospheric core of the synthetic spectra is unrealistically narrow and strong, intensity variation from Doppler shifts are stronger than in reality.

Our results suggest that current FPI instruments are not sufficiently sensitive to detect circular polarization in the quiet Sun chromosphere using the Ca II 8542 Å line.

3.2 Non-LTE inversions from a 3D MHD simulation

Inversion codes have been extensively used to infer physical quantities from spectrometric and spectropolarimetric data. Inversions involve least-squares fits of the parameters of an atmospheric model, in order to reproduce observed

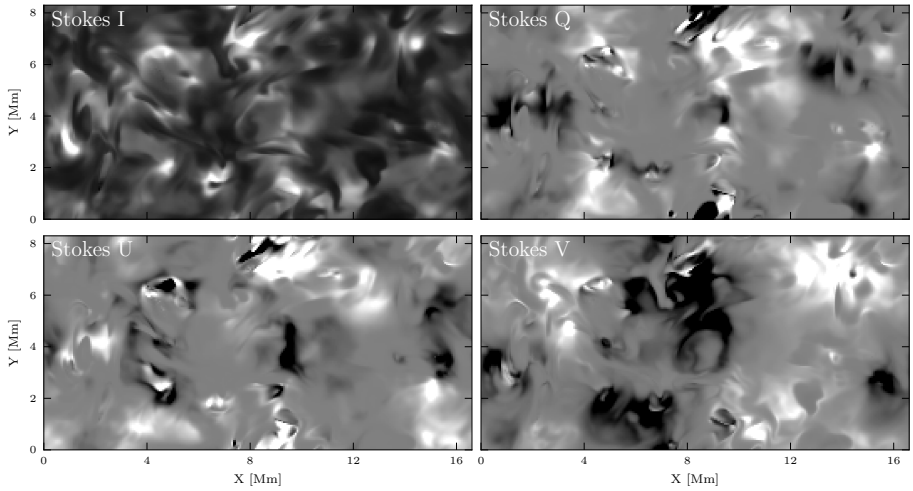

Figure 3.4: Stokes images at -75 mÅ from the core of the line. The Stokes Q and U images are scaled between ± 0.002 and Stokes V is scaled between ± 0.02, relative to continuum intensity.

profiles. In the photosphere, LTE conditions or a Milne-Eddington atmosphere (Ruiz Cobo & del Toro Iniesta 1992; Bellot Rubio & Borrero 2002) are often assumed to simplify and speed up the radiative transfer calculations. Interesting results have been achieved with Milne-Eddington inversions of the chromospheric He I 10830 Å lines (Lagg et al. 2004; Asensio Ramos & Trujillo Bueno 2009; Kuckein et al. 2010), which seem to form in the upper chromosphere (Centeno et al. 2008).

The work presented by Socas-Navarro et al. (2000b) demonstrated that non-LTE inversions of solar observations are possible. Along those lines, Pietarila et al. (2007a) carried out inversions of Ca II 8542 Å data, to measure chromospheric quantities in quiet Sun. More recently, de la Cruz Rodríguez et al. (2010) used the same scheme to carry out inversions on very high resolution observations of a sunspot showing umbral flashes.

However, it is hard to quantify how accurately inversions can provide chromospheric information, with the commonly used assumptions related to the radiative transfer calculations:

- The populations of the levels of the atom are computed in non-LTE assuming plane-parallel geometry.
- Optionally, the computation of populations can be accelerated by neglecting the effects of the velocity field in the outcoming intensity. Thus, fewer azimuthal angles can be used to evaluate the radiation field. Under those conditions, the line profile becomes symmetric and only one half needs to be computed.
- The fitted model is assumed to be in hydrostatic equilibrium to impose consistency between temperature and density.

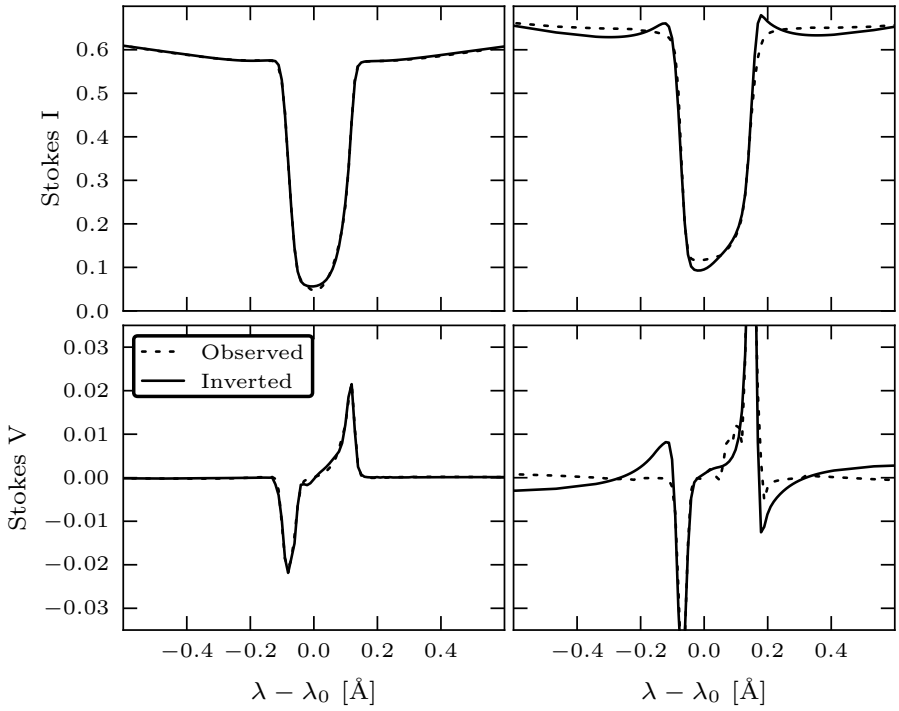

Figure 3.5: Illustrative examples of the fits (solid-line) to the simulated observations. The left column is an example of a good fit, whereas the column on the right illustrates a poorer fit. The top row corresponds to Stokes *I* and the bottom row to Stokes *V*.

In **Paper II**, we use the synthetic observations described in Section 3.1, without microturbulence, to test the Non-LTE Inversion Code based on the Lorien Engine (NICOLE) (Socas-Navarro et al. 2010). The results of the inversion are compared with the quantities from the 3D simulation model. The inversions provide a good estimate of the chromospheric average line-of-sight velocity and magnetic field. 3D non-LTE effects could be affecting temperature, which presents less temperature contrast than the original model. Fig. 3.5 shows two examples of fitted profiles from different pixels. The left panel corresponds to a good fit of the line, whereas the right panel shows a poor fit to the observed profiles. These failures originate the inversion noise that is mentioned in **Paper II**.

3.3 Magnetic fields in chromospheric fibrils

It is widely assumed that fibrils outline chromospheric magnetic fields. Fibrils usually appear around facular regions in Ca II 8542 filtergrams (Rutten 2007), supporting the connection between fibrils and magnetic fields. The goal is to find direct observational evidence of the alignment between magnetic fields

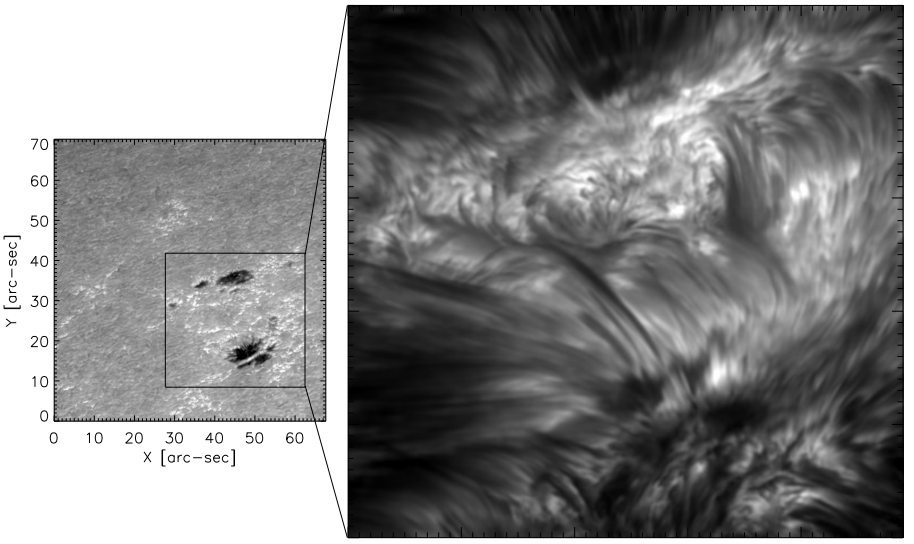

Figure 3.6: Superpenumbral fibrils in the surrounding of two sunspots observed in Ca II 8542 Å. The left panel shows a wideband image of the photosphere whereas the panel on the right corresponds to a narrowband image acquired at -161 mÅ from the core of the line. Images acquired with the SST.

and fibrils. We use two full Stokes datasets acquired in different telescopes with instruments of different type, to measure the orientation of magnetic fields in superpenumbral fibrils. The first dataset was acquired with SPINOR (Socas-Navarro et al. 2006) at the Dunn Solar Telescope (DST), a slit based instrument that allows a large wavelength coverage at a spatial resolution of 0.”6. The second dataset is acquired with SST/CRISP at very high cadence achieving a spatial resolution of 0.”18 but with a limited spectral coverage (see Fig. 3.6). In these datasets, the Stokes Q and U spectra are integrated along the length of the fibrils in order to improve the S/N ratio. The azimuthal direction of the magnetic field (χ) is calculated using the ratio between Stokes Q and U.

$$\tan(2\chi) = \frac{U}{Q} \tag{3.1}$$

Our measurements suggest that fibrils are mostly oriented along the magnetic field direction, however we find evidence of misalignment in some cases. This is both surprising, interesting, and hard to explain. Judge (2006) proposed that if $\beta < 1$ in the chromosphere, then magnetic fields should be almost force-free showing smooth spatial variations. The fine structure seen in chromospheric observations should then primarily be produced by the thermodynamic properties of the gas. Our results could be compatible with this scenario.

4 Data collection and processing

Some of the techniques that are described in this chapter are partially covered in **Paper IV**. However, the *backscatter* problem (see §4.3) and the telescope polarization model (§4.4) have not yet been described in separate publications, but are planned to appear in a forthcoming paper (de la Cruz Rodríguez et al. 2011).

4.1 The SST and CRISP

The data presented in **Paper III** and **Paper IV** was acquired with the Swedish 1-m Solar Telescope (SST) (Scharmer et al. 2003), located on the island of La Palma. Our narrow band data is acquired with the CRisp Imaging Spectropolarimeter (CRISP, Scharmer 2006) which is based on a Fabry-Pérot interferometer that allow for narrow band observations at very high spatial resolution and cadence, providing spectral information at the same time. Atmospheric turbulence is compensated for with adaptive optics (AO), in order to improve image quality. CRISP is mounted in the red beam of the SST (see Fig. 4.1). The light that has been corrected by the AO system passes through the chopper and the pre-filter. Part of the light is reflected to the wideband camera. The other part is modulated with liquid crystals, producing linear combinations of the four stokes parameters. Afterwards, the light beam passes through the CRISP. The p and s polarizations are separated by a beam splitter into two beams that are recorded with separate cameras.

4.2 Flat-fielding the data

Science data taken with a CCD camera can be corrected for pixel-to-pixel inhomogeneities in the response of the camera. Normally, if the CCD is illuminated with a flat and homogeneous light source, intensity variations are mostly produced by pixel-to-pixel sensitivity variations, dirt and fringes. Thus, flat-field calibration images can be acquired to correct for these intensity variations.

A particular problem arises by the presence of time-dependent telescope polarization in the data. Normally, the flat-field images are taken at a different time than the science data. Thus, the amount of polarization introduced by the telescope can differ significantly between science and flat field data. In

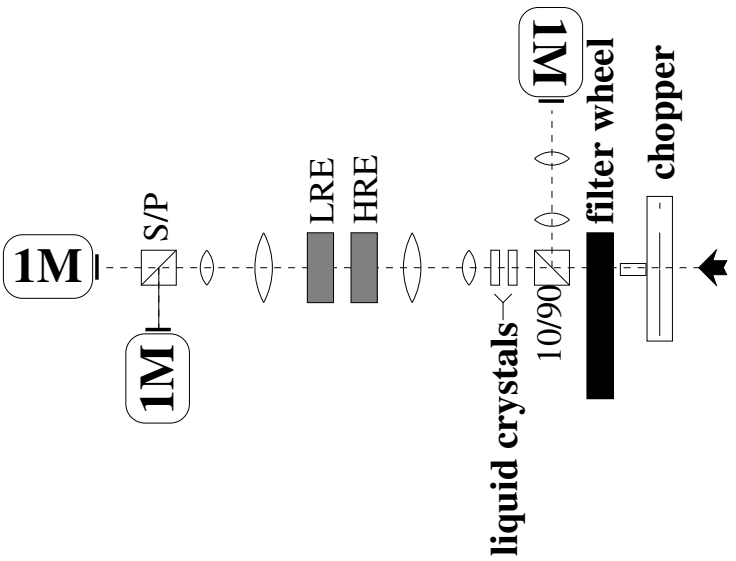

Figure 4.1: Sketch of CRISP at the SST. The incoming light passes the chopper and the pre-filter that isolates the observed spectral line. A beam splitter separates 10 % of the light to the WB camera. The rest of the light passes through the liquid crystals and the Fabry-Pérot etalons (HRE and LRE). Finally a polarizing beam splitter separates the *p* and *s* components of the polarized light to different cameras (1M).

principle this should not be a problem if our cameras could detect Stokes parameters directly. Instead, four linear combinations of Stokes I, Q, U and V are acquired. If seeing were not present, the demodulation of the data could be carried out directly. However, in our case image restoration needs to be done in order to remove residual effects of seeing, not fully compensated for by the AO. As the image reconstruction is done with modulated data, artifacts appear if the flats and science data are not taken at similar times.

Additionally, flat-fielding narrow-band images is more complicated than flat-fielding wideband images. In the case of CRISP, inhomogeneities on the surface of the FPI etalons produce field-dependent wavelength shifts of the transmission profile of the instrument. These are called cavity errors because they introduce variations in the FPI cavities that define the wavelength. The combined effect of cavity errors and the presence of a spectral line, produce field-dependent intensity variations purely introduced by the slope of the spectral line. At the same time, variations in the reflectivity of the etalons across the field-of-view translate into minor variations of the width of the instrumental profile, and therefore also to overall transmission variations. This effect is much smaller than intensity fluctuations produced by cavity errors. Fig. 4.2 illustrates these two effects on the Fe I 6302 Å line.

In **Paper IV** we address the flat-fielding problems produced by time varying telescope polarization and by cavity/reflectivity errors. We propose a method to flat-field polarimetric data affected by telescope polarization. A numerical

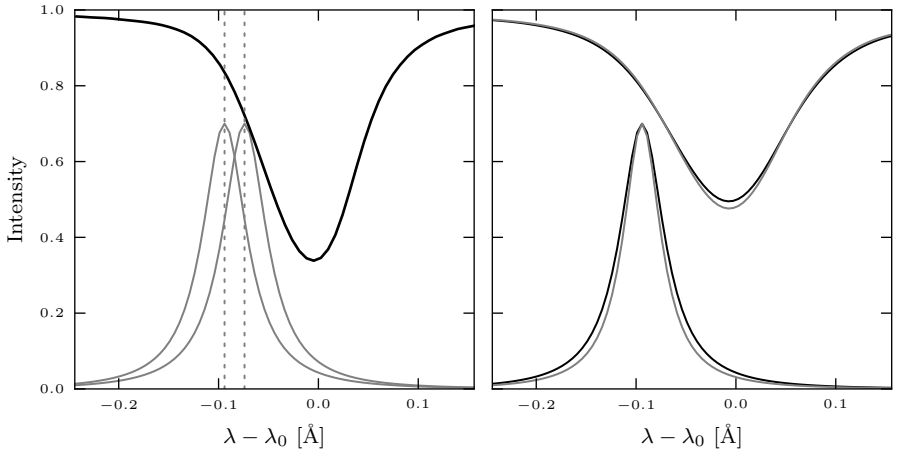

Figure 4.2: *Left:* A theoretical profile of CRISP is plotted with a grey line at two spectral locations. This example illustrates how a shift of the instrumental profile leads to a variation of the intensity on the flanks of a spectral line. The profile has been scaled to the intensity of the line at the location where it is centered. *Right:* Intensity variations produced by reflectivity errors. The line has been convolved with the instrumental profile of the same color.

scheme is used to model and remove the fingerprints of the spectral line from our flat-field data.

4.3 The backscatter problem

The content of this section only applies to observations carried out at infrared wavelengths, and it was motivated by our first observations in Ca II 8542 Å. The methods described here were developed together with Michiel van Noort and it is the main result of my first campaign with CRISP in 2008.

The problem

The CRISP acquisition system includes three back-illuminated CCD cameras (Sarnoff) that can record 35 frames per second. The quantum efficiency of these cameras decreases towards long wavelengths. Above 700 nm the CCD becomes semi-transparent, letting part of the light to pass through. Furthermore, the images show a circuit-like pattern that cannot be removed by traditional dark-field and flat-field corrections, as illustrated in Fig. 4.3.
Examination of pinhole data and flat-fielded data shows that:

1. There is a diffuse additive stray-light contribution in the whole image.
2. The stray-light contribution is much smaller in the circuit pattern and the gain appears to be enhanced.

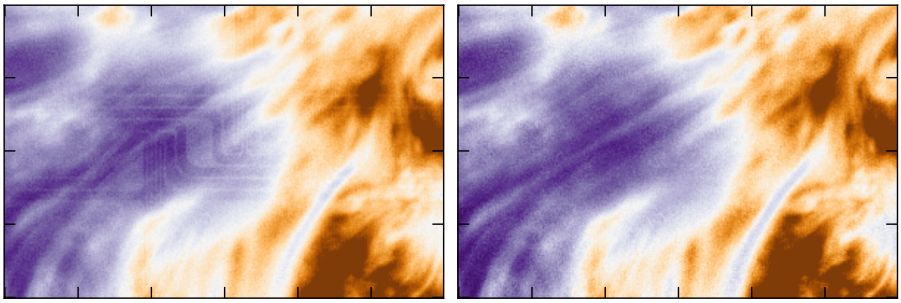

Figure 4.3: *Left:* Subfield of an image that has been traditionally flat-fielded, showing the circuit-like pattern. *Right:* The same subfield corrected using the numerical scheme that is proposed in this section. This colormap is chosen in order to enhance the contrast of fibrils and the electronic circuit.

The model

These problems can be explained by a semi-transparent CCD with a diffusive medium behind it, combined with an electronic circuit located right behind the CCD that is partially reflecting and therefore also less transparent to the scattered light. Fig. 4.4 represents the simplified structure of the camera. Under normal conditions an image recorded with a CCD, I_o, can be described in terms of the dark-field D, the gain factor G_f and the real image I_r:

$$I_o = D + (G_f \cdot I_r) \tag{4.1}$$

However, in the infrared we need a more complicated model:

$$I_o = D + f(1-f)[(G_b G_f I_r) * P]G_b + f G_f I_r \tag{4.2}$$

where f represents the overall fraction of light absorbed by the CCD, G_b is the gain for light illuminating the CCD from the back which should account for the electronic circuit pattern. In the following, we refer to G_b as *backgain*. P is a Point Spread Function (PSF) that describes the scattering properties of the dispersive screen. In the backscatter term we assume that $(1-f)G_f I_r G_b$ is transmitted to the diffusive medium where it is scattered. A fraction of the scattered light returns to the CCD, passing again through the circuit. The cartoon in Fig. 4.4 shows a schematic representation of the structure of the camera and the path followed by the light beam.

The numerical approach

In order to obtain the real intensity I_r, the PSF P, the back-gain G_b and the front-gain G_f must be known. The transparency factor is assumed to be smooth because the properties of the dispersive screen seem to be homogeneous across the field-of-view. This allows us to include f in the

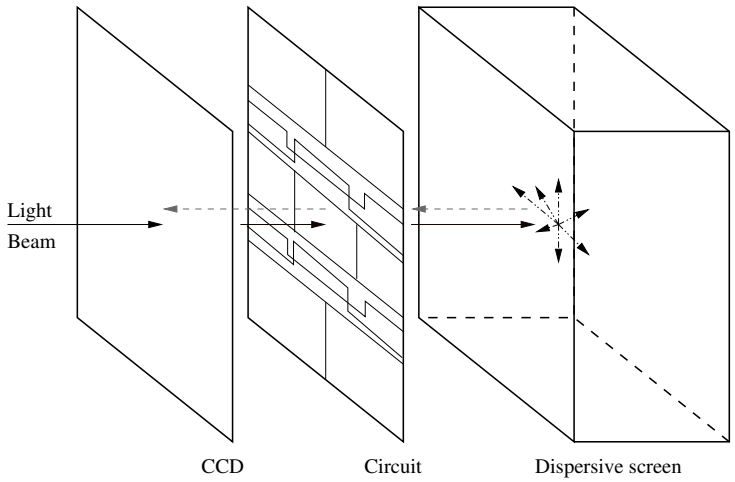

Figure 4.4: Cartoon showing the conceptual model of the camera. The dark arrows indicate the incoming light beam from the telescope and the gray arrows represent the back-scattered light that returns to the CCD.

front and the back gain factors

$$G_{b'} = \sqrt{1-f}\, G_b$$

$$G_{f'} = f G_f,$$

so Eq. 4.2 becomes:

$$I_o = D + G_{b'}[(G_{b'} G_{f'} I_r) * P] + G_{f'} I_r \tag{4.3}$$

This problem is linear and invertible, but a direct inversion would be expensive, given the dimensions of the problem. A numerical approach can be used to iteratively solve the problem. We define

$$\hat{J} = (G_{b'} G_{f'} I_r) * P \tag{4.4}$$

In the first iteration, we initialize $\hat{J}$ assuming that the smearing caused by P is so large that $\hat{I}$ can be approximated by the *average* value of the observed image multiplied with the back gain. The back gain $G_{b'}$ is assumed to be 1 for every pixel in the first iteration. Furthermore, we assume that the product $G_{f'} I_r$ can be estimated from Eq. 4.1 ignoring back scattering, i.e., $G_{f'} I_r \approx I_o - D$. These values are of the same order of magnitude as the final solution, and therefore correspond to a reasonable choice of initialization.

$$\hat{J}_0 \approx \langle G_{b'} G_{f'} I_r \rangle \approx \langle G_{b'} (I_o - D) \rangle, \tag{4.5}$$

where the initial guess of the PSF P represents an angular average obtained from a pinhole image. The small diameter of the pinhole only allows to estimate accurately the central part of the PSF. The wings of our initial guess are

extrapolated using a power-law. The estimate of $G_{f'}I_r$ is then

$$G_{f'}I_r = I_o - D - G_{b'}\hat{J} \tag{4.6}$$

which can be used to compute a new estimate $\hat{J}$. This procedure is iterated, until $G_{f'}I_r$ and I_o are consistent. This new value of $\hat{J}$ is used to improve our estimate of $G_{b'}$, by applying the same procedure to images that contain parts being physically masked ($I_r = 0$), as in Fig. 4.5. In the masked parts where $I_r \equiv 0$ we have,

$$I_o - D - G_{b'}\hat{J} = 0, \tag{4.7}$$

so the back-gain can be computed directly:

$$G_{b'} = \frac{I_o - D}{\hat{J}}. \tag{4.8}$$

Thus, every pixel must have been covered by the mask at least once in a calibration image in order to allow the calculation of the back-gain. With the new $G_{b'}$ we can recompute a new estimate of $G_{f'}I_r$.

We now need to specify a measure that describes how well the data is fitted by the estimate of P and $G_{b'}(P)$. Since both $G_{f'}I_r$ and $G_{b'}$ are computed based on self-consistency, we iteratively need to fit only the parameters of the PSF. We assume that the PSF is circular-symmetric and apply corrections to the PSF at *node* points placed along the radius.

We use Brent's Method described by Press et al. (2002) to minimize our fitness function. This algorithm does not require the computation of derivatives with respect to the free parameters of the problem. When the opaque bars block a region of the CCD, an estimate of the back gain can be calculated for a given PSF according to Eq. 4.8. In our calibration data, the four bars of width L are displaced 0.5 L from one image to the next (see Fig. 4.5). This overlapping provides two different measurements of the back gain on each region of the CCD. However, as the location of the bars changes on each image, the scattered light contribution is different for each of these measurements of the back gain. Our fitness function minimizes the difference between these two measurements of the back gain.

Having thus obtained the PSF P and the back-gain $G_{b'}$, we obtain $G_{f'}$ by recording conventional flats and assuming I_r is a constant in order to obtain $G_{f'}$ from Eq. 4.9.

Results

The numerical scheme described in §4.3 produces the backgain ($G_{b'}$) and an approximate PSF (P) that describes the scattering problem. The results are illustrated in Fig. 4.6. The back gain image shows a background with vertical dark areas in the extended gaps where the circuit pattern is not present. Those hollows probably indicate that the PSF is not perfect, an expected result given

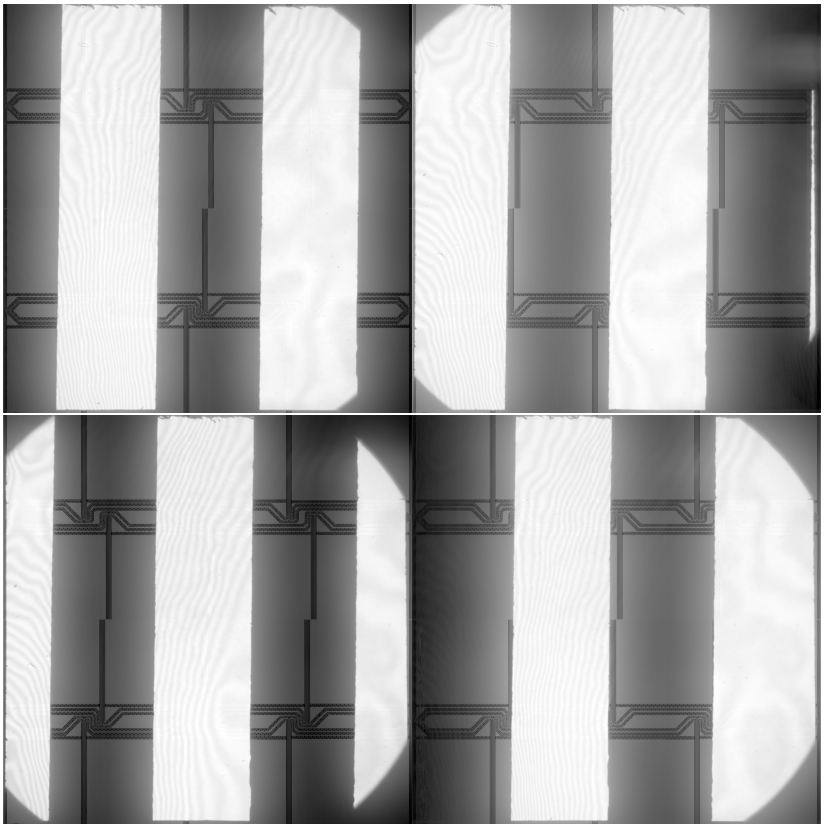

Figure 4.5: Calibration images used to infer the scattering PSF and the backgain of the camera. The bars are displaced image-to-image so every pixel is covered at least once by the black bars. The images are shown with logarithmic intensity scale.

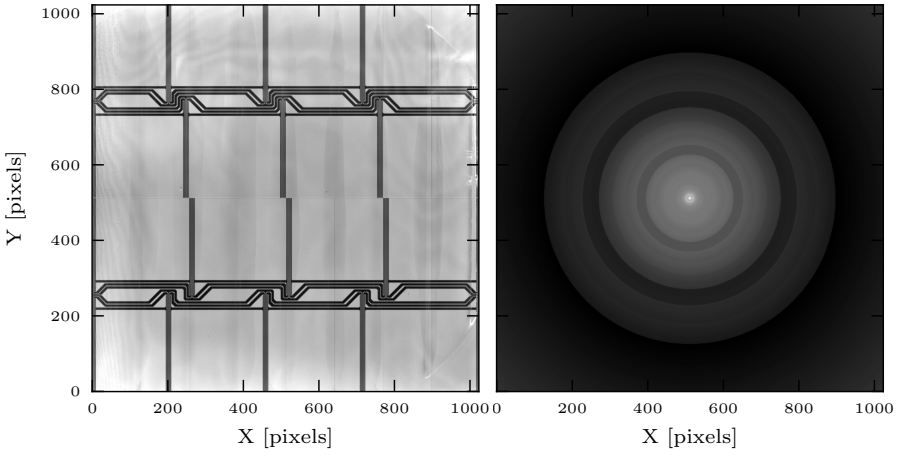

Figure 4.6: *Left:* Fitted back-gain for one of the cameras. *Right:* Circular-symmetric PSF obtained from our fitting routine. The PSF is displayed using a logarithmic scaling.

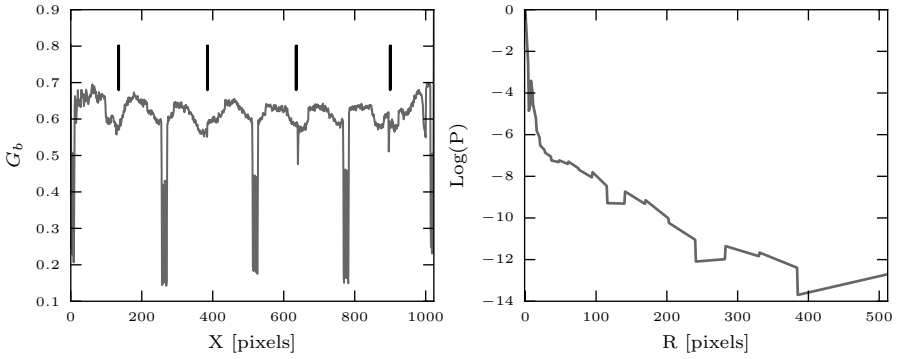

Figure 4.7: *Left:* Values of the back gain along the $x-$axis at $Y = 450$. The black markers indicate the location of the hollows resulting from the limited accuracy of the PSF. *Right:* The radial variation of P, represented in logarithmic scale.

the assumptions imposed on the shape of the PSF: it is constant over the entire field of view, and only radial variations are allowed. The PSF has extended wings that complicate the convergence of the solution, given the nature of our calibration data: the spacing between *bars* in the horizontal direction is a limiting factor to constrain such extended wings.

The flat-fielding method described in the previous sections has been implemented in the image reconstruction code MOMFBD (van Noort et al. 2005) and is only used when a back-gain and a PSF are provided. Eq. 4.9 is reordered to correct the science data.

$$G_f I_r = I_o - G_{b'}\left[(G_{b'} G_{f'} I_r) * P\right] - D \tag{4.9}$$

Since $G_{f'} I_r$ appears in both sides of the equation, some iterations are needed to estimate the term $G_{b'}\left[(G_{b'} G_{f'} I_r) * P\right]$, which is a computationally expensive process if thousands of images are flat-fielded.

In Fig. 4.3 we show a frame that has been traditionally flat-fielded (left panel) and the same image flat-fielded according to Eq. 4.9. The method described in the present work removes the electronic circuit pattern from the images. The assumption imposed on the PSF allows us to estimate the back gain with limited accuracy, as is obvious from the Fig. 4.7. The uncertainties present in the PSF and the back gain are likely to affect the contrast of the corrected images.

Figure 4.8: The 1-m polarizer mounted on the entrance lens of the SST. Calibration datasets were acquired during entire days to characterize the polarimetric properties of the telescope.

4.4 Telescope polarization model at 854.2 nm

The turret of the SST contains optical elements that polarize the incoming light. Selbing (2005) studied the polarizing properties of the telescope at 630.2 nm and proposed a theoretical model to characterize its temporal variation. Calibration images have been taken using a 1-m polarizer mounted at the entrance lens of the SST (see Fig. 4.8). The polarizer rotates 360° in steps of 5° and several frames are acquired on each polarizer angle. Data was adquired during the whole day. These data were used to determine the parameters of the model proposed by Selbing (2005) at 854.2 nm.

Telescope model

Each polarizing optical element of the telescope is represented with a Mueller matrix. Mueller matrices of mirrors are noted with M and have two free parameters. Assuming a wave that propagates along the z axis and oscillates in the $x-y$ plane, the parameters are the de-attenuation term (R) between the xy components of the electromagnetic wave and the phase retardance (δ) produced by the mirror (see Selbing 2005). This form of M assumes that Q is perpendicular to the plane of incidence. In the more general case, M can be

written as,

$$M(R,\delta) = \begin{pmatrix} \frac{1}{2}+\frac{1}{2}R & \frac{1}{2}-\frac{1}{2}R & 0 & 0 \\ \frac{1}{2}-\frac{1}{2}R & \frac{1}{2}+\frac{1}{2}R & 0 & 0 \\ 0 & 0 & -\sqrt{R}\cos(\frac{\pi}{180}\delta) & -\sqrt{R}\sin(\frac{\pi}{180}\delta) \\ 0 & 0 & \sqrt{R}\sin(\frac{\pi}{180}\delta) & -\sqrt{R}\cos(\frac{\pi}{180}\delta) \end{pmatrix}$$

$R(\alpha)$ corresponds to a rotation to a new coordinate frame, rotated an angle α.

$$R(\alpha) = \begin{pmatrix} 1 & 0 & 0 & 0 \\ 0 & \cos(\frac{\pi}{90}\alpha) & \sin(\frac{\pi}{90}\alpha) & 0 \\ 0 & -\sin(\frac{\pi}{90}\alpha) & \cos(\frac{\pi}{90}\alpha) & 0 \\ 0 & 0 & 0 & 1 \end{pmatrix}$$

L represents the entrance Lens. The form of the lens matrix represents a composite of random retarders, so it modulates the light without (de)polarizing it. The reference for Q is aligned with the 1m linear polarizer axis and the values of the matrix are measured in that frame.

$$L = \begin{pmatrix} 1 & 0 & 0 & 0 \\ 0 & A & B & -C \\ 0 & B & D & E \\ 0 & C & -E & (A+D-1) \end{pmatrix}$$

The model is built using the Mueller matrix of each polarizing element in the telescope (Eq. 4.10), as a function of the azimuth (φ) and elevation (θ) angles of the Sun at the time of the observation. We have included the conversion factor from degrees to radians in the matrices, thus all the angles are given in degrees.

$$M_{tel}(\theta,\varphi) = R_{f+} \cdot M_s \cdot M_f \cdot R_{f-} \cdot R_{az} \cdot M_{az} \cdot R_{el} \cdot M_{el} \cdot L \tag{4.10}$$

$$L = \begin{pmatrix} 1 & 0 & 0 & 0 \\ 0 & c_0 & c_1 & -c_2 \\ 0 & c_1 & c_3 & c_4 \\ 0 & c_2 & -c_4 & c_0+c_3-1 \end{pmatrix}$$

$$R_{el} = \begin{pmatrix} 1 & 0 & 0 & 0 \\ 0 & \cos(\pi(1+\frac{\theta}{90})) & \sin(\pi(1+\frac{\theta}{90})) & 0 \\ 0 & -\sin(\pi(1+\frac{\theta}{90})) & \cos(\pi(1+\frac{\theta}{90})) & 0 \\ 0 & 0 & 0 & 1 \end{pmatrix}$$

$$M_{az} = \begin{pmatrix} \frac{1}{2}+\frac{1}{2}c_5 & \frac{1}{2}-\frac{1}{2}c_5 & 0 & 0 \\ \frac{1}{2}-\frac{1}{2}c_5 & \frac{1}{2}+\frac{1}{2}c_5 & 0 & 0 \\ 0 & 0 & -\sqrt{c_5}\cos(\frac{\pi}{180}c_6) & -\sqrt{c_5}\sin(\frac{\pi}{180}c_6) \\ 0 & 0 & \sqrt{c_5}\sin(\frac{\pi}{180}c_6) & -\sqrt{c_5}\cos(\frac{\pi}{180}c_6) \end{pmatrix} = M_{el}$$

$$R_{az} = \begin{pmatrix} 1 & 0 & 0 & 0 \\ 0 & \cos(\frac{\pi}{90}\varphi) & \sin(\frac{\pi}{90}\varphi) & 0 \\ 0 & -\sin(\frac{\pi}{90}\varphi) & \cos(\frac{\pi}{90}\varphi) & 0 \\ 0 & 0 & 0 & 1 \end{pmatrix}$$

$$R_{f+} = \begin{pmatrix} 1 & 0 & 0 & 0 \\ 0 & \cos(\frac{\pi}{90}c_{11}) & \sin(\frac{\pi}{90}c_{11}) & 0 \\ 0 & -\sin(\frac{\pi}{90}c_{11}) & \cos(\frac{\pi}{90}c_{11}) & 0 \\ 0 & 0 & 0 & 1 \end{pmatrix}$$

$$R_{f-} = \begin{pmatrix} 1 & 0 & 0 & 0 \\ 0 & \cos(-\frac{\pi}{90}c_{11}) & -\sin(-\frac{\pi}{90}c_{11}) & 0 \\ 0 & \sin(-\frac{\pi}{90}c_{11}) & \cos(-\frac{\pi}{90}c_{11}) & 0 \\ 0 & 0 & 0 & 1 \end{pmatrix}$$

$$M_f = \begin{pmatrix} \frac{1}{2}+\frac{1}{2}c_7 & \frac{1}{2}-\frac{1}{2}c_7 & 0 & 0 \\ \frac{1}{2}-\frac{1}{2}c_7 & \frac{1}{2}+\frac{1}{2}c_7 & 0 & 0 \\ 0 & 0 & -\sqrt{c_7}\cos(\frac{\pi}{180}c_8) & -\sqrt{c_7}\sin(\frac{\pi}{180}c_8) \\ 0 & 0 & \sqrt{c_7}\sin(\frac{\pi}{180}c_8) & -\sqrt{c_7}\cos(\frac{\pi}{180}c_8) \end{pmatrix}$$

$$M_s = \begin{pmatrix} \frac{1}{2}+\frac{1}{2}c_9 & \frac{1}{2}-\frac{1}{2}c_9 & 0 & 0 \\ \frac{1}{2}-\frac{1}{2}c_9 & \frac{1}{2}+\frac{1}{2}c_9 & 0 & 0 \\ 0 & 0 & -\sqrt{c_9}\cos(\frac{\pi}{180}c_{10}) & -\sqrt{c_9}\sin(\frac{\pi}{180}c_{10}) \\ 0 & 0 & \sqrt{c_9}\sin(\frac{\pi}{180}c_{10}) & -\sqrt{c_9}\cos(\frac{\pi}{180}c_{10}) \end{pmatrix}$$

where,

- c_0, c_1, c_2, c_3 and c_4 are the parameters of the entrance lens.
- c_5 and c_6 are the de-attenuation and phase difference of the azimuth mirror.
- c_7 and c_8 are the de-attenuation and phase difference of the elevation mirror.
- c_9 and c_{10} are the de-attenuation and phase difference of the Schupmann mirror.
- c_{11} is the angle of the field mirror.

We used a Levenberg-Marquardt algorithm (see Press et al. 2002) to fit the 12 parameters (c) of the model to the calibration data. The orthogonality of 1-m polarizer states is maximum every 45°. Thus only four angles are used in our fitting routine: $0°, 45°, 90°, 135°$. The quality of the fit does not improve substantially by including data from other angles. The derived parameters of the Mueller matrix of the telescope are shown in Table 4.1. Unfortunately, we have not been able to analyze the errors due to time constraints.

The quality of the calibration data is limited by the quality of the 1-m linear polarizer. The problem is posed in such a way, that we cannot measure the extinction ratio of the polarizer and the parameters of the lens at the same time. In our case, the polarizer has a significant leak of unpolarized light at 854.2 nm. Using small samples of the sheets used to construct the 1-m polarizer, we have estimated the extinction ratio of the 1-m polarizer to be approximately 0.4, so the parameters of the lens have been determined assuming that value.

Table 4.1: *Parameters of the telescope model obtained from calibration data.*

Parameter	Fitted value
c_0	$+9.596161 \cdot 10^{-1}$
c_1	$-2.541791 \cdot 10^{-3}$
c_2	$-8.337375 \cdot 10^{-3}$
c_3	$+9.640901 \cdot 10^{-1}$
c_4	$-1.875988 \cdot 10^{-2}$
c_5	$+9.164327 \cdot 10^{-1}$
c_6	$+1.465364 \cdot 10^{1}$
c_7	$+1.017471 \cdot 10^{0}$
c_8	$+1.326977 \cdot 10^{0}$
c_9	$+1.010035 \cdot 10^{0}$
c_{10}	$-1.592178 \cdot 10^{0}$
c_{11}	$+4.000000 \cdot 10^{0}$

In Fig. 4.9 the time dependence of the Mueller matrix of the telescope is shown along a whole day. The largest changes occur when the sun is close to zenith, because of the rapid movement of the telescope. The linear polarization reference is defined by the first mirror after the lens, however this is not very useful in practice because the turret introduces image rotation along the day. Instead, we use the solar north as a reference for positive Q by applying an extra rotation to M_{tel}. The rotation is produced by reflections inside the turret and by the variation of the angle between the first mirror after the entrance lens and the solar north along the day. The angle between the first mirror and the solar north (β) is computed by the telescope software every 30 seconds. Eq. 4.11 transforms the reference of Q and U to solar North-South axis.

$$M'_{tel} = M_{tel} \cdot R(\beta) \tag{4.11}$$

The only remaining question is the location of the solar north in our science images. At this point, Stokes Q and U are relative to the solar North-South axis, but there is no coupling between the polarization calibration and the image orientation. The angle between solar north and the horizontal on the optical table is

$$\omega = \varphi - \theta - \mathrm{TC} - \beta, \tag{4.12}$$

where φ is the azimuth, θ is the elevation, TC is the *table constant* and β is the tilt angle between first mirror in the telescope and solar north. The table constant is relative to the orientation of the optical table and it is $+48^\circ$ for the current setup.

Fig. 4.10 and 4.11 show monochromatic Stokes I, Q, U, V images acquired in Ca II 8542 Å. The dataset has been restored using the de-scattering

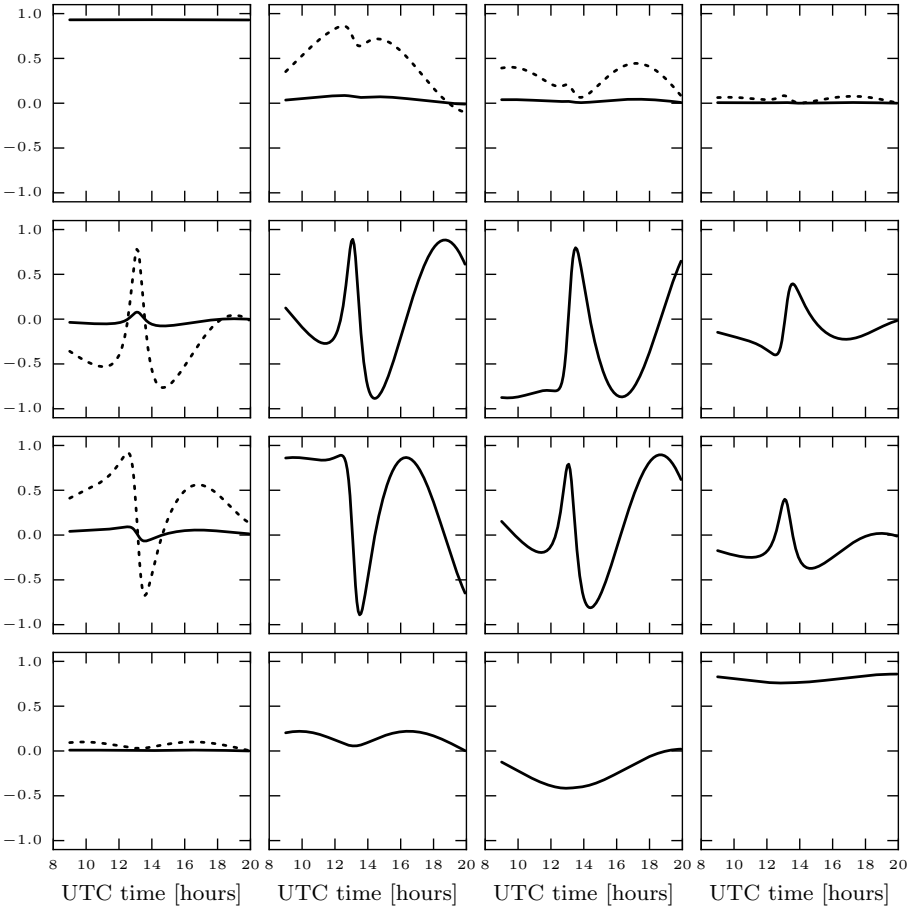

Figure 4.9: Mueller matrix of the telescope computed for 2009-05-28. Each panel corresponds to one element of the matrix placed in the same order. The solid line represents the time dependence of each value. The dashed line is the same value multiplied by a factor 10.

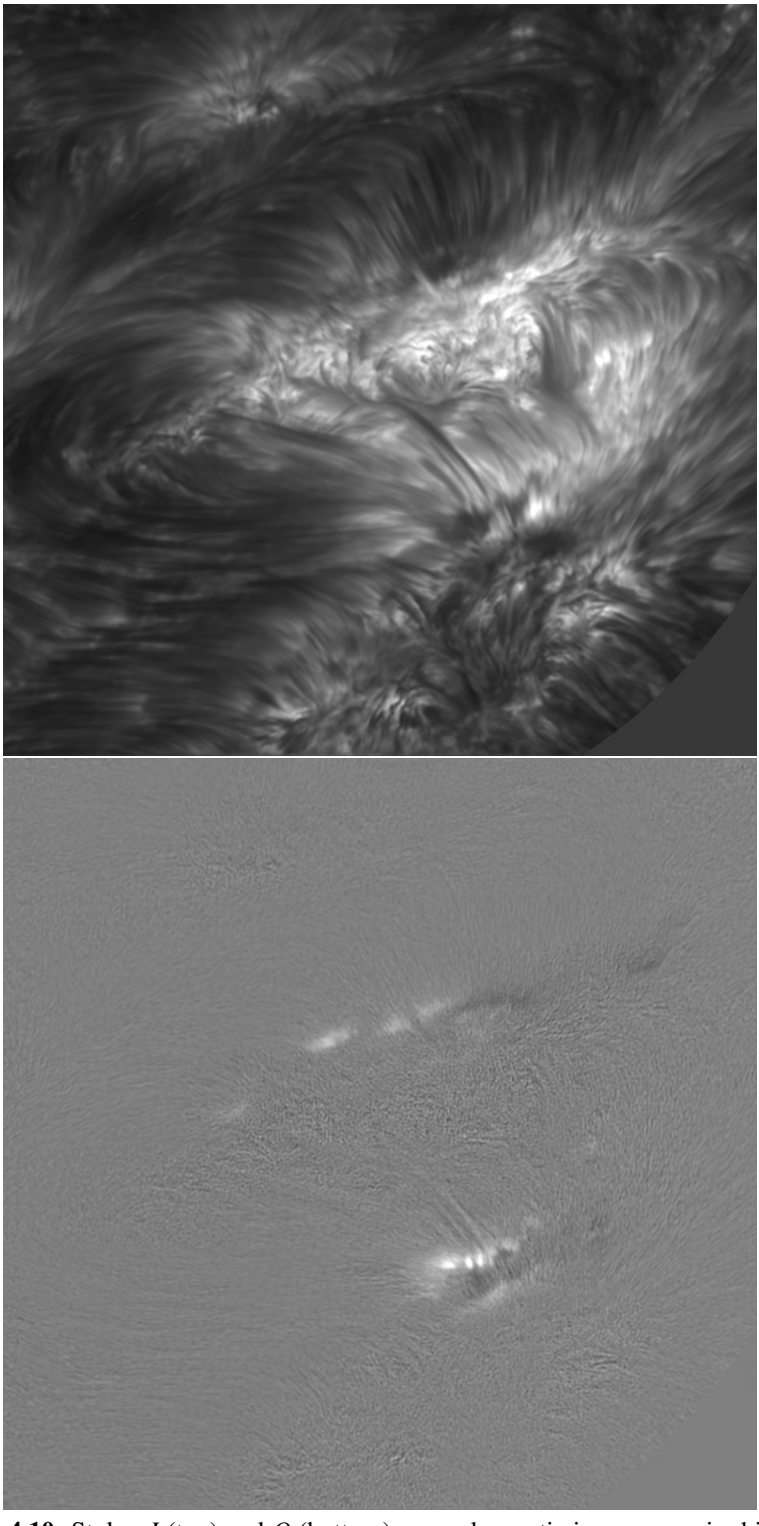

Figure 4.10: Stokes I (top) and Q (bottom) monochromatic images acquired in Ca II 8542 Å at -161 mÅ from the core of the line. Stokes Q is scaled to $\pm 3\%$ of the continuum intensity.

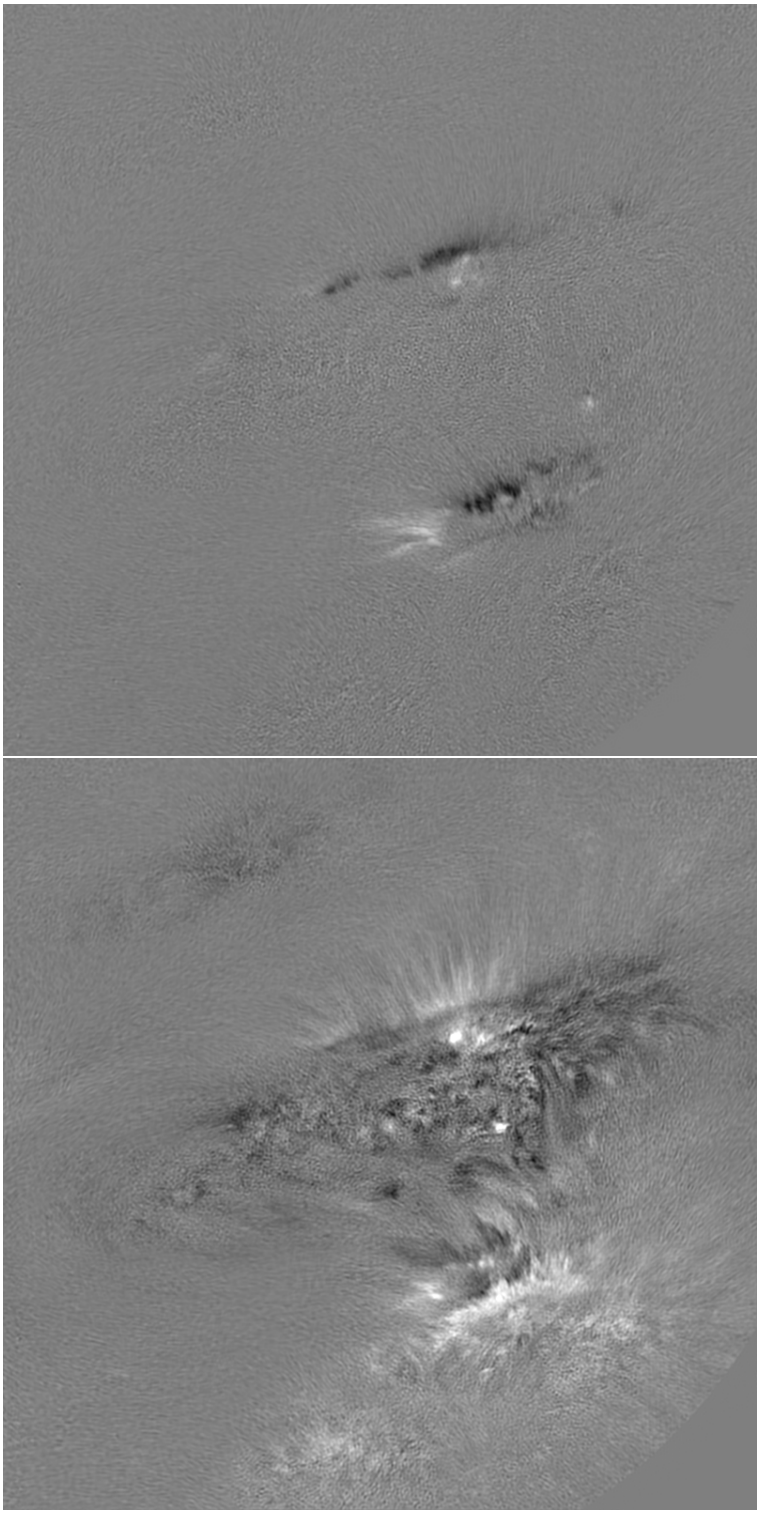

Figure 4.11: Stokes U (top) and V (bottom) monochromatic images acquired in Ca II 8542 Å at -161 mÅ from the core of the line. The images are scaled to $\pm 3\%$ of the continuum intensity.

scheme from §4.3 and the telescope model presented in the current section. This dataset is used in **Paper III** to measure the alignment between fibrils and magnetic field.

5 Summary of papers

Paper I: Solar velocity references from 3D HD photospheric models

The aim of this paper is to help observers to accurately calibrate line-of-sight velocities. We use a 3D hydrodynamic simulation of the solar photosphere to compute spatially-averaged spectra that can be used as absolute velocity references. The line profiles are computed at different heliocentric angles, from disk center towards the limb.

Our synthetic profiles are compared with observational data and several experiments are computed to estimate the accuracy of our method, which has an estimated error of approximately ± 50 m s^{-1} at disk center. Our tests suggest that the variation of the bisectors towards the limb, is mostly produced by the 3D topology of the photosphere.

In Paper I, I carried out all the calculations and prepared all figures. The collaborators contributed to the scientific discussion and assisted in the writing.

Paper II: Non-LTE inversions from a 3D MHD chromospheric model

In Paper II, we create synthetic full-Stokes observations in Ca II 8542 Å from a snapshot of a realistic 3D simulation of the solar atmosphere. These observations are used to estimate the amplitude of the Stokes profiles in quiet Sun. We discuss the effect that spectral degradation and noise have on our observations and discuss possible requirements for future instrumentation.

In the second part of the paper, we use our synthetic observations to test our non-LTE inversion code. The fitted model is compared with the quantities from the 3D snapshot. We conclude that the inversion code is able to estimate the average chromospheric value of magnetic field, line-of-sight and velocity. 3D non-LTE effects seem to affect the fitted temperature that in general presents less contrast than the original model.

My contribution to Paper II was to compute the full-Stokes simulated observations using the population densities provided by J. Leenaarts and carried out the Non-LTE inversions of the data. For that purpose I wrote an improved parallel version of NICOLE using MPI and a *master-slave* scheme. I prepared the main structure of the text in the paper and created all the figures.

Paper III: Are solar chromospheric fibrils tracing the magnetic field?

The aim of this letter is to obtain an observational evidence that confirms the alignment between chromospheric fibrils and magnetic field. We use two datasets acquired with SST/CRISP and DST/SPINOR to measure the orientation of magnetic field along chromospheric fibrils. We find that many fibrils are aligned with magnetic field, however in both datasets there are evidences of misalignment in some cases.

For this paper I provide a restored dataset from CRISP, compensated for telescope polarization and with a calibrated reference for Stokes Q and U. My co-author prepared the SPINOR data and contributed to the scientific discussion and the writing.

Paper IV: Stokes imaging polarimetry using image restoration at the Swedish 1-m Solar Telescope II: A calibration strategy for Fabry-Pérot based instruments

The image restoration step that is applied to our data, decouples the 1-to-1 relation between the pixels of the CCD. When image reconstruction is applied to data showing sharp spatial variations produced by intrumentation, artifacts can appear. We propose a flat-fielding scheme for polarimetric data acquired with CRISP. We discuss the effect of the polarization introduced by the telescope and the optical setup in our flat-field data. In order to correct for spurious intensity fluctuations from cavity errors and reflectivity errors, we use a numerical framework that allows to model the spectral line on each pixel of the CCD.

My contribution to this paper was to implement the numerical scheme that is used to model the flat fields and remove the intensity fluctuations produced by cavity errors and reflectivity errors. I contributed to the scientific discussion and prepared some of the figures in the paper.

6 Publications not included in this thesis

- **CRISP Spectropolarimetric Imaging of Penumbral Fine Structure**
  Scharmer G. B., Narayan G., Hillberg T., de la Cruz Rodríguez J., Löfdahl M. G., Kiselman D., Sütterlin P., van Noort M., Lagg A., 2008, ApJ, 689, L69.

- **The magnetic SW Sextantis star RXJ1643.7+3402**
  Rodríguez-Gil P., Martínez-Pais I. G., de la Cruz Rodríguez J., 2009, MNRAS, 395, 973.

- **High-order aberration compensation with Multi-frame Blind Deconvolution and Phase Diversity image restoration techniques**
  Scharmer G. B., Löfdahl M. G., van Werkhoven T. I. M., de la Cruz Rodríguez J., 2010, A&A, 521, A68

- **Observation and analysis of chromospheric magnetic fields**
  de la Cruz Rodríguez J., Socas-Navarro H., van Noort M., Rouppe van der Voort L., to appear in Proceedings of the 25th NSO Workshop: Chromospheric Structure and Dynamics, Memorie della Societa' Astronomica Italiana.

Acknowledgements

I gratefully acknowledge the Institute for Solar Physics of the Royal Swedish Academy of Sciences and the USO-SP Graduate School for Solar Physics for giving me a position in science in a prosperous academic environment. I especially value the scientific discussions with my collaborators **Hector Socas-Navarro**, **Michiel van Noort** and **Roald Schnerr** from whom I learned so much. I have benefited from the assistance and advice provided by my supervisors **Dan Kiselman, Göran Scharmer** and **Mats Carlsson**. I also appreciate the help from **Mats Löfdahl** who kindly commented on the manuscript of my thesis.

My thanks to **Tiago Pereira** and to the **Institute of theoretical Astrophysics** of Oslo for providing the 3D simulations used in my research. I especially enjoyed being in contact with **Luc Rouppe van der Voort** who shared observational data and also his knowledge with me. I also acknowledge **Pit Sütterlin** and **Rolf Kever** who have been of great help at the SST on La Palma. Here in Stockholm it has been great to share the office (and pubs) with **Vasco Henriques**.

I gratefully acknowledge the financial support of the European Commission during the first three years of my PhD. Many thanks to my institute for extending my financial support during the last months of my research.

Bibliography

Asensio Ramos, A. & Trujillo Bueno, J. 2009, in Astronomical Society of the Pacific Conference Series, Vol. 405, Solar Polarization 5: In Honor of Jan Stenflo, ed. S. V. Berdyugina and K. N. Nagendra and R. Ramelli, 281

Asplund, M., Nordlund, Å., Trampedach, R., & Stein, R. F. 2000, A&A, 359, 743

Bahng, J. & Schwarzschild, M. 1961, ApJ, 134, 312

Balthasar, H. 1988, A&AS, 72, 473

Beckers, J. M. 1977, ApJ, 213, 900

Bellot Rubio, L. R., Balthasar, H., & Collados, M. 2004, A&A, 427, 319

Bellot Rubio, L. R. & Borrero, J. M. 2002, A&A, 391, 331

Bellot Rubio, L. R., Tritschler, A., & Martínez Pillet, V. 2008, ApJ, 676, 698

Borrero, J. M. & Bellot Rubio, L. R. 2002, A&A, 385, 1056

Brault, J. W. & Neckel, H. 1987, Spectral Atlas of Solar Absolute Disk-averaged and Disk-Center Intensity from 3290 to 12510 Å, ftp://ftp.hs.uni-hamburg.de/pub/outgolng/FTS-Atlas

Cacciani, A., Briguglio, R., Massa, F., & Rapex, P. 2006, Celestial Mechanics and Dynamical Astronomy, 95, 425

Carlsson, M., Hansteen, V. H., & Gudiksen, B. V. 2010, ArXiv e-prints 1001.1546

Carlsson, M. & Stein, R. F. 1995, ApJ, 440, L29

Cauzzi, G., Reardon, K., Rutten, R. J., Tritschler, A., & Uitenbroek, H. 2009, A&A, 503, 577

Cauzzi, G., Reardon, K. P., Uitenbroek, H., et al. 2008, A&A, 480, 515

Cauzzi, G., Reardon, K. P., Vecchio, A., Janssen, K., & Rimmele, T. 2007, in Astronomical Society of the Pacific Conference Series, Vol. 368, The Physics of Chromospheric Plasmas, ed. P. Heinzel, I. Dorotovič, & R. J. Rutten, 127

Centeno, R., Trujillo Bueno, J., Uitenbroek, H., & Collados, M. 2008, ApJ, 677, 742

Cheung, M. C. M., Schüssler, M., & Moreno-Insertis, F. 2007, A&A, 461, 1163

de la Cruz Rodríguez, J., Socas-Navarro, H., van Noort, M., & Rouppe van der Voort, L. 2010, ArXiv e-prints 1004.0698

de la Cruz Rodríguez, J., van Noort, M., & Schnerr, R. 2011, In preparation

De Pontieu, B., McIntosh, S., Hansteen, V. H., et al. 2007, PASJ, 59, 655

Dravins, D., Lindegren, L., & Nordlund, A. 1981, A&A, 96, 345

Fossum, A. & Carlsson, M. 2005, in ESA Special Publication, Vol. 600, The Dynamic Sun: Challenges for Theory and Observations

Franz, M. & Schlichenmaier, R. 2009, A&A, 508, 1453

Hansteen, V. H., Carlsson, M., & Gudiksen, B. 2007, in Astronomical Society of the Pacific Conference Series, Vol. 368, The Physics of Chromospheric Plasmas, ed. P. Heinzel, I. Dorotovič, & R. J. Rutten, 107

Hansteen, V. H., De Pontieu, B., Rouppe van der Voort, L., van Noort, M., & Carlsson, M. 2006, ApJ, 647, L73

Judge, P. 2006, in Astronomical Society of the Pacific Conference Series, Vol. 354, Solar MHD Theory and Observations: A High Spatial Resolution Perspective, ed. J. Leibacher, R. F. Stein, & H. Uitenbroek, 259

Judge, P. G., Tritschler, A., Uitenbroek, H., et al. 2010, ApJ, 710, 1486

Kahn, F. D. 1961, ApJ, 134, 343

Kuckein, C., Centeno, R., & Martinez Pillet, V. 2010, ArXiv e-prints 1010.4260

Lagg, A., Woch, J., Krupp, N., & Solanki, S. K. 2004, A&A, 414, 1109

Langangen, Ø., Carlsson, M., Rouppe van der Voort, L., Hansteen, V., & De Pontieu, B. 2008, ApJ, 673, 1194

Langangen, Ø., Carlsson, M., Rouppe van der Voort, L., & Stein, R. F. 2007, ApJ, 655, 615

Leenaarts, J., Carlsson, M., Hansteen, V., & Rouppe van der Voort, L. 2009, ApJ, 694, L128

Leenaarts, J., Carlsson, M., Hansteen, V., & Rutten, R. J. 2007, A&A, 473, 625

Leighton, R. B., Noyes, R. W., & Simon, G. W. 1962, ApJ, 135, 474

Manso Sainz, R. & Trujillo Bueno, J. 2010, ApJ, 722, 1416

Martinez Pillet, V., Lites, B. W., & Skumanich, A. 1997, ApJ, 474, 810

Meyer, F. & Schmidt, H. U. 1968, Mitteilungen der Astronomischen Gesellschaft Hamburg, 25, 194

Montesinos, B. & Thomas, J. H. 1997, Nature, 390, 485

Ortiz, A., Bellot Rubio, L. R., & Rouppe van der Voort, L. 2010, ApJ, 713, 1282

Pietarila, A., Socas-Navarro, H., & Bogdan, T. 2007a, ApJ, 670, 885

Pietarila, A., Socas-Navarro, H., & Bogdan, T. 2007b, in Astronomical Society of the Pacific Conference Series, Vol. 368, The Physics of Chromospheric Plasmas, ed. P. Heinzel, I. Dorotovič, & R. J. Rutten, 139

Press, W. H., Teukolsky, S. A., Vetterling, W. T., & Flannery, B. P. 2002, Numerical recipes in C++: The art of scientific computing, 2nd edn. (Cambridge University Press)

Priest, E. R. 1982, Geophysics and Astrophysics Monographs, Vol. 21, Solar magneto-hydrodynamics (Dordrecht: D. Reidel Pub. Co.)

Rouppe van der Voort, L., Leenaarts, J., De Pontieu, B., Carlsson, M., & Vissers, G. 2009, ApJ, 705, 272

Rouppe van der Voort, L. H. M., De Pontieu, B., Hansteen, V. H., Carlsson, M., & van Noort, M. 2007, ApJ, 660, L169

Ruiz Cobo, B. & del Toro Iniesta, J. C. 1992, ApJ, 398, 375

Rutten, R. J. 2006, in Astronomical Society of the Pacific Conference Series, Vol. 354, Solar MHD Theory and Observations: A High Spatial Resolution Perspective, ed. J. Leibacher, R. F. Stein, & H. Uitenbroek, 276

Rutten, R. J. 2007, in Astronomical Society of the Pacific Conference Series, Vol. 368, The Physics of Chromospheric Plasmas, ed. P. Heinzel, I. Dorotovič, & R. J. Rutten, 27

Sanchez Almeida, J. & Lites, B. W. 1992, ApJ, 398, 359

Scharmer, G. B. 2006, A&A, 447, 1111

Scharmer, G. B. 2008, Physica Scripta Volume T, 133, 014015

Scharmer, G. B., Bjelksjö, K., Korhonen, T. K., Lindberg, B., & Petterson, B. 2003, in Society of Photo-Optical Instrumentation Engineers (SPIE) Conference Series, Vol. 4853, Innovative Telescopes and Instrumentation for Solar Astrophysics, ed. S. L. Keil & S. V. Avakyan, 341–350

Scharmer, G. B., Gudiksen, B. V., Kiselman, D., Löfdahl, M. G., & Rouppe van der Voort, L. H. M. 2002, Nature, 420, 151

Scharmer, G. B., Narayan, G., Hillberg, T., et al. 2008, ApJ, 689, L69

Scharmer, G. B. & Spruit, H. C. 2006, A&A, 460, 605

Selbing, J. 2005, Master's thesis, Stockholm University

Shchukina, N. & Trujillo Bueno, J. 2001, ApJ, 550, 970

Socas-Navarro, H., de la Cruz Rodríguez, J., Asensio-Ramos, A., Trujillo-Bueno, J., & Ruiz-Cobo, B. 2010, in preperation

Socas-Navarro, H., Elmore, D., Pietarila, A., et al. 2006, Sol. Phys., 235, 55

Socas-Navarro, H., Trujillo Bueno, J., & Ruiz Cobo, B. 2000a, Science, 288, 1396

Socas-Navarro, H., Trujillo Bueno, J., & Ruiz Cobo, B. 2000b, ApJ, 530, 977

Solanki, S. K. & Montavon, C. A. P. 1993, A&A, 275, 283

Stein, R. F. & Nordlund, A. 1998, ApJ, 499, 914

Stix, M. 2002, The sun: an introduction, ed. Stix, M.

Thomas, J. H., Weiss, N. O., Tobias, S. M., & Brummell, N. H. 2002, Nature, 420, 390

Tritschler, A., Schlichenmaier, R., Bellot Rubio, L. R., et al. 2004, A&A, 415, 717

van Noort, M., Rouppe van der Voort, L., & Löfdahl, M. G. 2005, Sol. Phys., 228, 191

van Noort, M. J. & Rouppe van der Voort, L. H. M. 2006, ApJ, 648, L67

Vecchio, A., Cauzzi, G., & Reardon, K. P. 2009, A&A, 494, 269

Vernazza, J. E., Avrett, E. H., & Loeser, R. 1981, ApJS, 45, 635

Wedemeyer-Böhm, S., Lagg, A., & Nordlund, Å. 2009, Space Sci. Rev., 144, 317

Wedemeyer-Böhm, S., Steiner, O., Bruls, J., & Rammacher, W. 2007, in Astronomical Society of the Pacific Conference Series, Vol. 368, The Physics of Chromospheric Plasmas, ed. P. Heinzel, I. Dorotovič, & R. J. Rutten, 93

Weiss, N. O., Thomas, J. H., Brummell, N. H., & Tobias, S. M. 2004, ApJ, 600, 1073

Westendorp Plaza, C., del Toro Iniesta, J. C., Ruiz Cobo, B., et al. 1997, Nature, 389, 47

Wilson, A. & Maskelyne, N. 1774, Royal Society of London Philosophical Transactions Series I, 64, 1

Paper I

Astronomy & Astrophysics manuscript no. 2010bisec˙cor˙thesis
November 7, 2010

Solar velocity references from 3D HD photospheric models

J. de la Cruz Rodríguez[1,2], D. Kiselman[1] and M. Carlsson[3,4]

[1] Institute for Solar Physics, Royal Swedish Academy of Sciences, AlbaNova University center, SE-106 91 Stockholm, Sweden
[2] Department of Astronomy, Stockholm University, AlbaNova University center, SE-106 91 Stockholm, Sweden
[3] Institute of Theoretical Astrophysics, University of Oslo, P.O. Box 1029 Blindern, N-0315 Oslo, Norway
[4] Center of Mathematics for Applications, University of Oslo, P.O. Box 1053 Blindern, N-0316 Oslo, Norway

Preprint online version: November 7, 2010

ABSTRACT

Context. The measurement of Doppler velocities in spectroscopic solar observations requires a reference for the local frame of rest. The rotation of the Earth, Sun-Earth radial velocity and the rotation of the Sun introduce velocity offsets in the observations. Normally, good references for velocities are missing (e.g. telluric lines), especially in filter-based spectropolarimetric observations.
Aims. We determine an absolute reference for line-of-sight velocities measured from solar observations for any heliocentric angle, calibrating the convective line shift of spatially-averaged profiles on quiet-sun from a 3D hydrodynamical simulation. This method works whenever there is quiet sun in the field-of-view, and it has the advantage of being relatively insensitive to uncertainties in the atomic data.
Methods. We carry out radiative transfer computations in LTE for selected C I and Fe I lines, whereas the Ca II infrared lines are synthesized in non-LTE. Radiative transfer calculations are done with a modified version of MULTI, using the snapshots of a non-magnetic 3D hydrodynamical simulation of the photosphere.
Results. The resulting synthetic profiles show the expected C-shaped bisector at disk center. The degree of asymmetry and the line shifts however, show a clear dependence on the heliocentric angle and the properties of the lines. The profiles at $\mu = 1$ are compared with observed profiles to prove their reliability and they are tested against errors induced by the LTE calculations, inaccuracies in the atomic data and the 3D simulation.
Conclusions. Theoretical quiet-sun profiles of lines commonly used by solar observers are provided to the community. Those can be used as absolute references for line-of-sight velocities. The limb effect is produced by the projection of the 3D atmosphere along the line of sight. Non-LTE effects on Fe I lines are found to have a small impact on the convective shifts of the lines, reinforcing the usability of the LTE approximation in this case. We estimate the precision of the disk-center line shifts to be approximately 50 m s^{-1}, but the off-center profiles remain to be tested against observations.

Key words. Convection – Sun: photosphere – Line: fomation – Radiative transfer – Sun: granulation – Hydrodynamics

1. Introduction

The need for high spatial and spectral resolution in solar observations stimulates new advances in telescope and instrumentation technology, adaptive optics and image reconstruction techniques. However, the accuracy of the measurements is often limited by calibration issues. This is evident when using Doppler shifts of spectral lines to acquire line-of-sight velocities in the solar plasma, where the task of finding a local standard of rest is often problematic.

The current work is partly motivated by the installation of the CRisp Imaging Spectropolarimeter (CRISP, Scharmer et al. 2008) at the Swedish 1-m Solar Telescope (SST, Scharmer et al. 2003). Instruments like this usually lack laboratory wavelength references, while the use of telluric lines has limitations as will be discussed below. The obvious (and commonly used) solution of letting the spectral line of interest – averaged over a sufficiently large area and sufficiently long time – define a local frame of rest is confounded by the fact that convective motions leave strong fingerprints on any spectral line formed in the solar photosphere. The statistical average of bright blueshifted and dark redshifted profiles formed in granules and intergranular lanes respectively, produces the blueshifted C-shaped bisectors of photospheric lines as reviewed by Dravins (1982).

Send offprint requests to: J.d.l.C.R.: e-mail: jaime@astro.su.se

Below, we discuss some methods that have been used to define a velocity reference for solar observations.

- *Sunspot umbrae* are not uncommon as standards (e.g., Beckers 1977; Scharmer et al. 2008; Ortiz et al. 2010) but this only works when a suitable sunspot is in the field-of-view and relies on the assumption that the umbra is at rest because of the convective motions being suppressed by the strong magnetic fields. Furthermore the line must be measurable in the umbra and wavelength shifts induced by blends from lines uniquely formed in the umbra (e.g. molecules), must be accounted for. Finally, observations of umbrae are always plagued by straylight from the much brighter quiet photosphere.
- *Telluric lines* can be used to define a laboratory-frame reference which can then be transformed to the Sun. Martinez Pillet et al. (1997) and Bellot Rubio et al. (2008) used telluric lines to derive the wavelength scale for their observations, then converted to an absolute wavelength scale on the Sun given the ephemeris constants, time of the observations, solar rotation and the laboratory wavelengths for all observed spectral lines.
- *A spectral atlas*, most commonly the atlas acquired with the Fourier Transform Spectrometer at the McMath-Pierce Telescope (hereafter called the FTS atlas) of Brault & Neckel (1987), can be used to calibrate observations. This was done

by Langangen et al. (2007) who used the laboratory wavelength to define the reference for velocities, assuming an absence of systematic errors in the FTS atlas itself and correcting for the gravitational redshift (633 m s^{-1}). This method only works at disk center where the atlas was recorded.

– *Numerical models* can be used to predict convective line shifts and thus provide a velocity reference. A two-component model of the solar photosphere was derived by Borrero & Bellot Rubio (2002) from the inversion of Fe I spectral lines. Since it does not contain any horizontal velocities its then in principle limited to calibrate disk center observations, for which it was used by Tritschler et al. (2004) and Franz & Schlichenmaier (2009). However, Bellot Rubio et al. (2004), used it together with the empirical results of Balthasar (1988) to estimate lineshifts also off solar center. Langangen et al. (2007) employed a 3D numerical granulation model to compute the convective blueshift of the C I 5380 Å line and calibrate their observations. The latter approach was necessary because the laboratory wavelength of the C I line is not known with enough precision to use the atlas calibration that is mentioned above.

We note that telluric lines are not always co-observable with the solar diagnostic lines and that when this is the case, observing them can be expensive. Observations with tunable filters require high cadence because of seeing variability and solar evolution. Any time spent recording telluric lines thus decreases the spatial resolution and the signal-to-noise of the science data. This would also apply to any laboratory spectral-line source used for calibration. Furthermore, approaches using telluric lines (or other calibration lines) and spectral atlases all require very accurate atomic data to define the zero velocity point and thus transform from wavelength to velocity. Such data are unfortunately not available for many of the lines that are extensively used in solar physics as is apparent in the work of Langangen et al. (2007) described above. Their approach is proposed in this study: the use of realistic 3D numerical simulations of the solar photosphere to compute spatially-averaged line profiles. As the radiative transfer computation is carried out in the local frame of rest of the Sun and the adopted atomic data is known, the velocity shifts of the spatially-averaged profile can be computed accurately for different heliocentric angles, relative to the assumed center of the line. This method relies on the degree of realism of the 3D simulation and requires a large statistical sample of spectra to compute the spatially-averaged profile.

The aim of this work is to provide the community with a set of theoretical spatially-averaged quiet-Sun profiles of lines commonly used in solar physics, that are computed for a range of heliocentric angles.

In Sect. 2 the atomic data and radiative transfer details are discussed. The 3D HD simulation is described in Sect. 3. In Sect. 4 the results are presented together with an error analysis and a real filter-based observation is calibrated using the new data. Section 5 describes the electronic data made available and Sect. 6 summarizes the main conclusions of this work.

2. Line list and radiative transfer

The calculations were carried out with a selection of lines (Table 1) that are extensively used in solar physics, including lines that can currently be observed with CRISP at the SST. A modified version of the radiative transfer code Multi (Carlsson 1986) was used to compute synthetic spectra from the simulation snapshots. The Fe I and C I lines were calculated assuming local thermodynamical equilibrium (LTE), which is a reasonable assumption for the wings of most photospheric Fe I lines (Gadun et al. 1999; Asplund et al. 2000). Fabbian et al. (2006) found that non-LTE effects for C I lines are expected to be small with the effect on derived abundance being < 0.05 dex. Possible errors produced by non-LTE effects will be further discussed in Section 4.3.1.

The Ca II lines were computed in 1.5D non-LTE – where the non-LTE problem is solved in 1D – using the same model atom as Leenaarts et al. (2009), which consists of 5 bound levels plus a continuum.

Table 1. Atomic data, sorted by element in increasing wavelength.

λ_0 (Å)	E_c	$\log gf$	σ	α	$\log \epsilon$
C I 5380.3370	7.6850	-1.824	1238	0.229	8.53
Fe I 5250.2089	0.1210	-4.938	207	0.253	7.44
Fe I 5250.6460	2.1980	-2.181	344	0.268	7.71
Fe I 5576.0888	3.4300	-1.000	854	0.232	7.69
Fe I 6082.7106	2.2230	-3.573	306	0.271	7.45
Fe I 6301.5012	3.6540	-0.718	834	0.243	7.55
Fe I 6302.4940	3.6860	-1.203	850	0.239	7.50
Fe I 7090.3835	4.2300	-1.210	934	0.248	7.63
Ca II 8498.0134	1.6920	-0.6391	291	0.275	6.31
Ca II 8542.0532	1.7000	-0.4629	291	0.275	6.31
Ca II 8662.1605	1.6920	-0.7231	291	0.275	6.31

Notes. σ is the cross-section in units of the Bohr radius and α is a dimensionless parameter used together with σ in the computation of collisional broadening (Barklem et al. 1998). The parameter $\log \epsilon$ represents the fitted value of the abundance for each line.

Atomic data were obtained from the VALD-2 database (Kupka et al. 2000). The treatment of van der Waals broadening follows that of Barklem et al. (1998) and the required cross sections were taken from Barklem et al. (2000), except for the C I line provided by Paul Barklem (private comunication). The effective quantum numbers $n*$ for this transition are $1.95 \rightarrow 3.27$. The treatment becomes less reliable when $n* > 3.0$ but it is more accurate than the commonly used Unsold (1955) formulation.

In order to achieve the best possible fit between the synthetic line profile at $\mu = 1$ and the FTS atlas, the elemental abundance is individually adjusted for each line. The resulting abundance values (last column in Table 1) should not be regarded as such. Rather, they act as free parameters that compensate for errors from atomic data, the LTE approximation, and the models themselves. The hope is that by fitting the profile the correct layer of the model with the appropriate velocity field is being sampled. Since non-LTE effects could be expected to affect the cores of strong lines, only the wings of each line were used for the fit of the abundance, however the results change marginally when the full profile is used to fit.

The results for the Ca II infrared triplet lines must be approached with extra caution since the lines are very strong and the 3D simulation does not extend all the way up to the chromosphere. Therefore the calculated core of the line cannot be compared to real observations, but the photospheric origin of the wings suggests the usability of the models with these lines, as discussed by Shine & Linsky (1974).

We have included blends affecting the Fe I and C I lines. The atomic parameters for these were taken from the VALD-2 database (Kupka et al. 2000). The blends are weak, but have a small effect on the upper part of some bisectors. The Ca II lines have some strong blends in the wings which greatly affect the bisectors, thus these blends were not present in the present Ca II calculations.

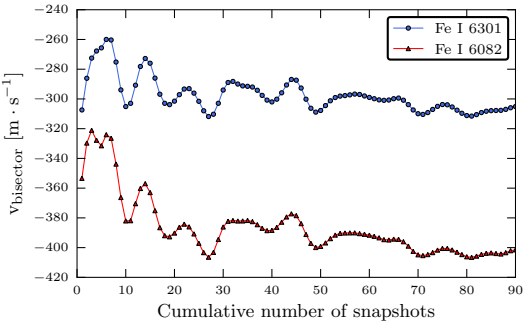

Fig. 1. Mean bisector velocity as a function of the number of snapshots used to compute the spatially-averaged spectrum.

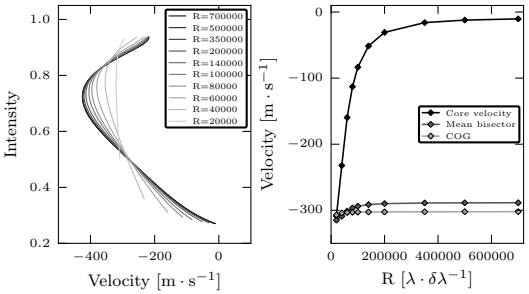

Fig. 3. *Left:* Bisectors of the synthetic Fe I 6301.5 Å line as a function of the spectral resolution. *Right:* Velocities measured in different ways from the profiles on the left panel, as a function of spectral resolution.

3. 3D hydrodynamical photospheric models

The 3D hydrodynamical simulation consists of 90 snapshots and covers around 45 minutes of solar time (Trampedach et al., in prep.; Pereira et al. 2009). The simulation does not include magnetic fields. The radiative energy transport was computed with an improved multi-group opacity binning of 12 bins, when compared with the 3D models of Asplund et al. (2000). The original simulation of $240 \times 240 \times 240$ grid-points covering a region of $6 \times 6 \times 4$ Mm was interpolated to a finer vertical depth grid in the radiative zone and sampled to a coarser grid in the horizontal plane for radiative transfer calculations. The resulting snapshots had a size of $50 \times 50 \times 82$ grid points representing a 6 Mm square. Our tests show that the effect of such a resampling in the horizontal plane has a negligible effect on the spatially-averaged profiles of the lines.

The presence of oscillations in the simulation broadens the time-averaged profile compared to the individual snapshots. The oscillations have a quasi-periodic behavior, so at least one period should be included in the time average in order to avoid systematic shifts of the average profiles. Figure 1 shows the average velocity (integrated along the bisector) of the time averaged profile as a function of the number of snapshots used in the time series. The limited sample of granules and intergranular lanes enclosed in a 6 Mm box reinforces the need to use more than one period in order to converge to a stable average for the line shift. Therefore, the whole time series was used for computing the average line profiles.

In order to produce profiles off disk center, the properties of the 3D snapshots are slanted assuming periodic boundary conditions and the velocity vector is projected into the new line-of-sight. The height scale is also modified to match the new geometry of the 3D model.

4. Results

In Fig. 2 the resulting line profiles for all heliocentric angles are plotted together along with their bisectors.

The C I 5380 Å line shows the strongest convective blueshift, an expected result given that it is a weak line and its very high sensitivity to temperature caused by its high excitation potential – both leading to the line being formed deep where vertical velocities are high and a very weak intergranular contribution. The blueshift decreases monotonously towards the limb.

A variety of bisector shapes and μ dependences are found in the Fe I lines. At $\mu = 1$, the lines have the expected blueshifted convective C-shaped bisectors. When going off center, the blueshift for many lines increases while at even higher heliocentric angles the blueshift decreases again, sometimes turning into a redshift, and the bisectors become more \-shaped. Each line shows its own individual behaviour – function of its strength, excitation potential, and other properties. The line cores have been excluded from the bisectors for the Ca II lines. These wing bisectors show a progression from a C-shape to a \-shape from center to limb.

Table 2 lists numerical values for the convective shifts computed as the mean of the bisector – excluding the part closest to the continuum – for each line and μ value, and Table 3 lists the line core velocities found when convolving the synthetic line profiles with the appropriate CRISP instrumental profile.

4.1. Effect of spectral resolution

The asymmetry of the lines will decrease with decreased spectral resolution. When comparing with observations, or using the theoretical profiles for velocity calibration, the profiles must be convolved to the proper spectral resolution. Figure 3 illustrates the dependence of the mean bisector, the center-of-gravity (COG) velocity, and the line-core velocity on spectral resolution. The core velocity is naturally the one most sensitive to spectral resolution. COG is least sensitive in this specific case, but the deviations in all cases start at such spectral resolutions that we are content to use the mean bisector velocity in all our illustrations here. We do think that any practical use of our line profiles should use the detailed profile with the application of the appropriate instrumental smearing and weighting.

4.2. The limb effect

The bisectors change with heliocentric angle, and close to the limb the blueshift usually gets small and is sometimes turned into a redshift for the line cores. This limb effect (Adam et al. 1976; Beckers & Nelson 1978; Balthasar 1985) was subject to much speculation before granulation was understood (see Dravins 1982). It seems that a comprehensive explanation is still lacking, which could be due to the fact that the complicated nature of the situation precludes simple explanations. Nevertheless, we want to discuss it here in the light of our results.

The convective blueshift and line asymmetry at disk center are caused by the asymmetry of large bright granules with a relatively slow upward flow producing blueshifted lines and nar-

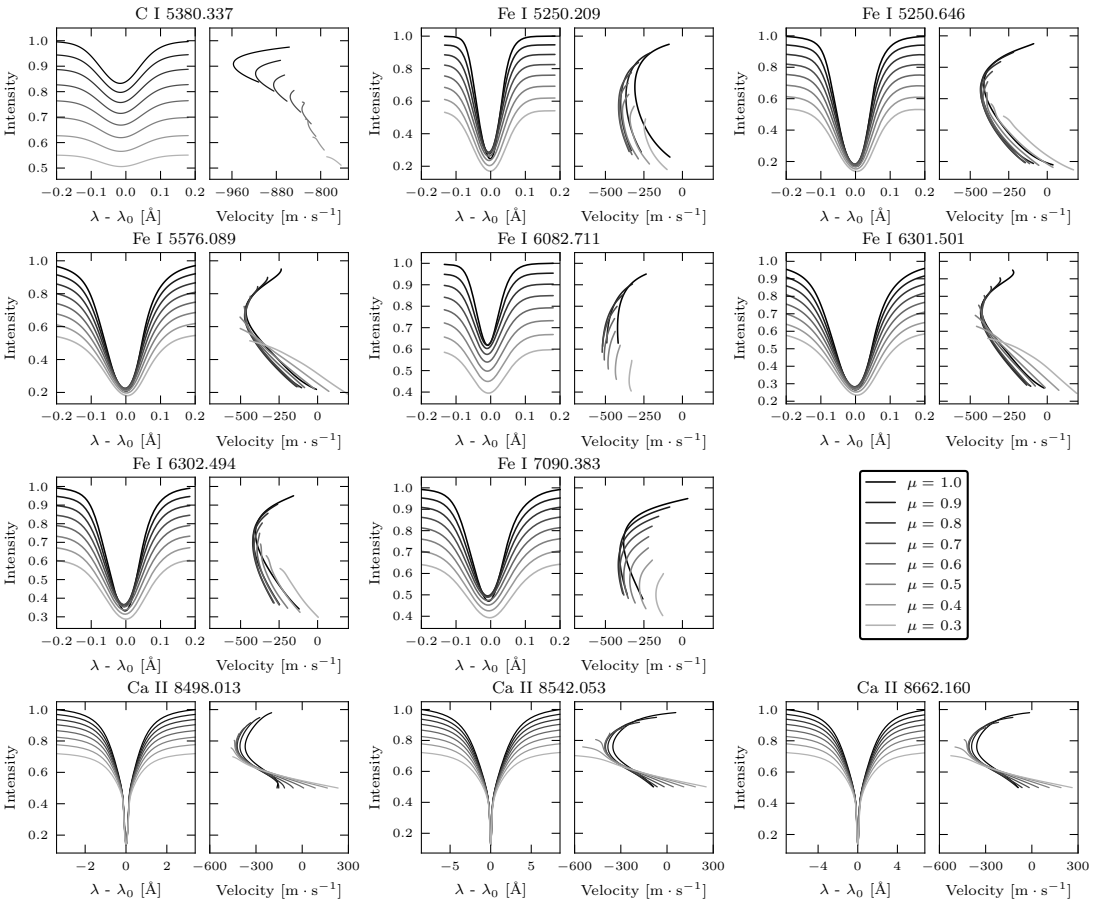

Fig. 2. Synthetic profiles and the corresponding bisectors resulting from the calculations of C I, Fe I and Ca II lines. The grey scale indicates the variation of the heliocentric angle from $\mu = 1.0$ to $\mu = 0.3$. Note that the bisectors for the Ca II lines are not shown in the core part.

row dark intergranular lanes with fast downward flows producing redshifted lines. As we leave the disk center a number of effects will change the shifts and the line profiles. Towards the limb, higher photospheric layers are sampled that have different velocity patterns and different statistical relations between intensity and line-of-sight velocities. Of particular interest is the pattern of inverse granulation (e.g., Cheung et al. 2007) that characterises the photospheric structure above a certain height. Also, horizontal velocities become more important as the viewing angle decreases and will soon dominate over the contribution from vertical convective motions. There are also 3D effects due to the corrugated nature of the optical depth surface. We can consider the following mechanisms that can decrease the blueshift and ultimately lead to a redshift in the average line profiles:

1. The intensity-velocity correlation changes as higher and higher levels in the photosphere are sampled by the line (e.g. Janssen & Cauzzi 2006; Cheung et al. 2007). This is the same effect that causes the C-shape in disk-center bisectors.
2. The redshifted part of the granule is seen against a brighter background than the blue-shifted part (Beckers & Nelson 1978; Asplund et al. 2000).
3. Near the limb, surface corrugation causes redshifted parts of granules to show larger areas to the observer (Balthasar 1985).
4. Reversed granulation "hills" over intergranular lanes shield blueshifted parts of granules when observed off disk center.

Figure 4 shows a cross section through a simulation snapshot illustrating line formation at $\mu = 0.3$. Inspection of the simulation snapshots in this way can give support to all the listed mechanisms and also give inspiration to the invention of new ones. The effect of the hot wall over an intergranular lane (at $x \sim 2200$ km) is for example obvious. It blocks the view towards the blueshifted side of a granule. But a similar structure is also present over the center of a granule ($x \sim 4000$ km), seemingly blocking a redshifted side of a granule. One can thus argue that some of the mentioned mechanisms and others can produce a *blueshift* with decreasing μ. Deciding which mechanisms will

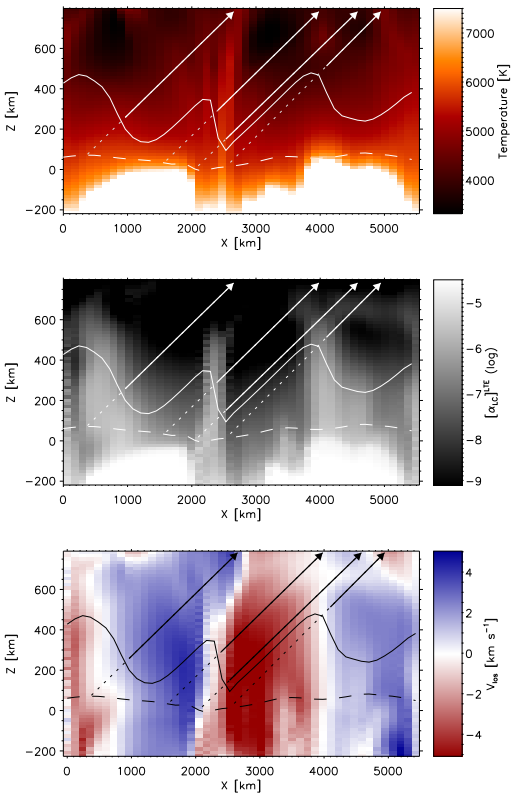

Fig. 4. Properties of the model along a slice of one of the snapshots at $\mu = 0.3$: temperature, absorption coefficient at the core of Fe I 6301.5 Å and line of sight velocity from top to bottom. The solid line that is overplotted over the three panels represents the layer where $\tau_{LC} = 1$ along the line of sight. Four rays are shown as solid lines above $\tau_{LC} = 1$ and dashed below this height. The bottom panel shows the line-of-sight velocities along the direction shown by the rays. The horizontal dashed line represents the layer where τ_{500} equals 1 at $\mu = 0.3$.

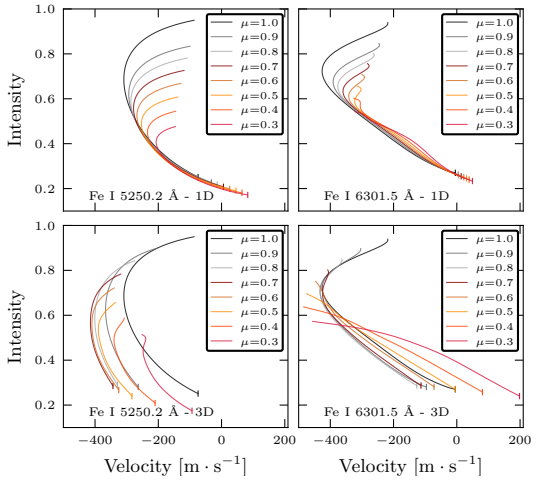

Fig. 5. Bisectors for two lines computed in the plane-parallel treatment, "1D", compared to the full "3D" result.

dominate requires a quantitative analysis. We have made a first effort in that direction.

Effects 2, 3, and 4 are true 3D effects that break the symmetry between redshifted limbside granular parts and blueshifted centerside parts. They should go away in a multi-1D treatment where each column in the simulation is treated as a plane-parallel atmosphere. The results of such a numerical experiments for two of our lines can be seen in Fig. 5. It is clear that for each line, the variation of bisectors with μ is smaller than in 3D. It is also monotonous and always in the sense that a profile becomes redder at the core of the line with decreasing μ. The close following of the successive bisectors to that of $\mu = 1$ is an illustration of the Eddington-Barbier relations: the μ dependence is equivalent to the depth dependence. We take this to mean that much of the center-to-limb variation of spectral line shifts is due to 3D effects. The latter either redshift or blueshift the bisectors relative to the 1D case. For example, the blueshift relative to disk center that is seen in many lines for moderate heliocentric angles must be due to a 3D mechanism. We hypothesise that this is due to the screening of narrow downdrafts from view as the line of sight departs from the vertical.

4.3. Error analysis

4.3.1. non-LTE effects in Fe I lines

Our radiative transfer calculations assume LTE. The errors introduced by this approximation will to some extent be reduced by fitting the line profiles using an individual abundance value for each line as a free parameter. Shchukina & Trujillo Bueno (2001) studied the impact of non-LTE effects on Fe I and Fe II lines using a 3D simulation (but a 1D treatment of the non-LTE problem, thus 1.5D) and reported larger departures from LTE in granules than in intergranular lanes. Based on this work, we can expect the following two non-LTE mechanisms to dominate:

1. *Overionization*: A line from a neutral species typically has lower line opacity than its LTE value because of overionization that is caused by the UV radiation field being stronger than the local Planck function. This causes the line to be formed deeper in the atmosphere and thus be weaker than in LTE.
2. The non-LTE line source function S_ν^l can be expressed in terms of the departure coefficients of the populations from the upper (b_j) and lower (b_i) levels (see Rutten 2003) if stimulated emission is neglected,

$$S_\nu^l \sim \frac{b_j}{b_i} B_\nu(T) \tag{1}$$

where $B_\nu(T)$ is the Planck function. *Photon losses* in the line itself lead to a decrease of b_j and increase of b_i, producing a line source function that is lower than the Planck function. This leads to a stronger line than in LTE.

The first effect tends to be the most important for weak lines, while the second is found for strong lines because the line opacity dominates over the background opacity. In some cases, the non-LTE and LTE profiles are very similar because the two effects cancel out. However, the presence of larger LTE departures

Table 2. Convective shifts in m s^{-1} of the studied lines from $\mu = 1.0$ to $\mu = 0.3$.

Element	λ_0 (Å)	$\mu = 1.0$	$\mu = 0.9$	$\mu = 0.8$	$\mu = 0.7$	$\mu = 0.6$	$\mu = 0.5$	$\mu = 0.4$	$\mu = 0.3$
C I	5380.34	-948	-936	-922	-910	-897	-888	-880	-844
Fe I	5250.21	-294	-372	-410	-426	-420	-394	-346	-259
Fe I	5250.65	-304	-354	-370	-369	-348	-308	-245	-140
Fe I	5576.09	-334	-378	-388	-383	-360	-317	-249	-140
Fe I	6082.71	-441	-495	-522	-536	-531	-511	-473	-397
Fe I	6301.50	-307	-349	-358	-351	-325	-279	-211	-101
Fe I	6302.49	-335	-387	-404	-403	-381	-342	-280	-176
Fe I	7090.38	-352	-396	-409	-407	-389	-354	-302	-210
Ca II	8498.01	-265	-288	-289	-275	-248	-206	-148	-70
Ca II	8542.05	-335	-364	-374	-372	-359	-337	-307	-269
Ca II	8662.16	-272	-294	-293	-279	-251	-208	-149	-68

Notes. The bisector of each line was integrated from 95% of the continuum intensity to the core of the line. In the case of the Ca II lines, the non-LTE core was excluded. In the case of C I the upper threshold was higher (97%) because the line is weak.

Table 3. Line core velocities of the synthetic spectral lines (excluding Ca II) convolved with the appropriate theoretical profile of CRISP for each wavelength.

Element	λ_0 (Å)	$\mu = 1.0$	$\mu = 0.9$	$\mu = 0.8$	$\mu = 0.7$	$\mu = 0.6$	$\mu = 0.5$	$\mu = 0.4$	$\mu = 0.3$
C I	5380.34	-928	-895	-867	-840	-820	-810	-795	-764
Fe I	5250.21	-178	-306	-358	-370	-354	-315	-246	-134
Fe I	5250.65	-115	-196	-221	-213	-177	-115	-26	108
Fe I	5576.09	-163	-222	-231	-209	-164	-96	-3	126
Fe I	6082.71	-403	-470	-499	-508	-500	-480	-433	-341
Fe I	6301.50	-188	-238	-241	-217	-173	-109	-17	108
Fe I	6302.49	-255	-326	-347	-338	-306	-255	-178	-57
Fe I	7090.38	-315	-378	-396	-388	-362	-321	-255	-148

in the granules than in the intergranular lanes, not only changes the strength of the line, but also the convective line shift. We tested the sensitivity of the resulting line shift to such differential departures from LTE. One of the 3D snapshots was divided in granules and intergranular lanes based on the sign of the vertical velocities at $\tau_{500} = 1$ and synthetic spectra were computed for different values of the iron abundance. The aim was to find the combinations of abundances in granules and intergranules that reproduce a spatially-averaged spectrum with the same equivalent width as the observed profile. We used a non-linear least-squares fit, described in Markwardt (2009), in order to infer these pairs of values. Figure 6 illustrates the average shift of the line as a function of abundance difference between the granules and the intergranular lanes. The reference was set where the abundance derived from the granules and intergranules is the same. Shchukina & Trujillo Bueno (2001) found an average non-LTE effect on derived Fe abundances of 0.1 dex. If this number is taken as typical also of the difference between granules and intergranules abundance in Fig. 6, the errors in the computed lineshift due to non-LTE effects should be smaller than ±30 m s^{-1}.

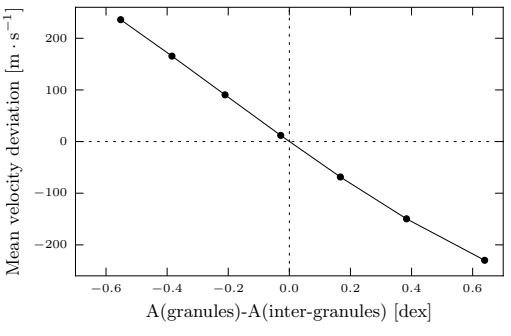

Fig. 6. Differential Doppler shift of the Fe I 6082.7 Å line produced by changes in the relative abundance between granules and inter-granules. The combinations of granular/intergranular abundances were fitted to reproduce the equivalenth width of the FTS atlas.

4.3.2. Profile fitting

Due to the effects described in Section 4.3.1 and the fact that the 3D models are only realistic up to a certain height, the resulting profiles show differences compared to the FTS atlas. The solar abundances inferred by Asplund et al. (2005) normally lead to different results for the different lines, some presenting more damped wings than the atlas and others narrower. The abundance is used as a free parameter in order to match the wings of the synthetic profiles for $\mu = 1$ with the FTS atlas. The inner core is not included in the fitting procedure because generally non-LTE effects are expected to be larger there (see Rutten & Kostik 1982), and the model snapshots become less reliable close to the upper boundary (see Asplund et al. 2000).

As an indicator of the errors due to this fitting procedure, we performed test calculations to get the sensitivity of the bisectors to changes in the assumed abundance. The results are shown in Fig. 7. The left panels correspond to the Fe I 6301 Å line, calculated on three different heliocentric angles, for different values of the Fe abundance. The panels on the right correspond to the C I 5380 Å, where the abundance covers an unrealistic range of values [8.19, 8.69]. This weak line, which is formed very close to the continuum, is more sensitive to changes in the abundance than the stronger Fe I line. The lower panels show the relative velocity shift integrated over the whole bisector. We estimate that

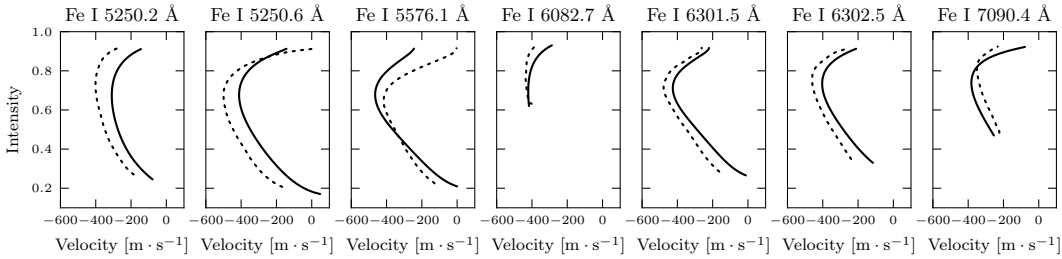

Fig. 8. Fe I synthetic bisectors (fulldrawn) compared with bisectors measured from the FTS atlas (dashed).

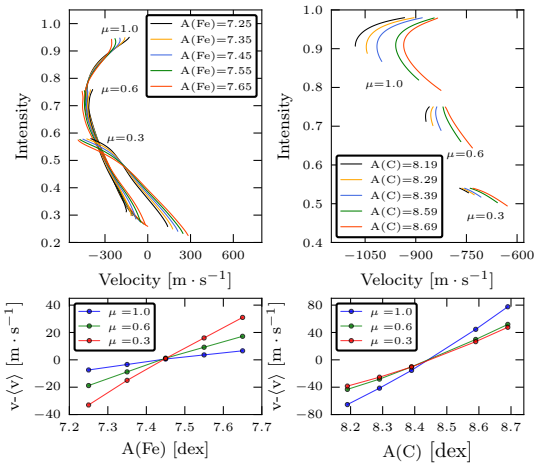

Fig. 7. Bisectors calculated for at $\mu = 1.0, 0.6, 0.3$ for a range of abundances. The results are from five snapshots only which means that they cannot be directly compared with, e.g., Fig 2. *Left:* abundance test for Fe I 6301 Å with values of the Fe abundance within [7.25-7.65] . *Right:* test for C I 5380 Å, the values of the abundance span an unrealistic range compared to the nominal value [8.19-8.69].

the uncertainties from the fitting procedure are within 0.1 dex in abundance which then corresponds to ±10 m s^{-1} for the integrated bisector.

4.3.3. Discussion

From the tests above, the estimated error in the shift of the lines is less than 50 m s^{-1}. This means that a full non-LTE treatment combined with the exact atomic data should not change these results by more than this amount. The estimate does not, however, include the intrinsic errors of the simulation.

To check the realism of the simulations we compare the synthetic line profiles at $\mu = 1.0$ with the FTS atlas after applying a gravitational redshift on the former. The average synthetic C I bisector lies 530 m s^{-1} redwards of that measured from the FTS atlas, something that we deem mostly to be due to error in the laboratory wavelength of the line. At face value our simulations implies a wavelength of 5380.3275 Å on the FTS-atlas wavelength scale. This is within the cited uncertainty (0.02 Å) of the laboratory value of 5380.3370 Å from Johansson (1966) which was used here. It is also comfortingly close to the 5380.3262 Å found in a similar way by Langangen et al. (2007) from their observations and simulations of magnetic regions. The bisectors for the Fe I lines are displayed in Fig. 8. The synthetic bisector shapes show an acceptable correspondence with those measured from the FTS atlas. The standard deviation of the differences in mean velocity is 56 m s^{-1} which corresponds to approximately 1 mÅ. This is comparable to our estimate of the internal errors from non-LTE effects and fitting procedures, but once again there is strong reason to believe that a significant part of these deviations are due to errors in the adopted laboratory wavelengths.

Finally we note that Allende Prieto & Garcia Lopez (1998) estimate the precision in FTS wavelengths to be on the order of 50 m s^{-1}. It seems likely that several of the error estimates discussed above are too conservative, but the synthetic profiles seem to pass the test and they should be correct within 50 m s^{-1}. Observational checks of the off-center profiles are more difficult but would be welcome. Since photospheric modelling often becomes more uncertain for small μ values it is natural to suspect that the accuracy of our convective line shifts will decrease towards the limb.

Note that the hydrodynamic granulation simulations do not include magnetic fields. This is potentially the most important source of errors in the practical application of these synthetic line profiles for velocity calibrations. For example, Langangen et al. (2007) estimated a difference of 200 m s^{-1} in convective shift for the C I 5380 Å line between non-magnetic and active granulation. (This was mostly caused by the changing intensity and velocity pattern and not by Zeeman splitting.) So any calibration work must use the least magnetic photospheric region available. However, how strong the quiet Sun magnetic fields are, is still an ongoing debate (e.g. Martínez González et al. 2008; Pietarila Graham et al. 2009; de Wijn et al. 2009).

4.4. Calibration of SST/CRISP observations

A quiet Sun dataset acquired with SST/CRISP at $\mu = 1.0$ was calibrated using the current results. The Fe I 6302 Å line was sampled with eight wavelength points, evenly distributed with a separation of $\mathrm{d}\lambda = 48$ mÅ and processed using the image restoration code MOMFBD (van Noort et al. 2005). The telecentric optical design of CRISP (Scharmer 2006) is optimum for high image quality, but it introduces instrumental field-dependent wavelength shifts produced by irregularities on the surface of the etalons, which are commonly known as cavity errors. The latter complicate the task of obtaining the spatially-averaged spectrum, as the profile is effectively broadened by

these random pixel-to-pixel shifts. The average spectrum was computed with a least-squares-fit of all the data points to a spline which was characterized with ten parameters. For this purpose, all the individual spectra were corrected for cavity errors and then arranged in a large array, which was sorted in increasing wavelength.

In order to carry out the velocity calibration, the synthetic spectrum obtained from the 3D simulation was convolved with the theoretical instrumental profile of CRISP, which included the effects of the beam converging at f/165. The velocity calibration was determined by finding the constant wavelength shift to the observed bisector that minimised the difference to the synthetic one. Figure 9 illustrates the results of the calibration, where Doppler map at the core of the line, is scaled between ± 1500 m s^{-1}. The bottom-left panel contains a density map of the spatially resolved spectra, corrected for cavity errors. The dispersion of points around the seven nominal wavelengths appears after correcting for the cavity errors in combination with the granulation contrast. The bisector of our calibrated data is over-plotted to the bisector of the synthetic spectrum that was convolved with the instrumental profile of CRISP. There is a telluric blend on the red wing of the observed profile, not present in the synthetic spectrum, that pollutes the upper part of the bisector.

5. Usage of electronic data

The synthetic profiles that have been presented in this study can be downloaded from `http://dubshen.astro.su.se/~jaime/line_shifts.tar.bz2` *(temporary)*. The spectral response of any instrument produces broadening and can introduce asymmetries in the observed profiles. Thus it is *imperative* that the profiles be degraded with the proper instrumental response before they are used to calibrate observations.
The quiet Sun average spectrum can be computed from quiet regions in the observations. However, the presence of p-modes (oscillations) will produce an unrealistic shift in the observed average profile. Thus, it should be averaged in time and space, or at least from a sufficiently large sample of quiet Sun spectra.

We have been cautious in the treatment of line cores, but the comparison with the FTS atlas suggests that the errors in the cores are small. Except for the Ca II IR triplet, we do not recommend against including the cores in velocity calibrations. We think, however, that a velocity measure that weigh in more of the profile will give a more reliable result.

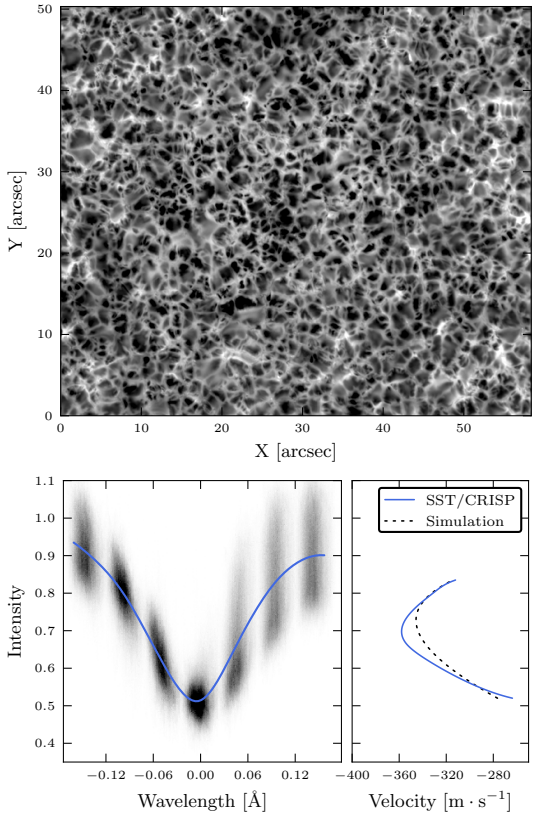

Fig. 9. *Top:* Doppler map of quiet-sun granulation observed with SST/CRISP at Fe I 6302 Å. The image grey scale is clipped to ± 1500 m s^{-1}. *Bottom-left:* Spatially-averaged profile computed along the image shown in the top panel. The density map represents the spatially-resolved profiles corrected for instrumental cavity errors. The average profile was computed using a least squares fit of all the points to a spline, consisting of 10 parameters. *Bottom-right:* Bisector of the observed spatially-averaged profile. The velocity calibration was carried out using our synthetic profile convolved with the CRISP instrumental profile.

6. Conclusions

We make use of the approach described by (Langangen et al. 2007) to obtain an absolute reference for velocities in solar observations. For this purpose, we have calibrated the shift of synthetic spectra produced by convective motions at different heliocentric angles for C I, Fe I and Ca II lines commonly used for solar physics diagnostics. We propose to use the profiles as absolute local references for line-of-sight velocities to allow accurate velocity measurements.

A realistic 3D hydrodynamical simulation of the the non-magnetic solar photosphere was used to synthesize the spectra. The computations were done in LTE for C I and Fe I lines whereas non-LTE computations were carried out in the Ca II infra-red lines. As the conversion from wavelength to velocity scale is done using the same laboratory wavelength that is used for computing the profiles, the measured line shifts are relatively unaffected by errors in the central wavelength. Uncertainties in the rest of atomic parameters are partially compensated when the profiles are fitted to reproduce the strength of the FTS atlas.

Our results show a systematic center-to-limb variation of the bisectors which is determined to a large extent by the 3D structure of the atmosphere which is projected along the line-of-sight. However, there is a small amount of redshift (relative to $\mu = 1.0$) produced by the change of the formation height with the heliocentric angle (non-3D effects), which is not related to projection effects. A careful analysis of the models suggests that a large number of 3D snapshots must be used in studies of line shifts so the oscillations are properly sampled and the statistics of granules and intergranules are complete, whereas non-LTE effects seem to have a minor influence on the shift of our Fe I lines. The largest uncertainty is related to the non-magnetic nature of the simulation. Nevertheless, we estimate our calibrations to be ac-

curate up to ~ 50 m s^{-1} at $\mu = 1$, remaining untested towards the solar limb.

We would like to emphasize the somewhat limited usability of the Ca II calibration, as observations are polluted by a significant number of blends, which should be masked in order to compare with the calibration data.

Our synthetic profiles reproduce spatially-averaged solar observations accurately, but it would be interesting to test for the impact of magnetic fields on the convective shift of the lines, and confirm the reliability of our calculations near the limb.

Acknowledgements. We thank Tiago Pereira for providing the 3D snapshots of the HD simulation and Roald Schnerr and Michiel van Noort for providing reduced data from the SST/CRISP. We are most grateful to Paul Barklem for providing unpublished cross-sections for collisional broadening. This research project has been supported by a Marie Curie Early Stage Research Training Fellowship of the European Community's Sixth Framework Programme under contract number MEST-CT-2005-020395: The USO-SP International School for Solar Physics. The Swedish 1-m Solar Telescope is operated on the island of La Palma by the Institute for Solar Physics of the Royal Swedish Academy of Sciences in the Spanish Observatorio del Roque de los Muchachos of the Instituto de Astrofísica de Canarias.

References

Adam, M. G., Ibbetson, P. A., & Petford, A. D. 1976, MNRAS, 177, 687
Allende Prieto, C. & Garcia Lopez, R. J. 1998, A&AS, 131, 431
Asplund, M., Grevesse, N., & Sauval, A. J. 2005, in Astronomical Society of the Pacific Conference Series, Vol. 336, Cosmic Abundances as Records of Stellar Evolution and Nucleosynthesis, ed. T. G. Barnes III & F. N. Bash, 25–+
Asplund, M., Nordlund, Å., Trampedach, R., Allende Prieto, C., & Stein, R. F. 2000, A&A, 359, 729
Balthasar, H. 1985, Sol. Phys., 99, 31
Balthasar, H. 1988, A&AS, 72, 473
Barklem, P. S., Anstee, S. D., & O'Mara, B. J. 1998, Publications of the Astronomical Society of Australia, 15, 336
Barklem, P. S., Piskunov, N., & O'Mara, B. J. 2000, VizieR Online Data Catalog, 414, 20467
Beckers, J. M. 1977, ApJ, 213, 900
Beckers, J. M. & Nelson, G. D. 1978, Sol. Phys., 58, 243
Bellot Rubio, L. R., Balthasar, H., & Collados, M. 2004, A&A, 427, 319
Bellot Rubio, L. R., Tritschler, A., & Martínez Pillet, V. 2008, ApJ, 676, 698
Borrero, J. M. & Bellot Rubio, L. R. 2002, A&A, 385, 1056
Brault, J. W. & Neckel, H. 1987, Spectral Atlas of Solar Absolute Disk-averaged and Disk-Center Intensity from 3290 to 12510 Å, ftp://ftp.hs.uni-hamburg.de/pub/outgolng/FTS-Atlas
Carlsson, M. 1986, Uppsala Astronomical Observatory Reports, 33
Cheung, M. C. M., Schüssler, M., & Moreno-Insertis, F. 2007, A&A, 461, 1163
de Wijn, A. G., Stenflo, J. O., Solanki, S. K., & Tsuneta, S. 2009, Space Sci. Rev., 144, 275
Dravins, D. 1982, ARA&A, 20, 61
Fabbian, D., Asplund, M., Carlsson, M., & Kiselman, D. 2006, A&A, 458, 899
Franz, M. & Schlichenmaier, R. 2009, A&A, 508, 1453
Gadun, A. S., Solanki, S. K., & Johannesson, A. 1999, A&A, 350, 1018
Janssen, K. & Cauzzi, G. 2006, in Astronomical Society of the Pacific Conference Series, Vol. 354, Solar MHD Theory and Observations: A High Spatial Resolution Perspective, ed. J. Leibacher, R. F. Stein, & H. Uitenbroek, 49–+
Johansson, L. 1966, Ark. Fys., 31, 201
Kupka, F. G., Ryabchikova, T. A., Piskunov, N. E., Stempels, H. C., & Weiss, W. W. 2000, Baltic Astronomy, 9, 590
Langangen, Ø., Carlsson, M., Rouppe van der Voort, L., & Stein, R. F. 2007, ApJ, 655, 615
Leenaarts, J., Carlsson, M., Hansteen, V., & Rouppe van der Voort, L. 2009, ApJ, 694, L128
Markwardt, C. B. 2009, in Astronomical Society of the Pacific Conference Series, Vol. 411, Astronomical Society of the Pacific Conference Series, ed. D. A. Bohlender, D. Durand, & P. Dowler, 251–+
Martínez González, M. J., Collados, M., Ruiz Cobo, B., & Beck, C. 2008, A&A, 477, 953
Martinez Pillet, V., Lites, B. W., & Skumanich, A. 1997, ApJ, 474, 810
Ortiz, A., Bellot Rubio, L. R., & Rouppe van der Voort, L. 2010, ApJ, 713, 1282
Pereira, T. M. D., Kiselman, D., & Asplund, M. 2009, A&A, 507, 417
Pietarila Graham, J., Danilovic, S., & Schüssler, M. 2009, ApJ, 693, 1728
Rutten, R. J. 2003, Radiative transfer in stellar atmospheres, ed. Utrecht University lecture notes, 8th edition
Rutten, R. J. & Kostik, R. I. 1982, A&A, 115, 104
Scharmer, G. B. 2006, A&A, 447, 1111
Scharmer, G. B., Bjelksjo, K., Korhonen, T. K., Lindberg, B., & Petterson, B. 2003, in Society of Photo-Optical Instrumentation Engineers (SPIE) Conference Series, Vol. 4853, Society of Photo-Optical Instrumentation Engineers (SPIE) Conference Series, ed. S. L. Keil & S. V. Avakyan, 341–350
Scharmer, G. B., Narayan, G., Hillberg, T., et al. 2008, ApJ, 689, L69
Shchukina, N. & Trujillo Bueno, J. 2001, ApJ, 550, 970
Shine, R. A. & Linsky, J. L. 1974, Sol. Phys., 37, 145
Tritschler, A., Schlichenmaier, R., Bellot Rubio, L. R., et al. 2004, A&A, 415, 717
Unsold, A. 1955, Physik der Sternatmospharen, MIT besonderer Berucksichtigung der Sonne., ed. Unsold, A.
van Noort, M., Rouppe van der Voort, L., & Löfdahl, M. G. 2005, Sol. Phys., 228, 191

Paper II

Astronomy & Astrophysics manuscript no. 3dchromos3
October 27, 2010

Non-LTE inversions from a 3D MHD chromospheric model

J. de la Cruz Rodríguez[1,2], H. Socas-Navarro[3], M. Carlsson[4,5] and J. Leenaarts[6]

[1] Institute for Solar Physics of the Royal Swedish Academy of Sciences, AlbaNova, SE-106 91 Stockholm, Sweden
[2] Stockholm Observatory, AlbaNova University Center, SE-106 91 Stockholm, Sweden
[3] Instituto de Astrofísica de Canarias, Avda Vía Láctea S/N, La Laguna 38205, Tenerife, Spain
[4] Institute of Theoretical Astrophysics, University of Oslo, P.O. Box 1029 Blindern, N-0315 Oslo, Norway
[5] Center of Mathematics for Applications, University of Oslo, P.O. Box 1053 Blindern, N-0316 Oslo, Norway
[6] Sterrekundig Instituut, Utrecht University, P.O. Box 80000 NL–3508 TA Utrecht, The Netherlands

Preprint online version: October 27, 2010

ABSTRACT

Context. The complex chromospheric landscape is believed to be governed by magnetic fields, even in quiet regions. Observers strive to develop tools that help to measure and interpret physical quantities, especially magnetic fields. During the past decade inversion methods have emerged as powerful tools to analyse active regions. However, their applicability in *weak* magnetic field regimes is still an ongoing debate.
Aims. This study aims to establish the diagnostic capabilities of NLTE inversion techniques applied to the Ca II infrared triplet, using a 3D MHD simulation of *quiet* Sun. We also comment on the instrumental requirements for observing polarization signals in the quiet Sun chromosphere.
Methods. A snapshot from a 3D MHD simulation of the solar atmosphere is used to compute synthetic Stokes profiles in the Ca II 8542 Å line. In order to compute the populations of the levels of the atom in NLTE, the 3D radiation field is evaluated using the 3D radiative transfer code MULTI3D. These synthetic observations are then inverted using the inversion code NICOLE, assuming plane parallel geometry. Spectral degradation and additive Gaussian noise are introduced in order to carry out the inversion in realistic conditions.
Results. Our NLTE inversions applied to *quiet* Sun synthetic observations provide good estimates of the chromospheric magnetic field, line-of-sight velocities and less accurate estimates of the temperature. The latter seems to be mostly affected by 3D NLTE effects, combined with the other effects further discussed in the present work. Along the same lines, the instrumental requirements to be able to observe chromospheric magnetic fields suggest that current observational strategies and instrumentation cannot successfully detect Stokes *linear* polarization with enough spectral coverage to allow for an inversion.

Key words. Sun: chromosphere – Radiative transfer – Sun: magnetic topology – Polarization

1. Introduction

The magnetic topology of the solar chromosphere is an outstanding challenge for observers. The limited polarimetric response of chromospheric spectral lines is usually combined with complicated modelling requirements (Socas-Navarro & Trujillo Bueno 1997; Pietarila et al. 2006; Manso Sainz & Trujillo Bueno 2010).

The development of inversion techniques have improved our capabilities to infer physical quantities from the chromosphere (e.g., Lagg et al. 2004; Asensio Ramos et al. 2008). The first full Stokes NLTE inversions of the Ca II infrared lines were carried out by Socas-Navarro et al. (2000). Their approach is optimal for active regions with strong Zeeman induced signals, however *quiet* Sun observations require very high sensitivity to detect polarization, especially in Stokes Q and U.

This study extends the work presented in Leenaarts et al. (2009) aiming to improve our understanding of the following aspects of chromospheric diagnostics.

1. Non-LTE inversions of quiet Sun observations: reliability and requirements using the Ca II 8542 Å line.
2. Detectability of Zeeman induced polarization: instrumental limitations and requirements.

The goal is to investigate polarimetric properties of Ca II infrared (IR) lines and the regime in which inversions yield a realistic result. A 3D simulation is used to compute synthetic full Stokes profiles with a realistic 3D solution of the NLTE problem. The resulting synthetic profiles are inverted assuming plane-parallel geometry on a pixel by pixel basis. Realistic values of noise and instrumental degradation are applied to the simulated observations before carrying out the inversions. In real observations, Stokes Q and U are produced by the combined action of scattering polarization and transverse Zeeman effect when $10\ \mathrm{G} < B < 100\ \mathrm{G}$ (Manso Sainz & Trujillo Bueno 2010). We emphasize that this study only accounts for Zeeman induced polarization, a simplification that is needed given the computational demands of the problem.

The simulated observations along with the 3D simulation and radiative transfer calculations are explained in Sect. 2. The inversion code and the inversion results are discussed in Sect. 3. The conclusions are summarized in Sect. 4.

2. Simulated observations

2.1. 3D MHD model

We make use of a snapshot from a 3D simulation of a patch of quiet Sun that extends from the upper convection zone to the

Send offprint requests to: J.d.l.C.R.: e-mail: jaime@astro.su.se

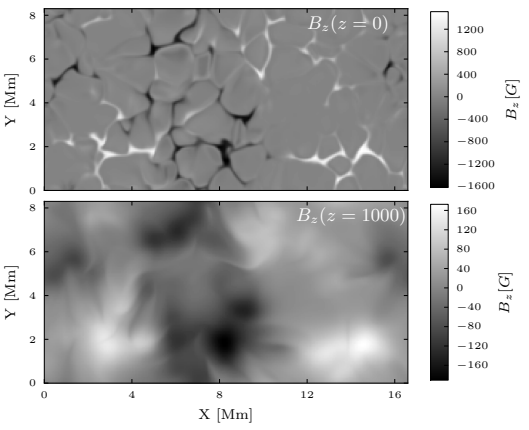

Fig. 1. B_z slices from the 3D snapshot at $z = 0$ km (top) and $z = 1000$ km (bottom).

corona. The simulation was carried out with the Oslo Stagger Code (OSC) (Hansteen et al. 2007) which includes non-gray radiative losses using multi-group opacities with scattering, NLTE radiative losses in the chromosphere, optically thin radiative losses in the corona, thermal conduction along the field lines using operator splitting and a multi-group method. The simulation domain consists of a grid of $256 \times 128 \times 160$ points covering a physical range of $16.6 \times 8.3 \times 15.5$ Mm, extending from the upper convection zone to the lower corona (from 1.5 Mm below to 14 Mm above average optical depth unity at 500 nm). The simulation snapshot is the same as that used by Leenaarts et al. (2009). The simulation has an average magnetic field strength of 150 G. Magnetic field is mostly concentrated in intergranular lanes at photospheric heights, whereas in the chromosphere it tends to fill up more space. Fig. 1 illustrates the vertical component of $\boldsymbol{B}$ in the photosphere (top) and in the low chromosphere (bottom).

2.2. Radiative transfer and inversions

We use the Non-LTE Inversion Code based on the Lorien Engine (Nicole, Socas-Navarro et al. 2010). Nicole includes a radiative transfer code for solving LTE and NLTE problems.

Our synthetic full Stokes profiles are computed in two steps. First, populations densities are calculated with Multi3D (Leenaarts & Carlsson 2009), which allows to evaluate the three dimensional radiation field (3D NLTE hereafter). The Ca II atom model used in this work consists of 5 bound levels plus a continuum. We calculate the LTE departure coefficients, defined as

$$b_i = \frac{n_i}{n_i^*}, \tag{1}$$

where n_i represent the populations of an atomic level i computed in NLTE and n_i^* is the equivalent LTE population.

In the second step, the same atmospheric model is used to compute the LTE solution with Nicole. The LTE departure coefficients obtained previously are applied to the LTE populations computed by Nicole. In each column the model is truncated at the height where the temperature is higher than 25000 K and interpolated to an optimal grid for the radiative transfer calculations. The grid points are distributed according to gradients in temperature, density and opacity, placing more points where the gradients are large. The departure coefficients are interpolated to the new grid using an accurate interpolation algorithm based on Hermite polynomials (Hill 1982).

Our synthetic line profiles show the same chromospheric features as in Leenaarts et al. (2009), which is not surprising since the same 3D snapshot and atom level populations are used. Figure 2 shows the monochromatic full Stokes vector at -75 mÅ from the core of the Ca II 8542 Å line. These polarization profiles are induced by Zeeman splitting in the presence of an average magnetic field of 150 G. The Stokes Q and U profiles show amplitudes of the order of 10^{-4}, peaking around 10^{-3} where the magnetic field is strong and mostly horizontally oriented. The Stokes V signal is one order of magnitude higher than Stokes Q and U, usually within the range $[10^{-3}, 10^{-2}]$, and shows extended areas with the same polarity.

2.3. Observability of Stokes signals

This study is partially motivated by the instrumental requirements of future telescopes that are now under considerations. In this context, Fabry-Pérot Interferometers (FPI) have become very popular as they allow a balanced trade-off between cadence, spatial resolution and spectral resolution. We analyse the combined effect of noise and spectral resolution on the Stokes profiles.

Leenaarts et al. (2009) pointed out that the core of the synthetic Ca II 8542 line is narrower and *steeper* than those from actual observations, probably from the lack of small scale random motions in the model. Thus, our Stokes Q, U and V spectra are unrealistically strong and narrow. Assuming Zeeman splitting in a weak field regime, the shape of Stokes Q and V can be expressed as a function of the first derivative of the intensity (Landi Degl'Innocenti & Landolfi 2004).

$$Q(\lambda) = -\frac{1}{4}\Delta\lambda_B^2 \bar{G} \frac{\eta''}{\eta'} \left(\frac{\partial I}{\partial \lambda}\right) \tag{2}$$

$$V(\lambda) = -\Delta\lambda_B \bar{g} \cos\theta \left(\frac{\partial I}{\partial \lambda}\right) \tag{3}$$

where $\Delta\lambda_B$ represents the Zeeman splitting of the line, $\bar{g}$ is the Landé factor, θ is the inclination, $\bar{G}$ depends on the quantum numbers of the line and η is the Voigt profile. According to Eqs. 2 and 3 the amplitude of Stokes Q and V is enhanced if the slope of Stokes I is large. Thus, sharper Stokes I profiles produce more strongly peaked Stokes Q, U and V profiles.

We conclude that the effect of instrumental degradation would be overestimated and the effect of noise underestimated due the width and amplitude of our profiles. In order to make more realistic predictions, we introduce an artificial micro-turbulence in the model. Without micro-turbulence, the width of the chromospheric core measured in our spatially-resolved spectra is of the order of 180 mÅ. Corresponding measurements from *quiet* Sun line profiles were carried out by Cauzzi et al. (2009), who find values in the range 450-550 mÅ. This means that our profiles are of the order of a factor 2.5 narrower than observed. By artificially introducing micro-turbulence of 3 km s^{-1} the width of our profiles is increased up to $\sim$ 400 mÅ. This value of micro-turbulence is consistent with the chromospheric average calculated from the Val-C model (Vernazza et al. 1981).

A comparison between the spatially-averaged spectrum with and without micro-turbulence is illustrated in Fig. 3.

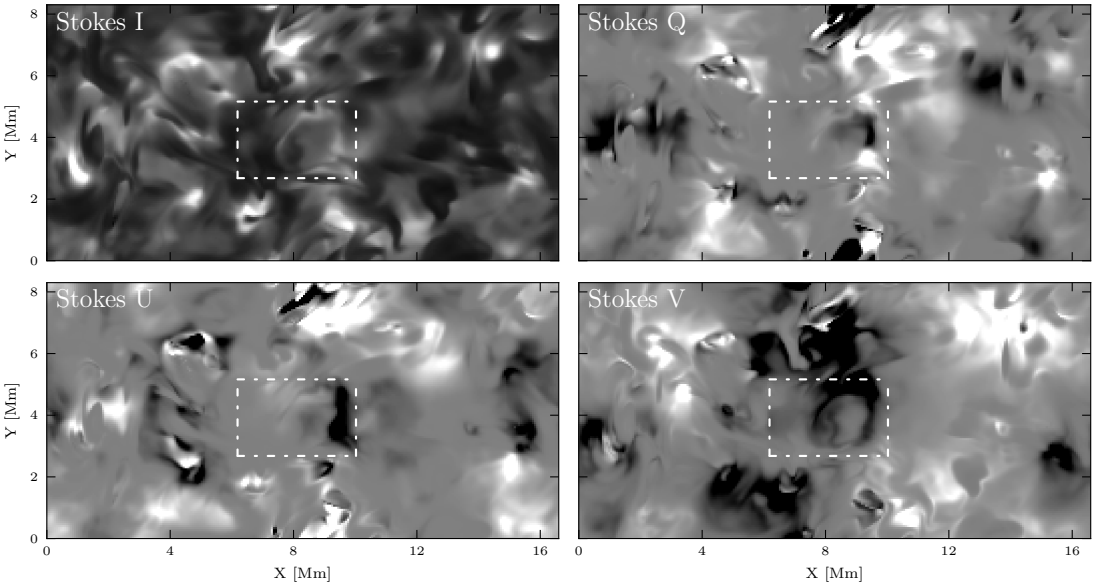

Fig. 2. Stokes images at -75 mÅ from the core of the line. The Stokes Q and U images are scaled between ±0.002 and Stokes V is scaled between ±0.02, relative to continuum intensity. The white box indicates the area selected to carry out inversions.

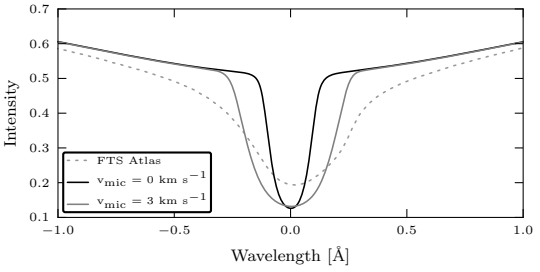

Fig. 3. Spatially averaged profile without micro-turbulence (black-solid), with micro-turbulence (grey-solid) and the FTS atlas

Our synthetic spectra are convolved with a Gaussian Point Spread Function (PSF) in order to emulate instrumental degradation. Additive Gaussian noise is introduced after applying this degradation. Instrumental PSFs are characterized by their Full Width Half Maximum (FWHM), and hereafter we refer to this parameter when instrumental degradation is discussed. The added noise is characterized in terms of its standard deviation,σ

Our results are illustrated in Figs. 6 and 7 at +205 mÅ from the line core. The noise value and spectral degradation are indicated inside each panel. In Fig. 6 spectral degradation spans the range $[0, 100]$ mÅ, in 25 mÅ steps. In the vertical direction, noise takes the following values from top to bottom: 0, $10^{-4}, 10^{-3}$. Fig. 7 corresponds to Stokes V images where spectral resolution is also degraded from left to right. Only the case corresponding to $\sigma = 10^{-3}$ is shown because the signal is well above noise in all other cases.

In the top row of Fig. 6 only spectral degradation is applied. Even though the amplitude of Stokes Q is decreased around a factor 2 between FWHM = 0 mÅ and FWHM = 100 mÅ, the main features are still visible at maximum spectral degradation (see Fig. 5 where different levels of spectral degradation are shown).

The middle row (panels *(f)* - *(j)*) corresponds to $\sigma = 10^{-4}$. Stokes Q is still above noise for all the assumed values of the FWHM. This result is somewhat expected because our Stokes Q profiles usually peak within $[10^{-4}, 10^{-3}]$, so noise only affects the very weak polarization signals.

The bottom row of Fig. 6 corresponds to $\sigma = 10^{-3}$, where noise clearly dominates the Stokes Q images. Some regions with strong polarization in Q are discernible in panels *(k)* and *(l)* (FWHM $\leq$ 25 mÅ) but barely visible when FWHM = 50 mÅ. Above this value, Stokes Q vanishes below noise due to spectral degradation.

The most advanced FPI instruments that are currently operating in solar telescopes can typically achieve a spectral resolution of 45-100 mÅ in the near infrared, with noise levels of the order of 10^{-3}. Those cases correspond to panels *(m)*, *(n)* and *(o)* in Fig. 6 and 7. Our results suggest that Stokes V detections are possible with current instrumentation. However, detections of linear polarization in *quiet* Sun require sensitivities of the order of 10^{-4}.

Exposure time in solar observations is limited by the evolution time of the Sun. Longer exposures than the evolution time scale of the any fine structure can produce smearing of the data. Particularly, image reconstruction assumes that the Sun is static for a given set of short exposure images. In that context, the vigorously dynamic chromosphere shows features moving horizontally within few seconds (van Noort & Rouppe van der Voort 2006). Thus observing the chromosphere involves a dif-

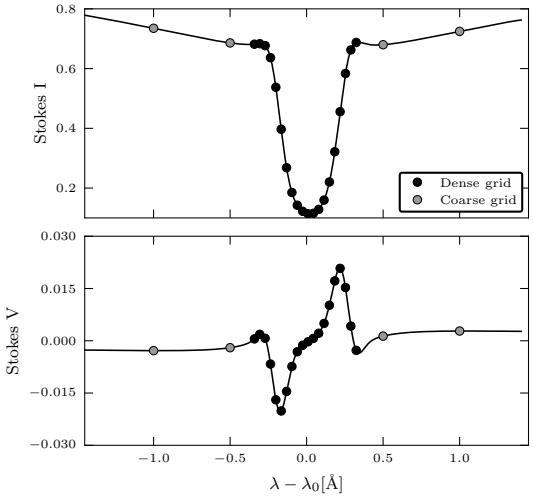

Fig. 4. Stokes I and V profiles from one of the columns from the 3D model. The grey circles indicate a coarse grid of points located outside the the chromospheric range of the line. The black circles sample the core of the line every 35 mÅ.

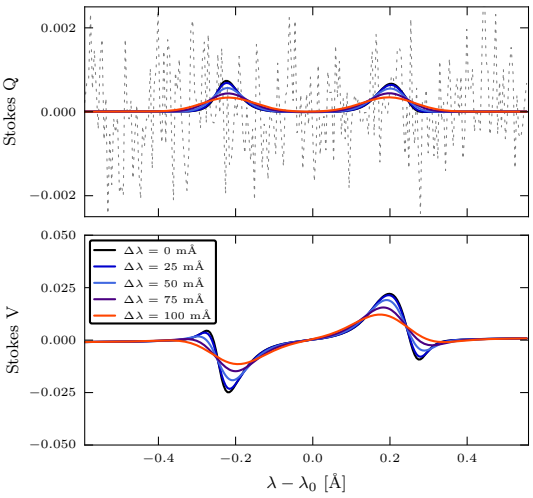

Fig. 5. Degradation of the Stokes Q and V signals as a function of the instrumental resolution. The dotted line in the upper panel illustrates $\sigma = 10^{-3}$.

ficult trade off among wavelength coverage, exposure time and cadence.

There are ways to ameliorate the sampling. The broad Ca II infrared lines have a large formation range: the fast moving features observed in the cores contrast with the slow evolution of photospheric granulation present in the wings of the lines. Additionally, the amplitude of Stokes Q, U and V rapidly decreases towards the wings of the line. A strategy to optimize the polarization measurements and proper time sampling would be to place a fine grid of points in the chromospheric core and a coarser grid at the wings, where slower variations are expected. As the photosphere evolves on a longer time scale than the chromosphere, exposures in the wings do not have to be recorded as frequently as in the core. Fig. 4 illustrates this scheme, with a fine grid of points (black circles) distributed along the core every 35 mÅ and a coarser grid at the wings (grey circles) placed every 500 mÅ.

3. Inversions

Nicole solves the NLTE problem assuming plane-parallel geometry and complete redistribution in angles and frequencies, using the strategy described by Socas-Navarro & Trujillo Bueno (1997). All the Zeeman sub-levels originating from a given atomic level are assumed to be equally populated, discarding any quantum interference between them, as proposed by Trujillo Bueno & Landi Degl'Innocenti (1996).

Nicole makes use of the *velocity-free* approximation, by assuming a static atmosphere when the populations are computed. In these conditions only half of the profile needs to be computed and fewer quadrature angles are needed. This allows fast processing and gives stable convergence properties.

The inversions are initialized with a guess model which contains of temperature, electron pressure, line-of-sight (l.o.s.) velocity, micro-turbulence and the three components of the magnetic field vector. The inversion engine of Nicole is based on a Levenberg-Marquardt algorithm that computes the corrections to a guess model in order to minimize the differences between the observed and the synthetic profiles.

In order to maintain physical consistency between temperature, electron pressure and gas pressure, the model is set to hydrostatic equilibrium after each correction. Those are applied at node points that are equidistantly distributed over the depth scale of the model. The inversions are initialized with the VAL-C model, and carried out with 11 nodes in temperature, 6 nodes in velocity, 4 nodes in longitudinal magnetic field (B_z), and 2 nodes in the horizontal components of the magnetic field vector (B_x and B_y). After the first inversion, the parameters of the VAL-C model are randomized to start the inversion from a different solution. Each pixel is inverted with 5 different initializations.

3.1. Velocity and magnetic field in LTE

The intensity absorption profile of a given spectral line is given by the expression (see, e.g. Landi Degl'Innocenti 1992):

$$\kappa_I(\lambda, T, \boldsymbol{B}, v_{los}) = \kappa_C(T) + \frac{1}{2}\eta_0(T, n_l, n_u)\Big[\phi_p(\lambda, \boldsymbol{B}, v_{\rm los})\sin 2\theta + \frac{\phi_b(\lambda, \boldsymbol{B}, v_{\rm los}) + \phi_r(\lambda, \boldsymbol{B}, v_{\rm los})}{2}(1+\cos 2\theta)\Big], \quad (4)$$

where κ_C is the continuum absorption coefficient, η_0 is the line strength, ϕ_p, ϕ_b and ϕ_r are the π, blue and red profile components, respectively (the notation employed is also from Landi Degl'Innocenti 1992).

Assuming LTE, Eq. (4) shows explicitly the dependencies on the temperature (and other thermodynamical parameters such as density or pressure) T, magnetic field vector $\boldsymbol{B}$ and the l.o.s. velocity $v_{\rm los}$ are. For the continuum absorption coefficient κ_C we have neglected the wavelength dependence because the continuum opacity varies with wavelength much more slowly than for the line. The atomic level populations of the lower and upper levels of the transition considered, n_l and n_u, obviously depend

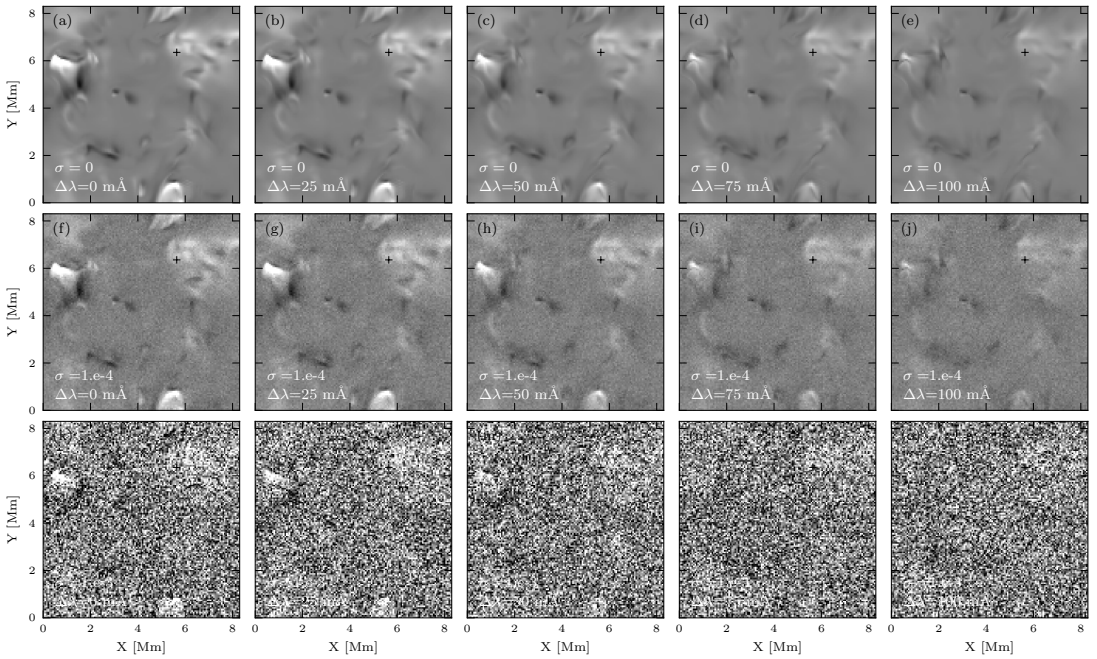

Fig. 6. Stokes Q image spectrally degraded with Gaussian PSFs and random noise. From left to right, the spectral degradation increases as a function of the FWHM of the Gaussian, from $\Delta\lambda = 0$ (no convolution) to $\Delta\lambda = 100$ mÅ. From top to bottom, the noise component increases, from $\sigma = 0$ to $\sigma = 10^{-3}$. The images are scaled to ±0.15% relative to the continuum intensity.

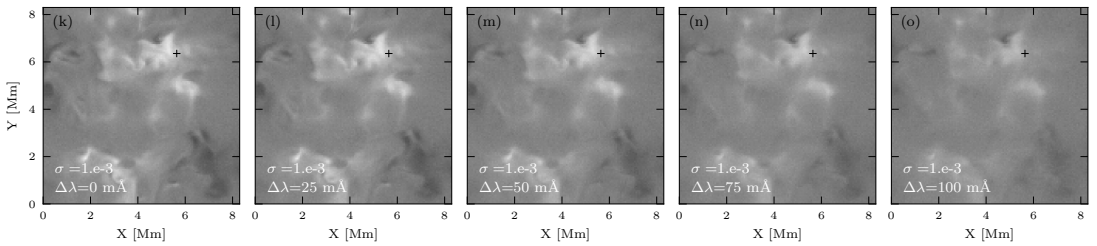

Fig. 7. Stokes V image spectrally degraded with Gaussian PSFs. From left to right, the spectral degradation increases as a function of the FWHM of the Gaussian, from $\Delta\lambda = 0$ (no convolution) to $\Delta\lambda = 100$ mÅ. A Gaussian random noise component of $\sigma = 10^{-3}$ has been added. The images are scaled to ±5% relative to the continuum intensity.

on T as well (in practice, the atomic populations may be considered to be independent of $\boldsymbol{B}$ and $v_{\rm los}$ even in conditions far from LTE), unless gradients in velocities are very large.

In Eq. (4) there is a convenient separation of the atmospheric parameters (the unknowns of our inversions). The dependence on the thermodynamical parameters T is contained exclusively in κ_C and η_0, whereas the dependencies on the magnetic field $\boldsymbol{B}$ and the velocity $v_{\rm los}$ are in the term enclosed in square brackets. The same happens with the equivalent absorption profiles for the rest of the Stokes parameters κ_Q, κ_U, κ_V, as well as the emission and the anomalous dispersion profiles. They can all be separated into a term containing the atomic populations and the thermodynamic properties and another term containing the wavelength profiles with the dependence on $\boldsymbol{B}$ and $v_{\rm los}$.

This separation of variables is fortunate because if we are not interested in the temperature but only in the magnetic field and velocity, it is possible to devise a much simpler inversion for these quantities. Such simpler inversion would not require the solution of a NLTE problem and would therefore not be subject to the limitation of approximations such as hydrostatic equilibrium, neglecting 3D effects or instantaneous recombination.

Let us consider now one such simplistic procedure, namely one that fits the observed profiles computing the atomic populations in LTE. With the inversion we obtain a run of thermodynamic parameters T^* which is, in general, different from the real T in the solar atmosphere. From that T^* we compute LTE populations n_l^* and n_u^*.

In order to fit the observational data, however, the atomic level populations and the line strength obtained must be simi-

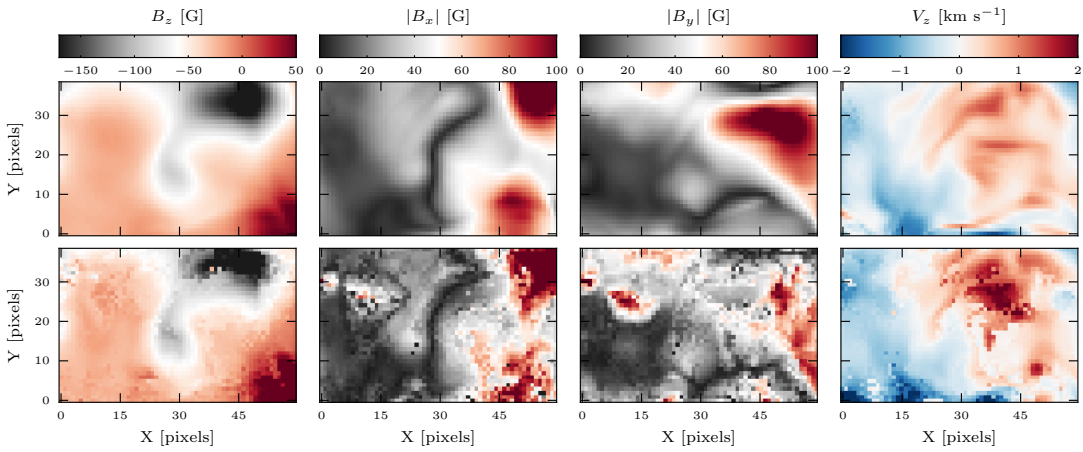

Fig. 8. Results from an inversion carried out in LTE. The top row illustrates quantities from the 3D snapshot and the bottom row the results of the inversion. All quantities are averaged in the $\log(\tau_{5000})$ range between −4 and −6.

lar (within the inversion uncertainties, of course, but this would be independently of whether one uses LTE or NLTE) to the real populations and line strengths. This, in turn, implies that the term within the square brackets of Eq (4) must also be properly reproduced, otherwise we would not be able to fit the observations. Ultimately we would recover $\boldsymbol{B}$ and v_{los} with the same degree of accuracy as with a NLTE inversion, and only T would be wrong.

With the same reasoning, we argue that questioning the validity of the assumptions that we have made on the radiative transfer (such as hydrostatic equilibrium, 1D atmosphere or instantaneous recombination) would only be relevant in the determination of T but not $\boldsymbol{B}$ or v_{los}.

Figure 8 depicts the result of inverting $\boldsymbol{B}$ and v_{los} in a region of the simulation. Due to the computational requirements of the NLTE inversions discussed below, we restrict ourselves to a smaller section of the 3D snapshot, indicated with a white box in Fig. 2. To facilitate comparisons among the various results, we apply the LTE inversions of this section to the same subfield. The results presented are averaged in the range of from $\log(\tau_{5000})$=−4 to $\log(\tau_{5000})$=−6 (where τ_{5000} is the continuum optical depth at 5000 Å), spanning the entire chromosphere. Note that the inversion results may not be very meaningful if a single height is isolated because the radiative transfer is insensitive to a perturbation in $\boldsymbol{B}$ and v if it takes place over a region much smaller than the photon mean free path. Such a small perturbation would be transparent for the outgoing beam and would leave no imprint on the emergent profiles. As a result, it is possible to have small-scale fluctuations in the inversion results but those fluctuations should average out to approximately the same value as the 3D model, or otherwise the fitted profile would differ from the simulated observation. The height range has been picked more or less arbitrarily. It could perhaps be refined, e.g. using response functions (see, e.g., Uitenbroek 2006), but it has not been done in our study.

We can see in the figure that the results for B_z and v_{los} are better, with some noise coming primarily from inversions that failed to converge. This is illustrated in Fig. 9, which shows the difference in the fit between a pixel that converged to the correct solution and another one for which the algorithm settled in a secondary minimum of the χ^2 hypersurface. The noise created in the resulting image by imperfect fits (we will refer to this as *inversion noise* to avoid confusion with the usual photon noise found in the observations) can be minimized by implementing more sophisticated schemes with multiple initializations to ensure that one reaches the absolute minimum. Genetic algorithms (Charbonneau 1995) provide a suitable approach to the problem and have been successfully implemented in Stokes inversion codes (e.g., Lagg et al. 2004). However, such strategies (and especially the genetic algorithms) increase the computational requirements of the problem which is already very intensive in terms of processing. For this reason, we have refrained from implementing anything beyond the already mentioned 5 attempts with randomized initializations.

For B_x and B_y the results appear more noisy than for B_z. This is because the Stokes Q and U signals are weaker than Stokes V and also because the horizontal field component is weaker than the vertical component. In a realistic case, we would be dominated by the observational noise, except in very specific cases such as strong fields in the vicinity of sunspots.

The Pearsons correlation coefficient between the model and the inversion are 0.93 for B_z, 0.84 for v_{los}, 0.90 for B_x and 0.69 for B_y. The mean error (averaged over the inverted field) is of 10.2 G in B_z and 12.6 G in B_x and B_y, and 0.28 km s^{-1} in $v_{\rm los}$.

We defer a study of the degradation of the results with the noise in the simulated observations to Section 3.2 below. The purpose of this section has been to present an exploration of the feasibility of a simple inversion scheme to retrieve $\boldsymbol{B}$ and v_{los} in which the thermodynamical parameters are treated simply as formal fitting parameters and not as an actual estimate of the real solar quantities. This approach is actually similar to what is often done in Milne-Eddington inversions for the photosphere, in which only $\boldsymbol{B}$ and v_{los} are interpreted as physical parameters, even though several other parameters are involved in the fit.

3.2. Non-LTE inversions

We perform NLTE inversions of our simulated line profiles, which are first convolved with Gaussian functions of 25 and 50 mÅ FWHM. Random Gaussian noise is added with r.m.s. amplitudes $\sigma = 10^{-4}$ and $\sigma = 10^{-3}$, resulting in four differ-

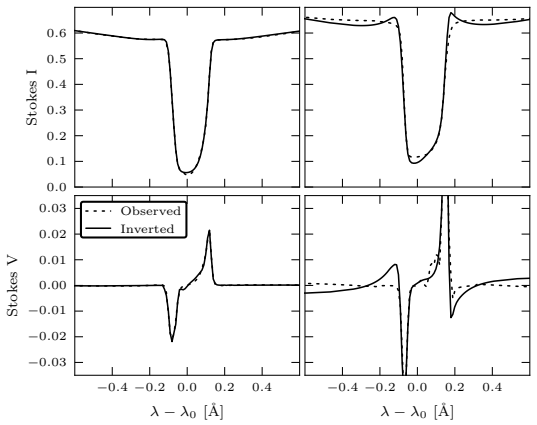

Fig. 9. Illustrative examples of the fits (solid line) to the simulated observations (dashed line) at two different locations in the LTE inversion of Fig. 8. Left panels: A good fit, at pixel coordinates (25,23) in Fig. 8. Right panels: A comparatively poorer fit at pixel coordinates (39,34). Upper row: Stokes I (normalized to the average continuum intensity). Lower row: Stokes V.

ent datasets. In this case, the observations do not include microturbulence, representing a though challenge for the inversion code. The results of the inversions in Figs. 10 and 11 represent an average of the chromospheric parameters computed from $\log(\tau_{5000})= -4$ to $\log(\tau_{5000})= -6$. Some quantitative details are presented in Table 1.

The l.o.s. velocity reconstructed by the inversion is unaffected by the spectral degradation and noise levels assumed in this study, and leading to similar results with all datasets. The noise in the inversion result is due to the inversion noise effect described earlier, related to imperfections in the fit. Fig. 11 compares integrated properties from the 3D model with the inversions. The inversion is able to recover most of the structure originally present in the simulation, with a correlation factor of 0.80.

The overall structure of the inverted temperature resembles that of the 3D snapshot (Fig. 11). The average relative error in the inferred temperature (measured as the difference between model and inversion divided by the model) is of 8%. The absolute error is of ∼400 K, but the temperature contrast in the chromosphere is so high (typically of several thousand degrees) that the agreement can be considered good. Even though this parameter is unaffected by the levels of noise considered in the inversions, the temperature contrast of the inverted field is reduced compared with that of the model. The exclusion of 3D NLTE effects when assuming plane-parallel geometry and the assumption of hydrostatic equilibrium is probably at least partially responsible for the disagreement.

The longitudinal magnetic field (B_z) is the most accurately retrieved parameter from the inversions. The Stokes V profiles usually peak well above the 10^{-3} level, thus similar results are obtained from all our datasets. The results in Fig. 10 clearly show a detailed correspondence between the input and output quantities.

The horizontal component of the magnetic fields is constrained in the inversion only by Stokes Q and U. The inversions with 10^{-4} noise do not differ from the noise free case. However, the datasets where noise is 10^{-3}, exhibit significant loss in structure and detail, as illustrated in Fig. 10.

In general the correspondence between observed and inverted profiles is good, however, our *observed* profiles are narrower than those from real solar observations. We find that the quality of the fits produced by Nicole is better for real observational data than for synthetic profiles calculated from the simulations.

Table 1. Linear relation ($y = ax + b$) between input and output quantities.

	FWHM [mÅ]	Noise [σ]	a	b	r^2
B_z	25	10^{-4}	0.96	-6.46	0.93
	50	10^{-4}	0.94	-7.55	0.92
	25	10^{-3}	0.94	-7.82	0.89
	50	10^{-3}	0.95	-7.07	0.93
B_x	25	10^{-4}	0.83	0.66	0.83
	50	10^{-4}	0.82	1.06	0.83
	25	10^{-3}	0.66	18.84	0.58
	50	10^{-3}	0.66	19.44	0.61
B_y	25	10^{-4}	0.54	11.29	0.67
	50	10^{-4}	0.54	11.46	0.67
	25	10^{-3}	0.41	27.64	0.41
	50	10^{-3}	0.41	28.53	0.42
v_z	25	10^{-4}	1.16	-0.01	0.77
	50	10^{-4}	1.16	-0.01	0.76
	25	10^{-3}	1.08	0.02	0.78
	50	10^{-3}	1.16	-0.01	0.76

4. Conclusions

We have computed full Stokes synthetic line profiles using a 3D MHD simulation of the outer atmosphere of the Sun. A full 3D evaluation of the NLTE problem is carried out using Multi3D. These line profiles are inverted using the inversion code Nicole, which solves the NLTE problem assuming plane parallel geometry. For clarity, the present study is made with the following assumptions and limitations:

1. All the polarization is produced by the Zeeman effect.
2. The average magnetic field strength in the 3D model is 150 G. Nicole is conceived to work o data from active region with stronger magnetic field, leading to Stokes Q and U profiles that are stronger.
3. The thermal width of the core of our Ca II line is approximately a factor 2.5 lower than for real observations.

The simulations are used to study the ability of inversions to reconstruct a realistic chromospheric model.The inversion results are more affected by noise than by instrumental degradation. In general, NLTE inversions provide good estimates of the l.o.s. velocity and longitudinal magnetic field. Results for horizontal fields strongly depend on the noise present in the observational data. Temperature is the less reliable quantity. It is difficult to disentangle whether this is because of 3D NLTE effects, difficulties to reproduce the transition region or the limited convergence of the fits. In the light of this results, the usability of Ca II lines to infer chromospheric quantities remains somewhat unclear, and future studies should focus on exploring new methods to improve inversions. Along those lines, we demonstrate that inversions carried out in LTE and NLTE provide similar estimates of the magnetic field vector and the l.o.s velocity. Inversions using multiple lines of the Ca II infrared triplet could help to improve the results presented in this work.

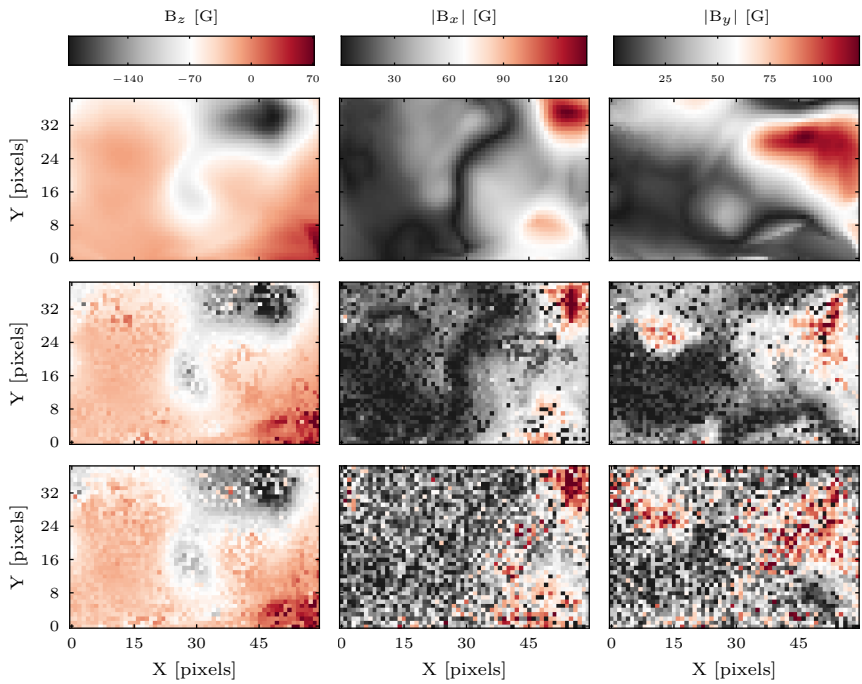

Fig. 10. Left to right B_z, $|B_x|$, $|B_y|$ respectively. *Top row:* properties of the 3D snapshot averaged between $\log(\tau_{5000})=-4$ and $\log(\tau_{5000})=-6$. *Middle row:* results of a inversion with 10^{-4} random noise added to the observed profiles. *Bottom row:* results of a inversion with 10^{-3} random noise added to the observed profiles. The data was spectrally degraded with a 25 mÅ PSF. This subfield corresponds to the white box indicated on Fig 2.

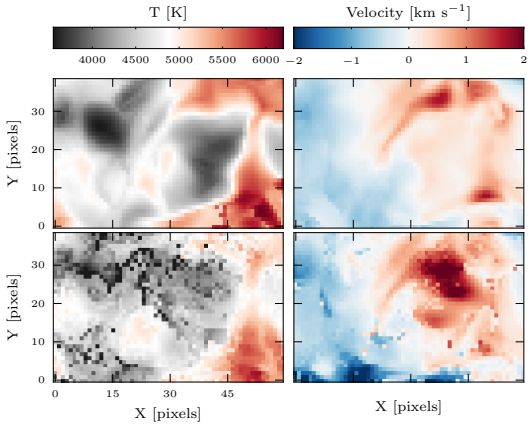

Fig. 11. Temperature (left column) and l.o.s. velocities (right column) for the 3D snapshot and respective NLTE inversions (top and bottom rows respectively).

Our work leads to a better understanding of the information contained in chromospheric Ca II observations and what can be learned from inversions. The tests presented here are very demanding because the simulated observations have been computed using departure coefficients from a different code (Multi3D) that incorporates more physical effects than the inversion code, most notably the inclusion of 3D NLTE transfer and the absence of hydrostatic equilibrium. Furthermore, the magnetic field in the simulation is very weak. In a real scenario one would be applying these inversion techniques to more active regions which produce more conspicuous signals. Finally, the lack of turbulent broadening results in profiles that have a lot of spectral fine structure with very narrow emission features and multi-peaked Stokes profiles (much more so than what is typically observed). This corrugates the χ^2 hypersurface and makes it more difficult for the Levenberg-Marquardt algorithm to reach the true minimum.

We have also proposed an optimal scheme to observe the chromosphere using the Ca II infrared lines. Our results suggest that in order to be able to detect and invert Stokes Q and U signals, the noise level should be significantly better than 10^{-3}.

Acknowledgements. HSN gratefully acknowledges financial support by the Spanish Ministry of Science and Innovation through project AYA2010-18029 (Solar Magnetism and Astrophysical Spectropolarimetry). JdlCR thanks Vasco Henriques for his comments on the manuscript. This research project has been supported by a Marie Curie Early Stage Research Training Fellowship of the European Community's Sixth Framework Programme under contract number MEST-CT-2005-020395: The USO-SP International School for Solar Physics.

References

Asensio Ramos, A., Trujillo Bueno, J., & Landi Degl'Innocenti, E. 2008, ApJ, 683, 542

Cauzzi, G., Reardon, K., Rutten, R. J., Tritschler, A., & Uitenbroek, H. 2009, A&A, 503, 577
Charbonneau, P. 1995, ApJS, 101, 309
Hansteen, V. H., Carlsson, M., & Gudiksen, B. 2007, in Astronomical Society of the Pacific Conference Series, Vol. 368, The Physics of Chromospheric Plasmas, ed. P. Heinzel, I. Dorotovič, & R. J. Rutten, 107–+
Hill, G. 1982, Publications of the Dominion Astrophysical Observatory Victoria, 16, 67
Lagg, A., Woch, J., Krupp, N., & Solanki, S. K. 2004, A&A, 414, 1109
Landi Degl'Innocenti, E. 1992, in Solar Observations: Techniques and Interpretation,First Canary Islands Winter School of Astrophysics, ed. F. Sánchez, M. Collados, & M. Vázquez (Cambridge Univ. Press), 71
Landi Degl'Innocenti, E. & Landolfi, M., eds. 2004, Astrophysics and Space Science Library, Vol. 307, Polarization in Spectral Lines
Leenaarts, J. & Carlsson, M. 2009, in Astronomical Society of the Pacific Conference Series, Vol. 415, Astronomical Society of the Pacific Conference Series, ed. B. Lites, M. Cheung, T. Magara, J. Mariska, & K. Reeves, 87–+
Leenaarts, J., Carlsson, M., Hansteen, V., & Rouppe van der Voort, L. 2009, ApJ, 694, L128
Manso Sainz, R. & Trujillo Bueno, J. 2010, ApJ, 722, 1416
Pietarila, A., Socas-Navarro, H., Bogdan, T., Carlsson, M., & Stein, R. F. 2006, ApJ, 640, 1142
Shine, R. A. & Linsky, J. L. 1974, Sol. Phys., 39, 49
Socas-Navarro, H., de la Cruz Rodríguez, J., Asensio-Ramos, A., Trujillo-Bueno, J., & Ruiz-Cobo, B. 2010, in preperation
Socas-Navarro, H. & Trujillo Bueno, J. 1997, ApJ, 490, 383
Socas-Navarro, H., Trujillo Bueno, J., & Ruiz Cobo, B. 2000, ApJ, 530, 977
Trujillo Bueno, J. & Landi Degl'Innocenti, E. 1996, Sol. Phys., 164, 135
Uitenbroek, H. 2006, in Astronomical Society of the Pacific Conference Series, Vol. 354, Solar MHD Theory and Observations: A High Spatial Resolution Perspective, ed. J. Leibacher, R. F. Stein, & H. Uitenbroek, 313–+
van Noort, M. J. & Rouppe van der Voort, L. H. M. 2006, ApJ, 648, L67
Vernazza, J. E., Avrett, E. H., & Loeser, R. 1981, ApJS, 45, 635

Paper III

Astronomy & Astrophysics manuscript no. paper
October 29, 2010

Are solar chromospheric fibrils tracing the magnetic field?

J. de la Cruz Rodríguez[1,2] and H. Socas-Navarro[3,4]

[1] Institute for Solar Physics, Royal Swedish Academy of Sciences, AlbaNova University Center, SE-106 91 Stockholm, Sweden
[2] Stockholm Observatory, AlbaNova University Center, SE-106 91 Stockholm, Sweden
[3] Instituto de Astrofísica de Canarias, Avda Vía Láctea S/N, La Laguna 38200, Tenerife, Spain
[4] Departamento de Astrofísica, Universidad de La Laguna, 38205, La Laguna, Tenerife, Spain

Preprint online version: October 29, 2010

ABSTRACT

Fibrils are thin elongated features visible in the solar chromosphere in and around magnetized regions. Because of their visual appearance they have been traditionally considered a tracer of the magnetic field lines. In this work we challenge that notion for the first time by comparing their orientation to that of the magnetic field, obtained via high-resolution spectro-polarimetric observations of Ca II lines. The short answer to the question posed in the title is that mostly yes, but not always.

Key words. Sun: activity - Polarization - Sun: chromosphere - Sun: filaments - Sun: magnetic topology - Sun: sunspots

Narrow-band solar filtergrams in the H I 6563 Å (Hα) line core show an ubiquitous pattern of fibrilar appearance covering most of the disk, often connecting patches of magnetic field. Although not as easily, the same pattern is visible in the chromospheric Ca II lines as well (e.g., Zirin 1974; Marsh 1976, for a recent reference see Pietarila et al. 2009). Fibril observation requires high spatial and spectral (particularly in Ca II) resolution, since they are very thin and observable only in the very core of the lines. Because of their visual appearance, which resembles magnetic field lines connecting the poles of a magnet, it has been traditionally assumed that fibrils indeed trace the chromospheric magnetic field. To our best knowledge, this common conception has never been actually put to test, probably because a proper empirical determination of the chromospheric magnetic field is very challenging, requiring high-resolution spectro-polarimetry in chromospheric lines. Only recently, suitable instrumentation for this purpose has become available. Kuckein et al. (2010) al have been able to make vector field determinations in filaments (where the magnetic field is relatively strong) using the TIP polarimeter (Collados et al. 1999).

The transverse (i.e., projected on the plane of the sky) component of the magnetic field, which is what we are interested in for this work, is determined solely by the observed linear polarization signals (Stokes Q and U profiles). Unfortunately, such signals are typically very weak and their observation presents numerous challenges. In order to extract a clear signal above the noise we select by hand a small segment along the direction of a fibril and average the Stokes Q and U profiles spatially to improve the signal-to-noise ratio (Q and U are averaged separately). From the profiles thus obtained we can determine the azimuth of the magnetic field on the plane of the sky.

We present here results from two different datasets acquired with two different instruments, a Fabry-Perot interferometer and a slit spectro-polarimeter. Due to the nature of the instrumentation employed, each dataset exhibits its own advantages and disadvantages for our purposes but they complement each other well, as we discuss below.

The first dataset is a spectro-polarimetric scan with the Spectro-Polarimeter for INfrared and Optical Regions (SPINOR, Socas-Navarro et al. 2006) of Ca II 8542 Å at the Dunn Solar Telescope of the National Solar Observatory/Sacramento Peak Observatory (Sunspot, NM, USA). The observing setup and the data are described in detail in that paper. We analyze a (λ, x, y) cube acquired by scanning the spectrograph slit over a 80×80″ field of view. Seeing conditions were exceptionally good at the time and aided by the adaptive optics system (Rimmele 2000), we achieved a spatial resolution of approximately 0.″6 (although this figure varies through the scan due to temporal fluctuations of the seeing). Because of its high quality, this dataset has also been used in previous papers for studies of the chromospheric field and electric currents in sunspots (Socas-Navarro 2005a,b). High spatial resolution is very important for the observation of fibrils, which are barely visible in typical spectroscopic observations with more modest resolution.

The second cube was acquired on 2008-06-10, with the Fabry-Perot interferometer CRisp Imaging Spectropolarimeter (CRISP, Scharmer 2006) in full Stokes mode at the Swedish 1-m Solar Telescope (SST, Scharmer et al. 2003). The Ca II 8542 Å line was sampled at 17 wavelength points between ±1.3 Å from the core of the line, separated equidistantly by 162 mÅ. The instrumental profile of CRISP has a Full Width Half Maximum of approximately 100 mÅ at 8542 Å. The images are processed using the image resconstruction code MOMFBD (van Noort et al. 2005), according to the scheme described in van Noort & Rouppe van der Voort (2008) and Schnerr et al. (2010). The polarimetric response of the telescope is calibrated using a 1 meter polarizer, mounted on the entrance lens. Calibration images are used to fit the parameters of a theoretical model of the telescope as in Selbing (2005).

The SPINOR observations have better spectral resolution (120 mÅ dominated by instrumental resolution vs 324 dominated by spectral sampling) and slightly higher polarimetric sensitivity. The noise in the Stokes parameters in the absence of signal (measured as the standard deviation in the continuum away from magnetic areas) is of 4.5×10^{-4} and 1.3×10^{-3}, respectively, in units of the average quiet Sun continuum intensity. The spa-

tial averaging of the profiles that we carry out in our analysis works well in improving the magnetic sensitivity as long as the observations are photon noise limited. However, at some point one reaches a limit in which the uncertainties are dominated by other factors such as the goodness of the calibration, flatfielding, spurious artifacts introduced in the image reconstruction process and so forth. In the SPINOR case, this limit is reached at approximately 5×10^{-5}, whereas for CRISP it is around 10^{-4}. The CRISP observations, on the other hand, have much better spatial resolution (0.″2 vs 0.″6) and the linear polarization reference direction is known. It is then possible to derive the absolute azimuth direction without any further assumptions. For SPINOR, unfortunately, the linear polarization reference frame was not known and we need to resort on an *a posteriori* calibration of the zero azimuth using the data themselves. For this, we have used a number of penumbral filaments visible in the sunspot photosphere and calculated the field azimuth in those locations as explained below. A constant offset was added to all the azimuth values and adjusted until the field orientation matched all the filaments simultaneously. The resulting offset uncertainty (which propagates directly into the fibril azimuth determinations) is of approximately 2°.

In both cases (SPINOR and CRISP) we work with observations of strong magnetic fields (in the vicinity of a sunspot) to ensure that the polarization induced in the spectral lines is produced by the Zeeman effect. In the quiet Sun, one would have to deal with complications due to the intervention of the Hanle effect, which not only depolarizes the light (this would be irrelevant for our study) but also changes the relative amplitudes of Stokes Q and U (Manso Sainz & Trujillo Bueno 2010). Most of the fibrils studied here are of a category that is sometimes referred to as *superpenumbral fibrils* because they originate just beyond the boundary of a sunspot penumbra.

Figure 1 shows the chromospheric field of view observed with SPINOR in a grayscale image. Overplotted on top of that image are yellow lines indicating the fibril segments that we have manually picked for analysis. The selection has been made based not only on the appearance of the fibrils but also on the presence of linear polarization. The Stokes profiles inside the band defined by each segment and a width of 3 pixels have been averaged to produce one low-noise set of Stokes profiles for each fibril. Then the azimuth χ is obtained using the following formula (Jefferies et al. 1989):

$$\tan(2\chi) = \frac{\int_0^\infty f(\lambda)U(\lambda)}{\int_0^\infty f(\lambda)Q(\lambda)}, \quad (1)$$

where $f(\lambda)$ is a bandwith selection function. In this case we take $f(\lambda)$ to be a rectangular function of width 300 mÅ centered on the average position of the Stokes Q and U blue peak, very close to the line core. In the CRISP case we take a single wavelength, where the observed linear polarization signal is maximal. The validity of this approximation is further confirmed *a posteriori* since it provides azimuth values that match the orientation of the photospheric penumbral filaments in the SPINOR dataset.

For each fibril the azimuth was calculated 100 times using Eq (1) and adding different noise realizations to the Q and U profiles. The spread in the results obtained allows us to estimate the uncertainties involved. The red cones drawn in the figure on the yellow segments outline all the azimuth realizations obtained for each fibril. Table 1 lists the values of azimuth obtained compared to the orientation of the fibrils. The rightmost column lists the discrepancy in units of the spread (σ_χ). When this value is significantly larger than 3 we have a very high probability that the magnetic field orientation is incompatible with that of the fibril.

Table 1. Fibril orientation χ_{Fibril} and magnetic field azimuth χ_{Field} in the chromosphere of the SPINOR dataset.

Index	χ_{Fibril}	$\chi_{Field} \pm \sigma_\chi$	$\lvert\Delta\chi\rvert/\sigma_\chi$
1	34.7	153.4 ± 13.0	9.13
2	216.7	164.0 ± 9.0	5.86
3	195.2	161.5 ± 8.0	4.22
4	80.1	104.4 ± 8.4	2.91
5	103.1	131.6 ± 4.7	6.06
6	125.4	140.1 ± 5.1	2.91
7	142.4	159.1 ± 7.3	2.28
8	175.1	154.8 ± 8.2	2.49
9	144.8	154.6 ± 12.0	0.81
10	149.7	155.9 ± 4.3	1.43
11	158.3	158.5 ± 5.3	0.03
12	184.2	179.2 ± 4.5	1.11
13	185.6	174.2 ± 4.0	2.83
14	186.6	197.7 ± 4.6	2.42
15	214.3	215.8 ± 4.1	0.35
16	28.9	53.7 ± 4.8	5.18
17	39.8	50.4 ± 5.1	2.10
18	43.3	58.1 ± 4.2	3.54
19	59.7	64.1 ± 4.0	1.08

Notice how most fibrils are aligned with the magnetic field, which is a reassuring indication that the procedure works and that the linear polarization reference frame has been chosen correctly. However, there are a few noteworthy cases where significant misalignments occur, well above the observational error. The most obvious are located on the bottom left portion of the map (fibrils 1 through 5), near the smaller sunspot. Another interesting region is just above the large spot, where we find fibrils perfectly aligned with the field up until number 15, then a large misalignment in number 16 which gradually decreases in 17 and 18 until finally number 19 is again well aligned.

For comparison, Fig. 2 shows the same for the photospheric penumbral filaments used to determine the absolute azimuth reference position. The Q and U signals are stronger inside the penumbra, which is why the uncertainties are smaller. The solar limb is towards the right in the figure and therefore the transverse component is stronger on the right-hand side of the penumbra due to projection effects. Notice how in this figure the field is much better aligned with the filaments.

We have observed a similar behavior in the CRISP data, for which the absolute azimuth reference is known (see Fig. 3 and Table 2). Most fibrils that show polarization signal have a magnetic field that is oriented along the fibril direction, at least within the margin allowed by the data. However, some areas (e.g., the region with fibrils number 4, 6, 7 and 9) have a field orientation that differs significantly from that of the fibrils.

In the light of these results, we conclude that the widespread idea that chromospheric fibrils are a visual proxy for the magnetic field lines may need to be reconsidered. Here we have limited ourselves to presenting observational evidence. An attempt to explain the appearance of the chromospheric fibrilar pattern and the nature of fibrils themselves is beyond our scope. We speculate that perhaps the small difference in formation height between the Ca II line core (where the fibrils are seen) and the Stokes Q and U peaks (where the magnetic field is measured) might explain the discrepant behavior. This would still be a very surprising result anyway because conceiving a field topology

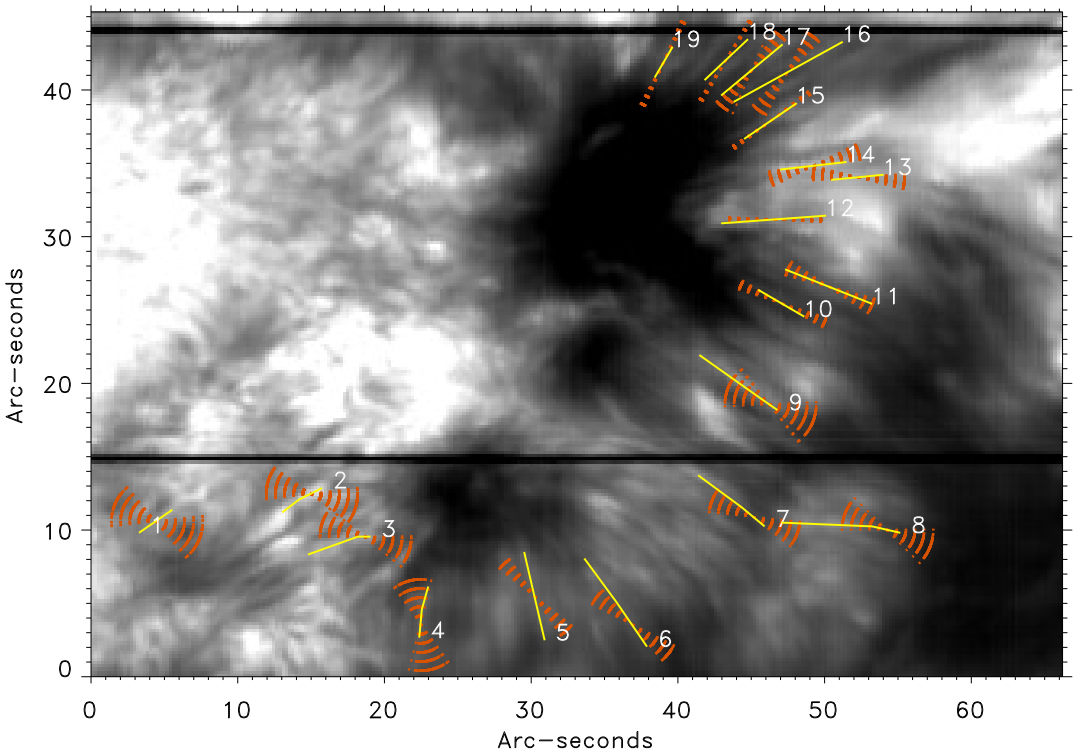

Fig. 1. Field of view observed with SPINOR in the core of Ca II 8542 Å. Yellow lines: Fibrils selected for analysis. The yellow segments define the direction of the 3-pixel wide bands used for Stokes Q and U profile averaging. Red cones: Range of magnetic field azimuth compatible with the Q and U profiles. The spatial sampling is 0.″22/pixel

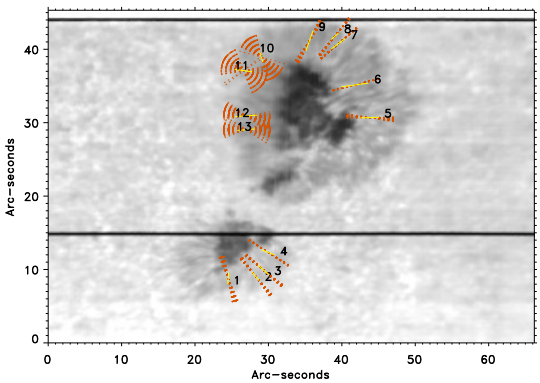

Fig. 2. Field of view observed with SPINOR in the wings of Ca II 8542 Å. Yellow lines: Penumbral filaments selected for analysis. The yellow segments define the direction of the 3-pixel wide bands used for Stokes Q and U profile averaging. Red cones: Range of magnetic field azimuth compatible with the Q and U profiles. The spatial sampling is 0.″22/pixel

with such strong vertical gradients in field orientation, especially in the low-β realm of the chromosphere (where magnetic field pressure and tensions are more difficult to sustain as the field dominates the dynamics of the plasma), is very challenging. Another possibility could be that the field changes rapidly in time and the plasma temperature structure (which is what ultimately dictates the intensity pattern observed) lags behind it somehow. Or perhaps the explanation is an entirely different one. In any case, we point out that the linear polarization sig-

Table 2. Fibril orientation χ_{Fibril} and magnetic field azimuth χ_{Field} in the chromosphere of the CRISP dataset.

Index	χ_{Fibril}	$\chi_{Field} \pm \sigma_\chi$	$\lvert\Delta\chi\rvert/\sigma_\chi$
1	176.1	175.6 ± 11.5	0.04
2	185.7	165.8 ± 4.4	4.53
3	178.0	171.1 ± 4.2	1.65
4	180.0	150.2 ± 3.5	8.55
5	196.9	157.9 ± 8.0	4.85
6	226.1	137.3 ± 3.0	29.97
7	28.9	109.6 ± 6.5	12.41
8	48.3	65.7 ± 14.6	1.19
9	62.3	106.2 ± 6.1	7.19
10	67.9	55.2 ± 5.9	2.15
11	92.1	93.0 ± 10.1	0.09
12	82.6	85.4 ± 4.6	0.60
13	126.3	75.4 ± 9.4	5.43

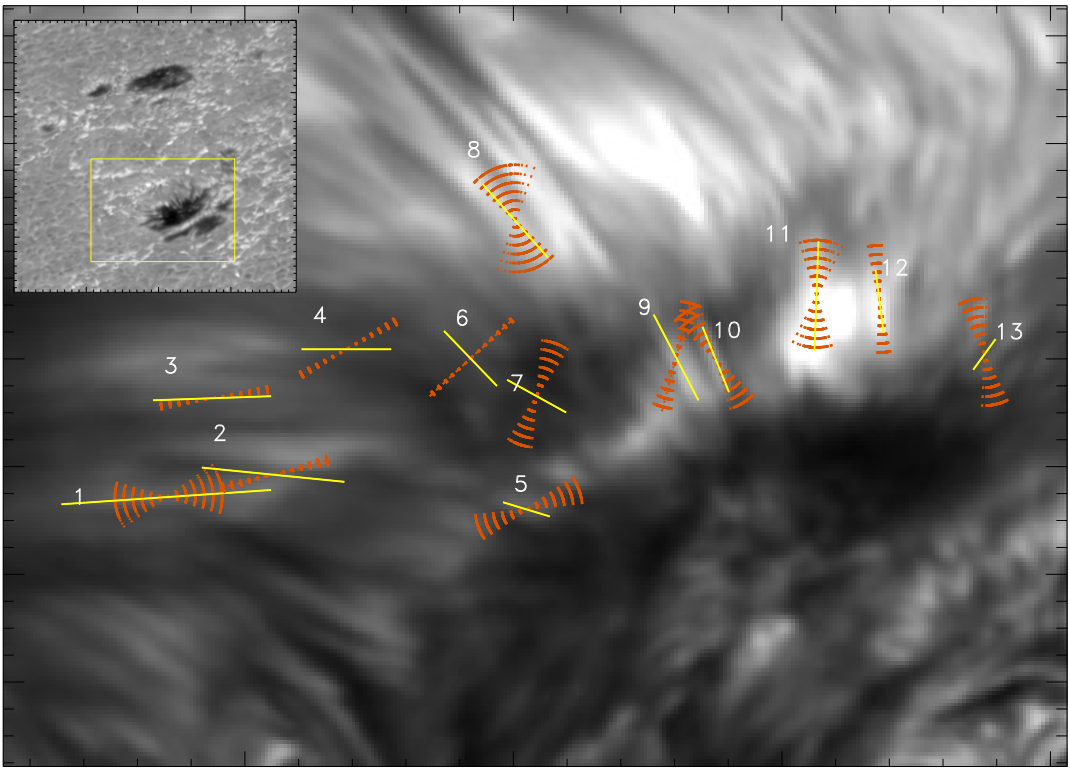

Fig. 3. Field of view observed with CRISP in the wing of Ca II 8542 Å. Inset: Detailed view of the line core in the region of interest. Yellow lines: Fibrils selected for analysis. The yellow segments define the direction of the 3-pixel wide bands used for Stokes Q and U profile averaging. Red cones: Range of magnetic field azimuth compatible with the Q and U profiles. The tick-mark separation is 1″ and 0.″5 on the X and Y axes, respectively. The intensity scale has been saturated to enhace the contrast of fibrils.

nal observed in the chromosphere around sunspots drops very abruptly as one moves outwards from the edge of the penumbra and this fact is very difficult to fit with the large size of the fibrilar patterns that are seen around it, if such fibrils are indeed magnetic field lines, because in that case the chromospheric field strength (and the linear polarization signal) should not drop off so abruptly as it is observed.

Although the data and the analyses presented here are reasonably well established, our work obviously has some limitations. Given the relevance of this subject, further observational studies should be conducted to confirm our refute these results. The main goal of our letter is to draw attention on the subject since modern instrumentation now enables the determination of the magnetic field vector in fibrils. A more definite and comprehensive answer to the question raised in this paper should be something that can be realistically expected for the near future with the existing and upcoming tools for solar observations and their interpretation.

Acknowledgements. We are grateful to Luc Rouppe van der Voort for providing the SST/CRISP observations. This research project has been supported by a Marie Curie Early Stage Research Training Fellowship of the European Communitys Sixth Framework Programme under contract number MEST-CT-2005-020395: The USO-SP International School for Solar Physics.
Financial support by the Spanish Ministry of Science and Innovation through project AYA2010-18029 (Solar Magnetism and Astrophysical Spectropolarimetry) is gratefully acknowledged by HSN.

References

Collados, M., Rodríguez Hidalgo, I., Bellot Rubio, L., Ruiz Cobo, B., & Soltau, D. 1999, in Astronomische Gesellschaft Meeting Abstracts, 13
Jefferies, J., Lites, B. W., & Skumanich, A. 1989, ApJ, 343, 920
Kuckein, C., Centeno, R., & Martinez Pillet, V. 2010, ArXiv e-prints
Manso Sainz, R. & Trujillo Bueno, J. 2010, ApJ, 722, 1416
Marsh, K. A. 1976, Sol. Phys., 50, 37
Pietarila, A., Hirzberger, J., Zakharov, V., & Solanki, S. K. 2009, A&A, 502, 647
Rimmele, T. R. 2000, in Proc. SPIE Vol. 4007, p. 218-231, Adaptive Optical Systems Technology, Peter L. Wizinowich; Ed., 218–231
Scharmer, G. B. 2006, A&A, 447, 1111
Scharmer, G. B., Bjelksjo, K., Korhonen, T. K., Lindberg, B., & Petterson, B. 2003, in Presented at the Society of Photo-Optical Instrumentation Engineers (SPIE) Conference, Vol. 4853, Society of Photo-Optical Instrumentation Engineers (SPIE) Conference Series, ed. S. L. Keil & S. V. Avakyan, 341–350
Schnerr, R. S., de la Cruz-Rodriguez, J., & van Noort, M. 2010, *in preparation*
Selbing, J. 2005, Master's thesis, Stockholm University
Socas-Navarro, H. 2005a, ApJ, 633, L57
Socas-Navarro, H. 2005b, ApJ, 631, L167
Socas-Navarro, H., Elmore, D., Pietarila, A., et al. 2006, Solar Physics, 235, 55
van Noort, M., Rouppe van der Voort, L., & Löfdahl, M. G. 2005, Sol. Phys., 228, 191
van Noort, M. J. & Rouppe van der Voort, L. H. M. 2008, A&A, 489, 429
Zirin, H. 1974, Sol. Phys., 38, 91

Paper IV

Astronomy & Astrophysics manuscript no. 6302
October 26, 2010

Stokes imaging polarimetry using image restoration at the Swedish 1-m Solar Telescope II

A calibration strategy for Fabry-Pérot based instruments

R. S. Schnerr, J. de la Cruz Rodríguez, and M. van Noort

Institute for Solar Physics of the Royal Swedish Academy of Sciences, AlbaNova University Center, SE-106 91 Stockholm, Sweden
Stockholm Observatory, AlbaNova University Center, SE-106 91 Stockholm, Sweden

Preprint online version: October 26, 2010

ABSTRACT

Context. The combination of image restoration and a Fabry-Pérot interferometer (FPI) based instrument in solar observations results in specific calibration issues. FPIs generally show variations over the field-of-view while in the image restoration process the 1-to-1 relation between pixel space and image space is lost, complicating correcting for such variations.
Aims. To develop a data reduction method that takes these issues into account, and minimizes the resulting errors.
Methods. By accounting for the time variations in the telescope Mueller matrix and using separate calibration data optimized for the wavefront sensing in the MOMFBD image restoration process and for the final deconvolution of the data we remove most of the calibration artifacts from the resulting data.
Results. Using the presented method to reduce full Stokes data from CRISP at the SST, we find that it drastically reduces the instrumental and image restoration artifacts resulting from cavity errors, reflectivity variations and the polarization dependence of flatfields. The resulting data allows for useful scientific interpretation. Inversions of restored data from the δ sunspot AR11029 using the Nicole inversion code, reveal strong (up to 10 km s^{-1}) downflows near the disk center side of the umbra.
Conclusions. There are calibration issues and intrinsic limitations to the accuracy that can be achieved, when using image restoration in combination with an FPI based instrument. We find that considering the polarimetric accuracy of CRISP at the SST of $\sim 10^{-3}$ these issues can be kept mostly under control. Similar instruments aiming for higher polarimetric and high spectroscopic accuracy, will, however, need to take these issues into account.

Key words. Techniques: image processing, polarimetric, imaging spectroscopy, Sun: surface magnetism, sunspots, activity

1. Introduction

As technical possibilities increase, more advanced and complicated instruments are being designed for observational studies of the Sun. New instrumentation is generally designed to offer better spatial resolution in order to resolve, e.g., small scale magnetic fields in the quiet Sun and magnetic fields and flows in sunspot penumbra, lightbridges and umbral dots, but also better spectral coverage and full polarization information which are needed to enable meaningfull interpretation of observed features. Adaptive optics (AO) is currently available at the major ground-based solar observatories, and has greatly improved the performance of telescopes.

Additionally, post-processing of high-cadence imaging data to correct the blurring effect of seeing has made a huge impact on image quality. Image restoration methods such as MOMFBD (Multi-Object Multi-Frame Blind Deconvolution, van Noort et al. 2005; Löfdahl 2002) and Speckle interferometry (see von der Lühe 1993, and references therein) have become essential for ground based high spatial-resolution solar imaging. As these methods allow to combine all the images obtained within a dataset while retaining high image quality, it removes the need for frame selection and results in more reliable and higher signal-to-noise data.

Send offprint requests to: R.S.S.: e-mail: rschnerr@science.uva.nl

In this context, Fabry-Pérot interferometer (FPI) based instruments have become quite popular and are in operation at many solar observatories, e.g. CRISP (Scharmer et al. 2008) at the Swedish 1-m Solar Telescope (SST), the Göttingen Fabry-Pérot spectropolarimeter (Puschmann et al. 2006) at the Vacuum Tower Telescope and the Interferometric bidirectional spectrometer (IBIS, Cavallini 2006) at the Dunn Solar Telescope. Similar instruments will likely be developed for the future 4-m class solar telescopes ATST and EST. The main advantages of FPIs compared to Lyot filters are that they have a high transmission, allow for rapid wavelength tuning and a dual-beam polarimetric setup with a polarizing beam splitter close to the final focal plane. A disadvantage is that even very well-made FPIs will show variations in the width and central wavelength of the transmission peak over the field of view (FOV, e.g. Reardon & Cavallini 2008). When the FPIs are set up in a telecentric mount, as is the case with CRISP, these variations cause intensity variations at relatively small spatial scales. In collimated mount, such small scale features disappear, but the central wavelength shifts systematically away from the center of the image. For further comments on FPIs in telecentric vs. collimated mount see Scharmer (2006).

A theoretical approach of the processing of full-Stokes line scans from FPI based instruments is discussed by van Noort et al. (2010); here we present the practical application of that approach to real CRISP data of a sunspot observed in the 6302.5 Å Fe I

line, including all the necessary data reduction steps, such as correction for telescope polarization, flatfielding, image restoration and demodulation.

In Sect. 2 we discuss the general setup of the data acquisition procedures and in Sect. 3 the challenges and possibilities for calibration procedures are discussed. The proposed calibration procedure is presented in Sect. 4, results of the procedure applied to CRISP data are presented in Sect. 5, and the conclusions in Sect. 6.

2. Polarimetric data acquisition

2.1. The optical setup

The data acquisition setup used with CRISP at the SST (see Fig. 1) is similar to that used by van Noort & Rouppe van der Voort (2008), with the notable difference that the SOUP Lyot tunable filter has been replaced with the CRISP Fabry-Pérot filter (Scharmer et al. 2008). The use of a Fabry-Pérot filter results in a significant (∼ 8×) increase in the peak transmission of the filter over that of the Lyot filter, and the use of a dual beam polarimetric setup results in a significant reduction of the seeing-induced crosstalk. In addition, the higher tuning speed of CRISP allows for observing programs scanning over ∼10 spectral points instead of the 2–4 points one would typically get with the Lyot filter. A downside, however, is that the placement of the filter cavities in a telecentric mount configuration leads to small-scale pass-band shifts and transmission profile width variations across the FOV, due to cavity and reflectivity errors. Note that in the case of CRISP, the high- and low-resolution FPIs have been placed ∼10 cm away from the focal plane in order to smooth such variations.

CRISP data are obtained while continuously cycling through a 4-state liquid-crystal (LC) scheme, which converts combinations of the incoming polarization states Q, U and V to linear polarization that can be analyzed with the the polarizing beam splitter close to the final focal plane. Data are simultaneously recorded using two narrow-band cameras (a transmitted and reflected camera) in a dual-beam setup and a wide-band camera placed before the liquid-crystal variable retarders. The frame rate of ∼36 Hz is set by the rotating chopper, which has a duty cycle setting the exposure time at 16 ms while CCD readout is performed during the dark part of the cycle. For the data shown in this paper, 4 full LC-cycles were completed before tuning to the next of a total of 12 wavelengths. The complete linescan of 4 LC-states × 4 repeats × 12 wavelengths = 202 frames covers ∼ 6 seconds.

2.2. Image restoration

For ground-based high-resolution imaging, image restoration is a vital tool. However, for multi-wavelength and polarimetric observations it is especially important, as it will reduce differential image shifts and blurring between images recorded at different wavelengths and polarization states. In the case of polarimetric data this implies that the image restoration has to be done *before* demodulating the data (to convert the LC-states to Stokes parameters I,Q,U,V), because the images of the different LC-states are each associated with a particular seeing disturbance that must be compensated for individually, to reduce artificial, seeing induced, signals. In our analysis we have focused on image restoration using MOMFBD (van Noort et al. 2005), but some of the issues discussed below are equally relevant for Speckle restorations.

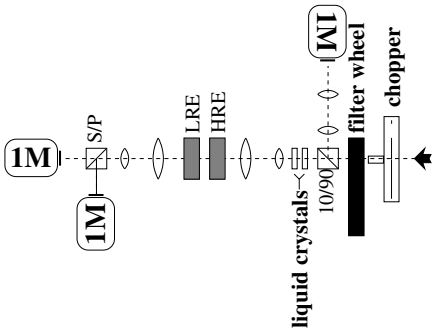

Fig. 1. Schematic drawing of the optical set-up at the SST. After reflecting off the dichroic mirror separating the red and blue beams (not shown), the red beam passes the chopper and prefilter. Then a beam splitter sends 10% of the light to the WB camera. The other beam passes the LCs, the high- and low-resolution etalons of the CRISP filter (LRE and HRE resp.), and finally a polarising beam splitter separating the p- and s-polarized light to the transmitted and reflected beams. All three cameras are 1024×1024 pixel (1M) Sarnoff cameras running at ∼36 Hz.

MOMFBD has several properties that can complicate calibrations:

1. The direct relation between an image pixel in the original data and the restored image is lost.
2. Artificial features in images can influence the wavefront sensing and can be amplified by the deconvolution.
3. Input images are assumed to be monochromatic; although MOMFBD can handle different wavelength channels within one restoration.
4. Noise is assumed to follow a Gaussian distribution with a constant width over each isoplanatic patch, which can be an issue when high-contrast targets are observed.

The loss of the direct relation between input data pixels and restored data pixels means that all calibrations that can not be done *before* image restoration, and hence before demodulating, can not be done on a pixel-by-pixel basis, but involve the point-spread-functions (PSFs, due to seeing and the finite pupil size) of the input images. Similarly, artificial features in the input images should be removed as much as possible before the image restoration, as they will interfere with the wavefront sensing and can be strongly amplified by the deconvolution. Input images that are not monochromatic over the FOV are rather hard to deal with, as this can not be properly corrected without knowing the entire line profile.

Both the wavelength changes over the FOV and the assumption of the Gaussian distribution with a constant width are limiting factors for the maximum (polarimetric) accuracy that can be obtained when using image restoration. To avoid interference from artifacts in the narrow band cameras on the wavefront sensing, one could only use images from the wide band camera for the wavefront sensing, and apply the corrections to the data of all cameras. However, the additional wavefront information contained in the narrow band data is then not used for the image restoration.

Image restoration of the data used in this paper was performed with MOMFBD assuming an isoplanatic angle of 96×96 pixels (∼5.7×5.7″) and using 37 Karhunen-Loève modes for modeling the wavefront phases.

3. Instrument calibration issues

A straightforward calibration scheme typically involves the following steps:

1. Dark correct data from the different cameras (transmitted, reflected and wide band).
2. Gain correct the different LC-state and wavelength images of all cameras.
3. Use image restoration to combine the data for the different cameras and states, and correct for the seeing.
4. Demodulate transmitted and reflected beams using the polarization calibration matrix (see Appendix A).
5. Combine Stokes images from the transmitted and reflected beams to reduce seeing crosstalk.
6. Compensate for telescope polarization using the inverse of the telescope Mueller matrix.

Due to specific instrumental properties, such as polarization dependent flatfields and FPI inhomogeneities, polarimetric and spectral calibration issues arise in step 2 to 4. These are discussed in more detail below.

3.1. Polarimetric issues

For polarimetric calibration of the data it is convenient to split the calibration in two parts:

1. **Telescope**. From the 1-m primary lens at the entrance of the vacuum tube down to the exit window at the bottom of the vacuum tube. Due to the 45° angle of incidence on the rotating azimuth- and elevation-mirrors, this part is intrinsically time variable, but is assumed to be independent of the line-of-sight (constant over the FOV). A model describing the Mueller matrix of the telescope as a function of the azimuth and elevation angles at 6302 Å was determined by Selbing (2006).
2. **Instrument**. From the vacuum exit window to the CCDs. This part is FOV dependent (e.g. dust close to the focal plane), but can be calibrated daily using calibration optics and is assumed not to be time dependent. It is described by a modulation matrix, that converts the input Stokes vector into intensities measured with the LC-states. How this matrix can be determined is described in Appendix A.

We can describe the total conversion matrix of the system ($\mathcal{A}$) as a matrix product of the Mueller matrix of the telescope $\mathcal{T}$ and the modulation matrix of the instrument $\mathcal{M}$ (see also van Noort et al. 2010):

$$\mathcal{A}(x, y, t) = \mathcal{M}(x, y) \cdot \mathcal{T}(t), \tag{1}$$

where the transmitted and the reflected beams have their own (although related) modulation matrices. As the intensity of the light during the determination of the telescope matrix and the modulation matrix is not known, an additional gain calibration is still required. The telescope matrix $\mathcal{T}(t)$ is time dependent, so the total system response matrix $\mathcal{A}$ is time dependent. This means that unless the flatfield images and the data are recorded at the same time, which is not practical, an appropriate gain correction must be computed. To this end, the flatfield must first be transformed to a time independent location. The obvious (and only) place available for this is the entrance of the telescope. The details of this procedure are discussed in Sect. 4.

3.2. Spectral issues

An important calibration issue is that part of the intensity changes over the field of view are not the result of real CCD gain variations, but due to variations in FPI reflectivity and cavity size (see, e.g., Reardon & Cavallini 2008; Cauzzi et al. 2009). When observing at a wavelength where $\delta I/\delta\lambda \neq 0$, e.g. in the wing of a spectral line, a wavelength shift due to a cavity error results in a change in the observed intensity which is completely unrelated to the gain of that particular pixel. Similarly, variations of the reflectivity cause changes of the integrated transmission profile.

The question, however, is which flatfield correction should be applied to the data. Although the intensity variations due to cavity errors are not real gain changes, the same cavity errors also affect the science data. The line profiles in the science data can be very different though, and therefore the intensity changes will in general not be the same as in the flatfield data. A change in wavelength scale due to a cavity error just *cannot* be corrected in a flatfielding procedure, which only changes the intensity, unless one knows the exact lineprofile. For a data calibration scheme without image restoration, one could attempt to somehow determine the real pixel gains, apply those, and account for the wavelength shifts later on in the analysis. For image restoration, however, the intensity variations that then remain could pose a problem for the wavefront sensing and/or the deconvolution.

The strategy that we propose is discussed in the next section.

4. Calibration scheme

For the wavefront sensing part of the image restoration it is important to use images that are as monochromatic as possible and without sharp artifacts. Sharp features can result from CCD pixel rows that have different response to the polarization of the incoming Stokes vector. These pixels stand out in some of the matrix elements of $\mathcal{M}$. If the polarization of the incoming light is low, the telescope polarization is known, and the instrument is stable, these features should be reproduced in flatfields that are properly converted to the time of the observations, as this information is contained in the modulation matrix. Dealing with the non-monochromatic nature of the data, due to FPI transmission variations over the FOV, is more complicated. In the final restored data one can attempt to take into account the wavelength shift due to cavity errors, although as a result of the image restoration process the effective shift in a given pixel in the restored image is always some mix of the shifts of all CCD pixels within the PSFs of the dataset. For the image restoration the intensity changes are more problematic, especially if they contain high spatial frequencies, as they distort the wavefront sensing. Note that intensity changes due to reflectivity and cavity errors of the FPI cannot simply be interpreted as brighter or darker regions in the observed object by the wavefront sensing, as they do not move with the object as the seeing varies throughout a dataset.

Our approach is to use flatfields that make the data as smooth as possible, before using the data for the wavefront sensing. This is done using the recipe described in Sect. 4.1. These flatfields *include* intensity changes due to varying cavity properties over the FOV. This is a straightforward choice, but a relatively arbitrary one, as such a flatfield will only properly correct these intensity changes if the observed lineprofile is the same as that of the flatfield data, which is in general not the case. For the final restored data however, we do not want to use these flatfields, as that would modify the observed lineprofiles, but the actual CCD response.

A relatively simple way to obtain the CCD gains without being affected by cavity errors in the FPI would be to use a wavelength close to the observed line where $\delta I/\delta\lambda = 0$. However, such a method does not account for the wavelength dependence of the impact of transmission profile changes due to reflectivity errors (e.g. in the line core an increase of the transmission profile width would increase the observed intensity by a larger factor than in the continuum). Additionally, it cannot remove (all of) the wavelength dependent fringes that are observed in the Sarnoff cameras, and the wavelength where such flats have to be taken might not correspond to the preferred continuum point, as the instrumental response has to be taken into account, increasing the time required for calibrations. Therefore we have developed a more accurate routine to derive the flatfield that corresponds to the real CCD response and simultaneously solves for the FPI cavity and reflectivity errors, and prefilter changes over the FOV. This routine is described in Sect. 4.2.

4.1. Time independent and image restoration flatfields

To obtain time independent flatfields, we have to invert the modulation matrix of each pixel to obtain the demodulation matrix ($\mathcal{M}^{-1}$, which is the inverse of the modulation matrix $\mathcal{M}$). By applying the demodulation matrix to the flatfield data of the 4 LC-states, we obtain flatfield images for all Stokes parameters under the vacuum tube exit window. Using the inverse Mueller matrix of the telescope, valid for the time at which the flatfields were taken, we can calculate the Stokes flats before the entrance lens of the telescope. As the signal-to-noise ratio in the Q, U and V flatfields is rather poor, because the signal is quite low, we assume that they are identical to the I flatfield and use that instead.

To calculate the flatfields relevant for the time the observations were obtained, one has to apply the telescope matrix applicable for that time, and then apply the modulation matrix. These flats will include intensity changes due to cavity and reflectivity errors, but the polarization levels should be properly reproduced to the accuracy that the telescope Mueller matrix and modulation matrix are known.

4.2. Getting the real CCD gains

The FPI has small variations of the cavity size and reflectivity, which results in changes in the central wavelength and width of the transmission profile, respectively. In addition, the central wavelength of the prefilter has a slight dependence on the tilt angle, as the angle of incidence changes over the FOV. To determine the real CCD gain, one has to account for these effects. At the SST, flatfields are determined by summing many (~1000) exposures per state and wavelength obtained while the telescope pointing is moving across the solar disc (to avoid intensity changes over the FOV due to limb darkening). If one assumes that the spectral profile of the averaged flatfield is constant over the FOV, then the different factors can be determined by using an iterative fitting scheme.

The transmission of a single FPI is given by the Airy function (e.g. Kentischer et al. 1998):

$$T_{\mathrm{FPI}} = \frac{1}{1 + F\sin^2(2\pi dn\cos\theta/\lambda)} \tag{2}$$

where the finesse F is given by

$$F = \frac{4R}{(1-R)^2} \tag{3}$$

with R the reflectivity, d the cavity size, n the refractive index in the cavity, θ the angle of incidence and λ the wavelength. The total transmission Ψ of the dual FPI setup of CRISP is calculated by multiplying the transmission of the high-resolution (T_{hr}) and low-resolution FPI (T_{lr}), assuming $\theta = 0$ and that cavity and reflectivity errors in the low-resolution FPI can be neglected as those in the high-resolution FPI will be dominant:

$$\Psi(R, \Delta R) = T_{\mathrm{lr}}(R) \cdot T_{\mathrm{hr}}(R + \Delta R) \tag{4}$$

As the spectral range used is small relative to the prefilter transmission profile width, we can limit the number of free parameters by not including the average prefilter shape in our fits, but instead only fit the deviations from the mean prefilter shape, assuming a linear dependence on wavelength.

Given the constant line profile $\phi(\lambda)$, average transmission profile $\Psi(R)$ of the combined FPIs and (wavelength independent) gain g, the observed lineprofile in pixel i will be given by:

$$\phi_{obs,i}(\lambda) = g_i \cdot [(1 + D_{pf,i}) \cdot (\lambda - \lambda_0)] \cdot \Psi(R + \Delta R_i) * \phi(\lambda - \Delta\lambda_i) \tag{5}$$

where g_i is the pixel gain, $D_{pf,i}$ the prefilter deviation factor, ΔR_i the reflectivity error, $\Delta\lambda_i$ the cavity error and λ_0 the central wavelength of the line.

The iterative scheme is initiated by setting g_i to the inverse of the mean intensity of the line profile, $\lambda_0 - \Delta\lambda_i$ to the minimum of a parabolic fit to the line minimum, and $D_{pf,i}$ and ΔR_i to zero. Applying these corrections one can then overplot all the observed line profiles and determine the average line profile by calculating a spline through a set of points at fixed wavelengths, of which the intensity is determined by a χ^2 minimalization routine (see Fig. 2; all fitting was done using the mpfit package, see Markwardt 2009; Moré 1978). The "real" line profile is then calculated by deconvolving this fitted lineprofile with the average transmission profile. As we now have an estimate for the average lineprofile and transmission profile, we can fit for the four unknown parameters in Eq. 5 for each pixel. These parameters allow us to improve our estimate for the average lineprofile and transmission profile. These two steps can be repeated until no more improvement is made.

Results of this fitting routine applied to a real dataset (see Sect. 5) are shown in Figs. 2 and 3. The total gain of a pixel is determined by the wavelength independent part g_i and a wavelength dependent part given by the ratio of the observed intensity and the fitted line profile, as shown in Fig. 2.

4.3. The prefilter transmission profile

After the prefilter deviation factor and average line profile have been determined, we use the average lineprofile of all the pixels (corrected for cavity errors and gain) to determine the average prefilter shape T_{PF}. The prefilter, which is mounted at a slight angle to tune the central wavelength, is assumed to have a Lorentzian profile:

$$T_{\mathrm{PF}}(\lambda) = \frac{1}{1 + (2\,(\lambda - \lambda_{0,\mathrm{PF}})/w)^{2N_{\mathrm{cav}}}} \tag{6}$$

where $\lambda_{0,\mathrm{PF}}$ is the prefilter central wavelength, w the full-width at half-maximum (FWHM) and N_{cav}(=2) the number of cavities of the prefilter.

The prefilter parameters $\lambda_{0,\mathrm{PF}}$ and w are determined by matching the average observed lineprofile to the lineprofile of the FTS atlas (the atlas acquired with the Fourier Transform Spectrometer at the McMath-Pierce Telescope, available from

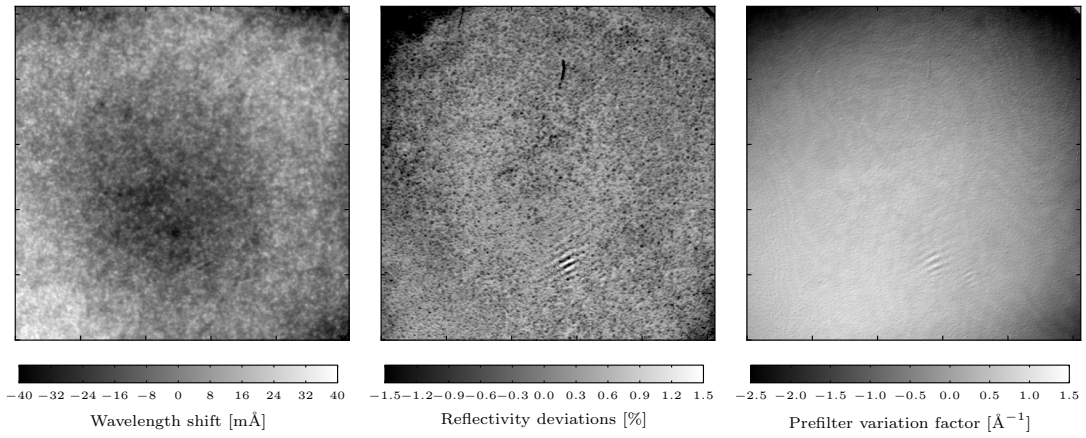

Fig. 3. Wavelength shift resulting from cavity errors (*left*), variations in the FPI reflectivity (*middle*, nominal value 93.5%) and the prefilter variation factor (*right*) as determined by the fitting routine described in Sect. 4.2 (see also Eq. 5) when applied to the 6302 Å dataset presented in Sect. 5.

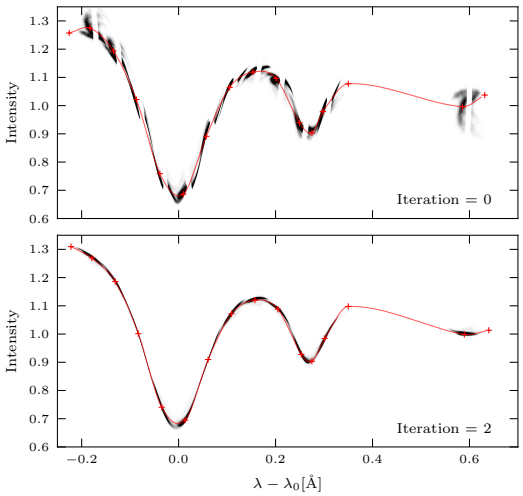

Fig. 2. Density plot of intensity (arbitrary units) vs. wavelength relative to line core for all points in the summed flatfield data before the first iteration (*top*, where the line center has been determined using a parabolic fit to the line core) and the same plot after the second iteration (*bottom*). The average line profile $\phi(\lambda)$, described by a spline curve through the a number of nodes (red plusses), is overplotted in red.

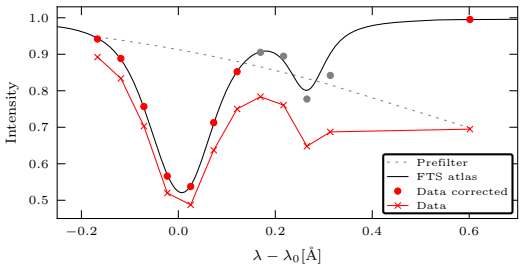

Fig. 4. The prefilter shape (dashed line) is determined by matching the uncorrected average spectrum (crosses) to the FTS convolved with the CRISP transmission (full black line). After correcting for the prefilter an excellent match if found (red circles). The points in the telluric line (grey circles) were not used in the procedure.

Brault & Neckel 1987) convolved with the average transmission of CRISP (see Fig. 4), masking the points in the telluric line. We find a prefilter width of 4.7±0.4 Å, which agrees with the specification of 4.4-4.6 Å, and a central wavelength of 6301.2±0.2 Å.

4.4. Iterative versus direct method

Having calculated both the actual CCD gains that we want to apply in the end and flatfields that should be used for the image restoration, we still have to account for the impact of the image restoration process, as the result of which the 1-to-1 pixel relation is lost. Here we discuss two possible approaches to that problem:

- **Direct method**. Apply the flatfields prepared for the image restoration to the data and after the image restoration remove these flatfields and apply the real gains, taking the average of the PSFs determined by the image restoration process into account.
- **Iterative method**. Use the PSFs that have been determined by the image restoration to iteratively determine the Stokes images that given the telescope Mueller matrix, modulation matrix, PSFs, and gains, best reproduces the observed data.

For the direct method, flatfields for the time of the observations are determined as described in Sect. 4.1, which are used for the image restoration process. These flatfields are then removed from the restored data and the true flatfield applied by multiplying with the convolution of the average PSF with the ratio of the image restoration flatfield and the true flatfield. The demodulation is then performed with the inverse of the modulation matrix convolved with the average PSF. The idea behind this is that each pixel in the restored image ”samples“ the whole PSF, and therefore the convolved calibration data should be applied.

An alternative, more simple but computationally expensive, method is the iterative method that was developed by van Noort et al. (2010). This approach solves the entire forward problem, including all the calibrations, and varies the incoming Stokes images to find the solution that best fits the observed data, taking all the individial PSFs into account.

5. Results

5.1. Example: sunspot 6302

As a test for our reduction method we have reduced a dataset from the 27th of October 2009, which has part of the δ sunspot AR11029 in the field of view (see Fig. 5) at a heliocentric angle of about 45°. The data contain 11 equidistant wavelength points around the core of the Fe I 6302.5 Å line with a wavelength separation of 48 mÅ and a continuum point at +600 mÅ.

5.2. Stokes parameters

In Fig. 5 we show the improvement in the Stokes parameters that is reached by using the scheme described in Sect. 4 as compared to straightforwardly applying standard calibrations as listed in Sect. 3. Polarimetric errors due to the changing telescope polarization that influences the flatfields are visible as saddle-shaped offsets in Stokes Q, U and V, a vertical fringe-like pattern strongest in Stokes Q and U, and as sharp lines in Stokes Q, U and V (indicated with white arrows in Fig. 5), that almost completely disappear with the new calibration method.

The origin of this problem lies in the variations of the modulation matrix. In Fig. 6 we show 2 representative examples of the 16 components of the modulation matrix; the contributions of Stokes I and Q to LC-state 1. As is the case for all the LC-states, the Stokes I contribution shows a vertical fringe-like pattern over the whole FOV, some smaller scale patterns, likely related to dust, and sharp lines. The Stokes Q contribution is much more smooth and mainly shows a saddle shape and some sharp lines, which is typical for the contributions of Stokes Q, U and V to the LC-states. If the incoming polarization of the light changes (e.g. due to the varying telescope polarization), the relative contributions of the Stokes parameters change and therefore the flatfield will change.

Note that the dark regions in the Stokes V map in Fig. 5 are actual signal that has been redshifted into the continuum wavelength due to strong downflows (see also Sect. 5.3). The small spot of fringes near the bottom of the Stokes Q, U and V images is likely due to a polarizing speck, e.g. dust, in the telescope, that is not accounted for in the telescope model.

5.3. Inversion results

The data are inverted using the inversion code Nicole (Socas-Navarro et al. 2010). For the inversions we use three nodes in temperature, two nodes in line-of-sight velocity ($v_{\rm los}$) and one node (i.e. the parameters has a constant value) for the magnetic field parameters and the microturbulence. The average transmission profile (see Sect. 4.2) is used to account for the finite spectral resolution of CRISP.

Results of the inversions are shown in Fig. 7. The shift in the velocities due to cavity errors of the FPI is corrected by subtracting a map of the cavity errors as determined in Sect. 4.2 convolved with the average PSF of the whole dataset. The velocity is determined by taking the average value in the range $[-1.0 < \tau_{cont} < -3.0]$, and the zero velocity reference was set to the average velocity in the umbra. Adopting this velocity reference we find a convective blueshift as measured from the granulation in the FOV of 0.3 km s^{-1}, which is consistent with the theoretical value of 0.4 km s^{-1} (de la Cruz Rodríguez et al. 2010).

Both the velocity and longitudinal magnetic field can reliably be determined from the data, showing fast (~5 km s^{-1}) outflows at the center-side penumbra and downflows (up to ~10 km s^{-1}) on the intersection between the umbra and penumbra slightly below the middle of the FOV.

6. Conclusions

We have presented a method to reduce full Stokes data obtained with CRISP at the SST: an instrument with a fast-tuning Fabry-Pérot filter in a telecentric mount. Although some calibration issues are inherent to such an instrument when used together with image restoration, most problems can be overcome by using proper calibration procedures.

The impact of wavelength shifts over the FOV, due to cavity errors, on the flatfields can be corrected for. This is important to prevent changes of the line shape due to errors in the gain tables. For instruments with the FPI in a collimated mount the cavity errors occur in pupil space, and are therefore not an issue in this respect. Such instruments do show radial wavelength shifts over the FOV that have to be accounted for (Janssen & Cauzzi 2006).

Without a proper calibration scheme the polarimetric imprint of the flatfielding can cause strong saddle shaped offsets, fringes, and sharp lines due to deviating pixel rows/columns that are enhanced by the deconvolution in the image restoration. Using the proposed calibration scheme these artifacts can be almost completely removed. Any remaining weak artifacts are most likely due to discrepancies in the SST telescope model, which is only accurate to a few tenths of a percent, and non-zero intrinsic polarization. The severity of the artifacts depends on the (variation of the) telescope polarization and the variations of the modulation matrix elements over the FOV. For telescopes that have low and/or constant intrinsic polarization and instrumentation of which the modulation matrix elements are nearly constant over the FOV, such flatfielding issues will be much less severe.

Velocities as determined from inversions of the data can be corrected for cavity errors using a convolved version of the cavity map. However, the PSFs will vary from wavelength to wavelength resulting in a non-equidistant wavelength sampling. Both the wavelength sampling and the variations of the width of the FPI transmission peak will vary from pixel-to-pixel, but can in principle be taken into account during the inversions. An intrinsic limitation is the use of non-monochromatic input images for the image restoration, which results in deconvolution artifacts: mixing of information from different wavelengths through the image restoration.

Modern developments in FPI instrumentation, such as rapid (kHz) modulation combined with charge shuffling (which may allow for demodulation before image restoration), could simplify calibration issues. However, to reach the polarimetric and spectroscopic accuracy that the future large solar observatories EST and ATST are aiming for with the next generation of Fabry-Pérot systems, advanced calibration techniques to deal with issues discussed here will be required.

Acknowledgements. We would like to thank P. Sütterlin for taking the observations. This research project has been supported by a Marie Curie Early Stage Research Training Fellowship of the European Community's Sixth Framework Programme under contract number MEST-CT-2005-020395: The USO-SP International School for Solar Physics. The Swedish 1-m Solar Telescope is operated on the island of La Palma by the Institute for Solar Physics of the Royal

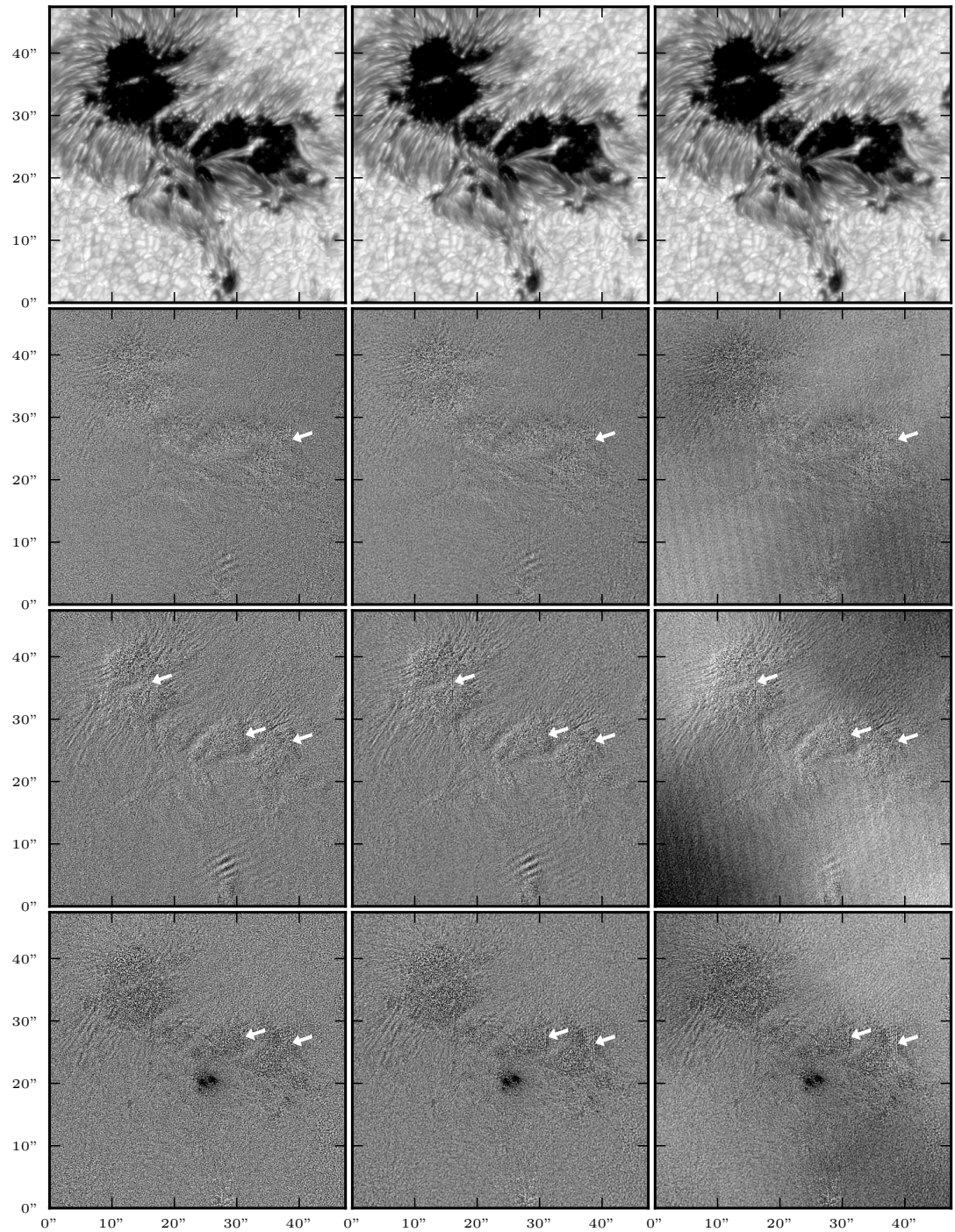

Fig. 5. Continuum Stokes I, Q, U and V images (from *top* to *bottom*) of the sunspot observed with the SST in the 6302.5 Å Fe I line on 27th of October 2009. The images on the *left* have been calibrated with the described calibration scheme and the iterative method, the images in the *middle* use the direct method instead, and the images on the *right* have been calibrated by straightforwardly applying standard calibrations as listed in Sect. 3 and using the direct method. The full range of the polarized images is −1.5% to +1.5%. The arrows indicate where, for some methods, sharp artifacts occur. Continuum offsets in the Q, U and V images, most likely resulting from discrepancies in the telescope model, of up to ∼0.35% have been subtracted. Note that the small dark region visible in the Stokes V image is actual signal in a region with strong downflows (see text).

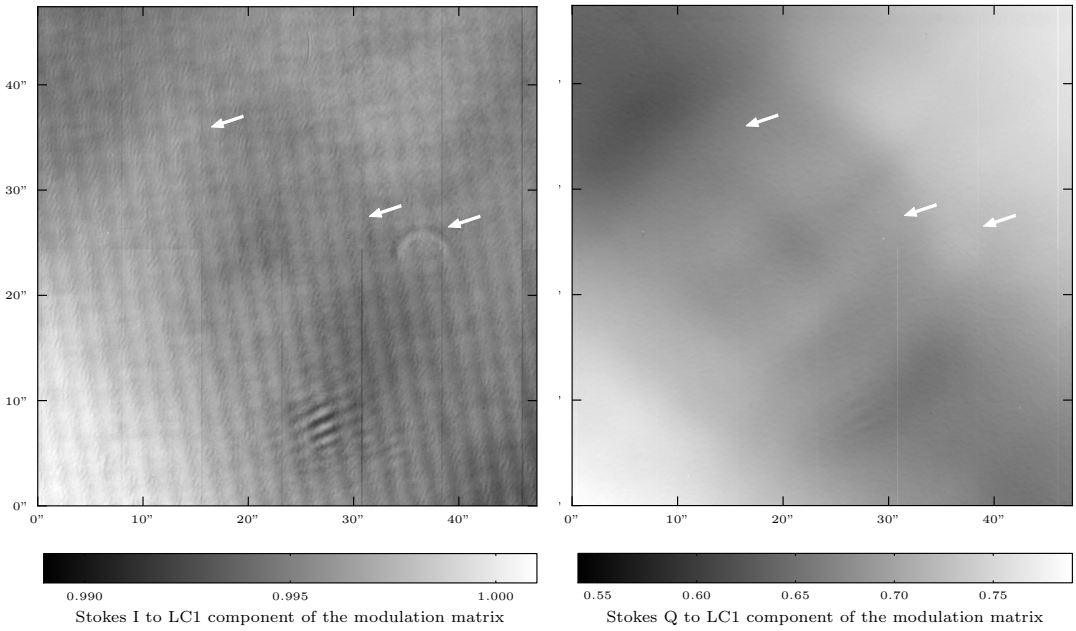

Fig. 6. Variations of modulation matrix elements over the FOV. The element describing the contribution of Stokes I to LC-state 1 is shown on the *left* and the contribution of Stokes Q to LC-state 1 is shown on the *right*.

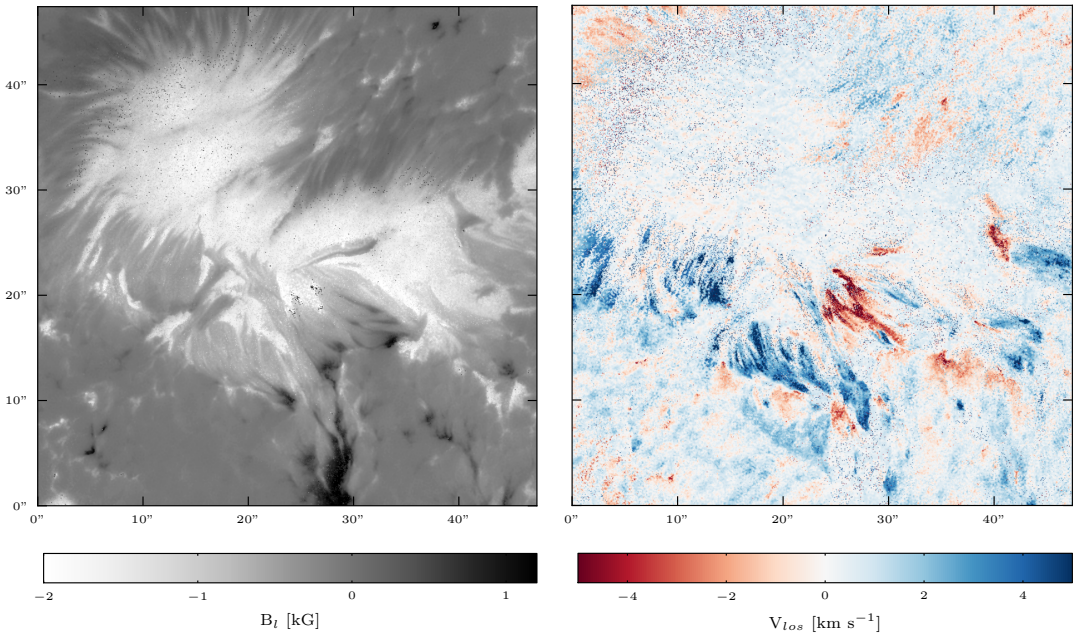

Fig. 7. Results of inversions of the data, showing the line-of-sight component of the magnetic field (*left*) and the line-of-sight component of the velocity (*right*). The inversions have some difficulties converging to the proper solution in locations of strong ($\sim$10 km s^{-1}) downflows where the lineprofile is not completely sampled due to the Doppler shift. The limb is towards the upper right.

Swedish Academy of Sciences in the Spanish Observatorio del Roque de los Muchachos of the Instituto de Astrofísica de Canarias.

References

Brault, J. W. & Neckel, H. 1987, ftp://ftp.hs.uni-hamburg.de/pub/outgoing/FTS-Atlas
Cauzzi, G., Reardon, K., Rutten, R. J., Tritschler, A., & Uitenbroek, H. 2009, A&A, 503, 577
Cavallini, F. 2006, Sol. Phys., 236, 415
de la Cruz Rodríguez, J., Kiselman, D., & Carlsson, M. 2010, A&A, submitted
Janssen, K. & Cauzzi, G. 2006, A&A, 450, 365
Kentischer, T. J., Schmidt, W., Sigwarth, M., & Uexkuell, M. V. 1998, A&A, 340, 569
Löfdahl, M. G. 2002, in Proc. SPIE, Vol. 4792, Image Reconstruction from Incomplete Data II, ed. Bones, Fiddy, & Millane, 146
Markwardt, C. B. 2009, in Astronomical Society of the Pacific Conference Series, Vol. 411, Astronomical Society of the Pacific Conference Series, ed. D. A. Bohlender, D. Durand, & P. Dowler, 251
Moré, J. 1978, in Lecture Notes in Mathematics, Vol. 360, Numerical Analysis, ed. G. A. Watson, 105
Puschmann, K. G., Kneer, F., Seelemann, T., & Wittmann, A. D. 2006, A&A, 451, 1151
Reardon, K. P. & Cavallini, F. 2008, A&A, 481, 897
Scharmer, G. B. 2006, A&A, 447, 1111
Scharmer, G. B., Narayan, G., Hillberg, T., et al. 2008, ApJ, 689, L69
Selbing, J. 2006, Master's thesis, Stockholm University
Socas-Navarro, H., de la Cruz Rodríguez, J., Asensio-Ramos, A., Trujillo-Bueno, J., & Ruiz-Cobo, B. 2010, in preparation
van Noort, M., Rouppe van der Voort, L., & Löfdahl, M. G. 2005, Sol. Phys., 228, 191
van Noort, M., Schnerr, R. S., & de la Cruz Rodríguez, J. 2010, in preparation
van Noort, M. J. & Rouppe van der Voort, L. H. M. 2008, A&A, 489, 429
von der Lühe, O. 1993, A&A, 268, 374

Appendix A: Determining the Modulation Matrix

When fitting the pixel dependent system response matrix $\mathcal{M}$, it is important to realize that the incoming intensity I is not known. A fit can therefore only be made on the fractional polarization, which means that we need to normalize the data with the intensity. The resulting data, lacking absolute transmission information, can only be used to determine the modulation matrix up to a constant factor λ^{-1}. Moreover, the normalization of the data requires us to compute the intensity from the data using the inverse of the unknown modulation matrix $\mathcal{M}$. It is therefore more natural to formulate the fit directly in terms of the demodulation matrix $\mathcal{M}^{-1}$:

$$\mathcal{M}^{-1} = \begin{pmatrix} b_{11} & b_{12} & b_{13} & b_{14} \\ b_{21} & b_{22} & b_{23} & b_{24} \\ b_{31} & b_{32} & b_{33} & b_{34} \\ b_{41} & b_{42} & b_{43} & b_{44} \end{pmatrix}.$$

The calibration data is taken using a linear polarizer followed by a $\lambda/4$-wave plate, which produces a known (relative) polarization, independent of polarization of the incoming light, by seperately rotating the two plates. Given the the calibration data $\boldsymbol{v}$ and the known (normalised) Stokes vector of the incoming light $\boldsymbol{S}$, we have for each calibration measurement point n with unknown intensity I_n:

$$b_{ij} v_{j,n} = S_{i,n} I_l = S_{i,n} \sum_{k=1}^{4} b_{1k} v_{k,n} \tag{A.1}$$

so that for a given guess-solution for $\mathcal{M}^{-1}$, the total accumulated fit error between the data and the guess-matrix can be written as

$$\chi^2 = \sum_{i=1}^{4} \sum_{n} \left(\sum_{j=1}^{4} b_{ij} v_{j,n} - S_{i,n} \sum_{j=1}^{4} b_{1j} v_{j,n} \right)^2. \tag{A.2}$$

Due to the use of normalized data, we have

$$\sum_{j=1}^{4} b_{1j} = \lambda. \tag{A.3}$$

Substitution in Eq. A.2 eliminates the contribution to χ^2 for $i = 1$, as $S_{i,n} = 1$. The minimum value of χ^2 is then given by $\frac{\partial \chi^2}{\partial b_{kl}} = 0$, giving

$$\begin{aligned} \frac{\partial}{\partial b_{kl}} \sum_{i=2}^{4} \sum_{n} \left(\sum_{j=1}^{4} b_{ij} v_{j,n} - S_{i,n} \left[\lambda v_{1,n} + \sum_{j=2}^{4} b_{1j} (v_{j,n} - v_{1,n}) \right] \right)^2 &= 0 \\ \sum_{i=2}^{4} \sum_{n} \frac{\partial}{\partial b_{kl}} \left(\sum_{j=1}^{4} b_{ij} v_{j,n} - S_{i,n} \left[\lambda v_{1,n} + \sum_{j=2}^{4} b_{1j} (v_{j,n} - v_{1,n}) \right] \right)^2 &= 0. \end{aligned}$$

Applying the chain rule results in

$$2 \sum_{i=2}^{4} \sum_{n} \left(\sum_{j=1}^{4} b_{ij} v_{j,n} - S_{i,n} \left[\lambda v_{1,n} + \sum_{j=2}^{4} b_{1j} (v_{j,n} - v_{1,n}) \right] \right) \left(\sum_{j=1}^{4} \delta_{ik} \delta_{jl} v_{j,n} - S_{i,n} \sum_{j=2}^{4} \delta_{1k} \delta_{jl} (v_{j,n} - v_{1,n}) \right) = 0,$$

where the last 2 sums over j can be evaluated

$$\sum_{i=2}^{4} \sum_{n} \left(\sum_{j=1}^{4} b_{ij} v_{j,n} - S_{i,n} \left[\lambda v_{1,n} + \sum_{j=2}^{4} b_{1j} (v_{j,n} - v_{1,n}) \right] \right) (\delta_{ik} v_{l,n} - S_{i,n} \delta_{1k} (v_{l,n} - v_{1,n})) = 0. \tag{A.4}$$

This expression splits naturally in 2 separate cases.

For $k = 1,\ l = 2, 3, 4$:

$$\begin{aligned} \sum_{i=2}^{4} \sum_{n} \left(\sum_{j=1}^{4} b_{ij} v_{j,n} - S_{i,n} \left[\lambda v_{1,n} + \sum_{j=2}^{4} b_{1j} (v_{j,n} - v_{1,n}) \right] \right) (-S_{i,n} (v_{l,n} - v_{1,n})) &= 0 \\ \sum_{i=2}^{4} \sum_{n} \left(\sum_{j=1}^{4} b_{ij} v_{j,n} - S_{i,n} \sum_{j=2}^{4} b_{1j} (v_{j,n} - v_{1,n}) \right) S_{i,n} (v_{j,n} - v_{1,n}) &= \lambda \sum_{i=2}^{4} \sum_{n} S_{i,n}^2 v_{1,n} (v_{l,n} - v_{1,n}) \end{aligned} \tag{A.5}$$

and for $k > 1,\ l = 1, 2, 3, 4$

$$\begin{aligned} \sum_{i=2}^{4} \sum_{n} \left(\sum_{j=1}^{4} b_{ij} v_{j,n} - S_{i,n} \left[\lambda v_{1,n} + \sum_{j=2}^{4} b_{1j} (v_{j,n} - v_{1,n}) \right] \right) \delta_{ik} v_{l,n} &= 0 \\ \sum_{n} \left(\sum_{j=1}^{4} b_{kj} v_{j,n} - S_{k,n} \sum_{j=2}^{4} b_{1j} (v_{j,n} - v_{1,n}) \right) v_{l,n} &= \lambda \sum_{n} v_{l,n} S_{k,n} v_{1,n} \end{aligned} \tag{A.6}$$

The solution of this system gives the least-squares fit to the data, which can be re-normalized by choosing an appropriate value for λ. The natural choice for λ is 2, as the maximum intensity measured by one of the beams of the polarimeter is $\frac{1}{2} I$ for unpolarized light. The one remaining element b_{11} is constrained by Eq. A.3.